

①

Dissertation

Femtosecond Laser Spectroscopy
of Excited-State Dynamics
in Vanadyl Phthalocyanines

Akira Terasaki

Submitted to
Department of Physics
Faculty of Science
University of Tokyo

October, 1991

ACKNOWLEDGEMENTS

I would like to express my sincerest gratitude to my advisor, Prof. T. Kobayashi, for his guidance and encouragement throughout the course of the present work and for affording me the opportunity to pursue this exciting research.

It should be noted that this work has been carried out as one of the projects in Nonlinear Optics and Advanced Materials' team of Frontier Research Program (Institute of Physical and Chemical Research, RIKEN). I would like to express my gratitude to Prof. A.F. Garito, the head of the team, and Drs. A. Yamada and H. Sasabe, the coordinators, for affording me the occasion to take part in this research project.

Special thanks are due to Dr. T. Wada, who offered me a lot of valuable advice, helped me in many ways, and encouraged me, Mr. M. Hosoda, who prepared most of the phthalocyanine samples studied in the present work and discussed a great deal with me, and Dr. M. Hara, with whom I had stimulating discussion.

One of the samples, vanadyl phthalocyanine deposited on alkali halide substrates by the molecular-beam-epitaxy technique, was provided by Prof. A. Koma and Mr. H. Tada. I would like to acknowledge their kindness.

I am grateful to Dr. J.P. Sokoloff for the stimulating discussion and the critical reading of a part of the present manuscript, and to Dr. T. Hattori and Mr. E. Tokunaga for their help in experiments and fruitful discussion. Thanks are also due to Messrs. A. Kaneko and T. Yamamoto, who helped me in some of the measurements for sample characterization. I am also thankful to Dr. M. Yoshizawa and Mr. M. Taiji for their many pieces of helpful advice on experimental techniques, and to Dr. C.H. Grossman for his collaboration in the early stage of the laser construction. And also I acknowledge the instructive discussion about phthalocyanines with Drs. K. Ishikawa

and S. Koshihara. I thank all the members of our group in RIKEN and University of Tokyo for their daily discussion and helpful advice on the research.

Many other people supported the present work. I am especially thankful to technical engineers in RIKEN for making many optics holders and mounts, jet nozzles, and electronic circuits, and for supplying liquid helium, and also to the building managers for their efforts to improve the cooling water system for the lasers.

This work was supported in part by Grant-in-Aid for Encouragement of Young Scientists (02952075) from the Ministry of Education, Science, and Culture of Japan. Also, I would like to express my gratitude to the Japan Society for the Promotion of Science for Japanese Junior Scientists and Teijin Scholarship for their financial supports.

Finally, I wish to thank my family for their understanding and warm encouragement throughout the course of my study.

TABLE OF CONTENTS

ACKNOWLEDGEMENTS	iii
TABLE OF CONTENTS	v
CHAPTER 1. INTRODUCTION	1
CHAPTER 2. FEMTOSECOND LASER SYSTEM	4
2.1. Introduction to ultrashort light pulses	4
2.2. Mode locking	8
2.3. Colliding-pulse mode-locked ring dye laser	10
2.4. High-repetition-rate amplifier	24
2.5. White-light continuum pulses	37
2.6. Measurement techniques	46
2.6.1. Degenerate four-wave mixing	46
2.6.2. Pump-probe measurement	52
2.7. Further improvements	55
CHAPTER 3. THEORY OF MEASUREMENTS	58
3.1. Third-order nonlinear polarization	58
3.2. Degenerate four-wave mixing	61
3.3. Pump-probe spectroscopy	67
CHAPTER 4. EXCITED-STATE DYNAMICS	
IN VANADYL PHTHALOCYANINES	72
4.1. Introduction	72
4.2. Sample preparation	75
4.3. Excited electronic states	82
4.4. Experimental procedure	90

4.5. Results and discussion	92
4.5.1. Isolated molecular phase	92
4.5.2. Phase II	96
4.5.3. Phase I	105
4.5.4. Films deposited on KBr	115
4.5.5. Coherent transient phenomena and induced phase modulation	125
4.6. Conclusions	137
CHAPTER 5. CONCLUDING REMARKS	141
REFERENCES	144

CHAPTER 1

INTRODUCTION

Recently there has been growing interest in the dynamical properties of materials. These studies reveal how fundamental physical phenomena bring an excited system to equilibrium. Among these are studies of the transient response of various materials after short optical pulse excitation. Time-resolved spectroscopy can be related to frequency domain studies, such as light scattering, using the temporal and spectral Fourier-transform relation of electric fields. However, except for the simple systems, these two methods are not equivalent, but provide complementary information. If one is interested in the time evolution of a system, time-resolved studies give more direct and detailed information; the shorter the pulses, the more detailed the information. Within the last decade, short pulse technology has made rapid progress and now pulses as short as 6 fs, which contain only three optical cycles, are generated [1].

In the nanosecond regime, or longer, time-resolved measurements can be carried out using electronic instruments, while, in the pico- or femtosecond region, ordinary electronics, except for such as streak cameras, lack the required resolution and a special high resolution technique, *i.e.*, a correlation technique, is utilized to obtain a time resolution limited only by pulse duration. In this technique, two light pulses are used typically. The change in a system induced by the first pulse is probed by the second delayed pulse and time is measured by the delay between the two pulses. Therefore, the observations are based on nonlinear optical phenomena. And also, because short pulses have extremely high peak powers, advances in short-pulse technology have contributed to the development of nonlinear optics.

By using short light pulses, various types of spectroscopic techniques have been invented and applied to numbers of studies of dynamical events in physics, chemistry, and biology [2]. A part of the studies is material research aimed at the development of functional optical devices utilizing nonlinear optical phenomena for the control of light. Required properties of materials for such applications are large optical nonlinearity, fast response, thermal and chemical stability, and processibility. While inorganic semiconductors have been investigated extensively, organic materials possessing conjugated π -electron systems have also been studied widely and known to have large optical nonlinearities and ultrafast responses [3] in addition to their great advantage in processibility. Among them, phthalocyanines have good thermal and chemical stability as well and proper chemical modification makes them soluble in some of the organic solvents, which is an important advantage in processing. The compounds show differences in their optical and electronic properties depending on the morphology, *i.e.*, the structure of stacking of the molecules, as well as the central metal. Their nonlinear optical properties were also found to have such dependence and now studies of their excited-state dynamics attract interest.

My thesis work has been carried out to clarify the dynamical properties of their excited states using a newly constructed femtosecond laser system. The present study was specifically focused on the morphology dependence, systematic studies of which have not been performed yet, by fixing the central metal for oxovanadium. It is expected to elucidate the relation between the dynamics and the origin of the excited electronic states as well as the mechanism of their relaxation. The relaxation kinetics were found to have strong morphology dependence, which is considered to be due to the differences in interactions between molecules. It is an interesting fact that molecular systems consisting of the same molecule can show markedly different transient optical response because of the molecular arrangement. Although only

vanadyl phthalocyanine was studied here, the result should give some general prospects for similar systems.

This dissertation is organized as follows. In Chapter 2, the femtosecond laser system, I have constructed, is described. In Chapter 3, a simple general theory of typical time-resolved measurements is given. The studies of excited-state dynamics in vanadyl phthalocyanines in several morphological forms are discussed in Chapter 4. Chapter 5 contains conclusions based on the present studies and the future prospects of this research.

CHAPTER 2

FEMTOSECOND LASER SYSTEM

Techniques for femtosecond pulse generation have made rapid progress in the past ten years [4] and nowadays a variety of femtosecond lasers are commercially available. However, their operation and maintenance are still not simple or easy. Furthermore, since different systems have different characteristics, it is very important to know the features of our own system in order to operate it optimally.

This chapter describes construction and characterization of a laser system for femtosecond spectroscopy, which consists of a colliding-pulse mode-locked ring dye laser, a high-repetition-rate amplifier pumped by a copper vapor laser, and systems for time-resolved measurements including pump-probe and degenerate four-wave mixing techniques. Characterization of femtosecond continuum pulses is also described. Before these descriptions, a brief history and an introduction to the essential techniques of ultrashort pulse generation are given. In the last section, possible improvements of the present system are proposed.

2.1. Introduction to ultrashort light pulses

The research of the ultrashort optical pulses is one of the streams of laser technology aimed at the achievement of the extremes. Since the first picosecond-pulse generation by passive mode locking of a Q-switched ruby laser was reported in 1965 [5], the technique to produce ultrashort laser pulses has made rapid progress. The first subpicosecond pulses were generated in 1968 by compressing chirped picosecond output pulses of a mode-locked Nd:glass laser down to 0.4 ps by a pair of gratings [6]. A stimulated Raman oscillator was applied to generate 0.3-ps pulses at the Stokes line of benzene, in 1971, by pumping it with picosecond pulses of the

second harmonic of a mode-locked Nd:glass laser [7]. In 1972, 0.7-ps pulses were generated by compressing picosecond mode-locked pulses of a Nd:glass laser by multiple transits through a saturable absorber-amplifier system [8]. And it was in 1974 that the first subpicosecond pulses as short as 0.5 ps were generated directly from a laser cavity by the passive mode-locking technique [9]. After this report, ultrashort pulse generation using dye lasers developed because of the advantage of broad gain spectra of dyes.

The epochal event occurred in 1981, when optical pulses shorter than 100 fs were generated by the colliding-pulse mode-locking (CPM) technique [10]. This marked the beginning of the femtosecond era. During these researches it was found that the group-velocity dispersion (GVD) inside the laser cavity plays an important role in short pulse generation [11-13], because the 100-fs pulses, which have bandwidths as broad as 10 nm, easily broaden temporally by passing through dispersive media such as optical elements. These optical elements usually have positive GVD in the visible region, *i.e.*, red component propagates faster than blue component. For example, after passing through a 1-mm thick silicate glass plate, Fourier-transform (FT) limited 10-fs pulses with center wavelength of 620 nm double in duration, while FT limited 1-ps pulses change their duration only by 10⁻⁶%. Several known or new optical configurations were exploited to produce variable negative GVD [14-18] by the use of gratings, prisms, or interferometers. Introduction of such configurations of optical elements into the dye laser cavity has made the output pulse duration much shorter. The CPM ring dye laser containing a four-prism sequence for GVD compensation has been shown to be able to generate pulses as short as 27 fs by balancing the intracavity GVD, self-phase modulation (SPM), saturable absorption, and saturable gain [19,20]. This type of dispersion-

compensated CPM ring dye laser is one of the most reliable femtosecond lasers in the sense of pulse duration and stability.

With the prism-pair configuration, GVD, *i.e.*, the second-order phase distortion, can be compensated for, but the third-order phase distortion remains and plays a pulse broadening role in the cavity [21]. More recently a new attempt has been made to compensate also for the third-order distortion with contribution of a prism sequence and a chirp-compensation cavity mirrors which have a well controlled stacking of dielectric layer coating [22-24]. With this technique pulses as short as 22 fs have been produced [25], which are the shortest ever pulses generated directly from a laser cavity.

The intracavity-dispersion-control element, *i.e.*, one- or two-pair prism sequence, has been used in other types of lasers. Pulses as short as 29 fs have also been generated from a linear dye laser cavity, which is hybridly mode-locked by synchronous pumping from a cw mode-locked Nd:YAG laser and a saturable absorber [26]. Attempts to take advantage of both synchronous pumping and CPM have also been made with an anti-resonant ring laser cavity [27] and pulses shorter than 100 fs are routinely obtained [28-32]. One of the advantages of synchronous pumping compared with passive mode locking is that the output can be actively stabilized with a feedback system by monitoring the intensity or spectrum of the output and adjusting the cavity length [30,31,33,34]. Further, it not only produces pulses with relatively high output power but also simplifies synchronization with other systems, such as amplifiers.

Because the pulses generated from dye lasers have pulse energies of the order of 0.1 nJ, various techniques for optical pulse amplification have also been developed [35]. High-power but low-repetition-rate amplifiers are based on a Q-switched Nd:YAG laser for excitation [36] and recently millijoule pulses focusable to

intensities of the order of 10^{16} W/cm² have been reported [37]. Amplifiers producing relatively low output power but high repetition rates have been achieved with pumping sources of copper vapor lasers [38-41], excimer lasers [42-44], Nd:YAG or Nd:YLF regenerative amplifiers [45], a cavity-dumped, Q-switched, mode-locked, cw pumped Nd:YAG laser [46], and a cavity-dumped, Q-switched, cw pumped Nd:YAG laser [47]. These light sources produce repetition rates ranging from 100 Hz to 10 kHz. By using the amplified pulses, femtosecond continuum can also be generated [48], which extends the usable wavelength region from less than 400 nm to more than 1 μ m, and also provides an ideal broad spectral probe for femtosecond spectroscopy.

Techniques of pulse compression have also made progress along with the development of short-pulse dye lasers and amplifiers [49-53]. And now, pulses as short as 6 fs can be generated by compensating for both the second- and the third-order phase distortion of self-phase modulated pulses from an optical fiber by appropriate combination of grating pairs and prism pairs [1].

In the early stage of the development of the ultrashort-pulse lasers, the available wavelength was limited to a red region around 600 nm. The lasers had poor tunability because only the combination of rhodamine 590 and DODCI as gain and saturable absorber dyes gave stable pulses shorter than 100 fs. Therefore, extensive efforts have been made to develop lasers in other wavelength regions. Several techniques have been exploited. One method is to operate dye lasers with other dye combinations [54-58]. Second is wavelength conversion by harmonic generation [59-62] and successive amplification [63-66], difference frequency mixing [67,68] or seeded optical parametric amplification based on it [69], optical parametric oscillation [70,71], stimulated electronic Raman scattering [72], and so on. Third is to amplify a selected spectral component of continuum pulses by a second amplifier [44,73,74] or by optical parametric amplification [75]. Fourth is to excite another dye with intense

femtosecond pulses by a configuration of traveling-wave amplifier [76-78]. And recently, new gain media other than dyes have been developed. Among such materials, titanium doped sapphire ($\text{Ti:Al}_2\text{O}_3$) [79] has an extremely broad gain region in the near infrared and has already proved itself as a useful material for short pulse generation. Much work has been devoted to femtosecond pulse generation with this crystal and a novel mechanism of mode locking has been discovered [80,81]. By these various techniques, femtosecond pulses are now obtainable over a wide spectral range from the ultraviolet to the infrared.

Using femtosecond pulses, experiments with femtosecond time resolution can be carried out. However, because ordinary electronic instruments cannot resolve the short optical pulses, correlation techniques are utilized. The method often adopted is to divide one short pulse into two, pass each pulse through different optical delay lines to the same spot on a sample material. By varying the path length of one of the optical delay lines, the time delay between the two pulses can be controlled. Because light propagates $3 \mu\text{m}$ in 10 fs in air, high time resolution can be achieved easily by the mechanical technique of micron-resolution spatial positioning.

2.2. Mode locking

As described in the preceding section, mode locking technique is essential in short pulse generation [82]. It locks the phase relation among the longitudinal modes of the laser cavity and produces coherence in the frequency domain by modulating the loss, gain, or phase inside the cavity synchronously with the round trip time. Mode locking is either done actively or passively. Active mode-locking utilizes an active modulator such as acousto-optic (A/O) and electro-optic (E/O) devices, which modulate the cavity loss or phase at the frequency corresponding exactly to a half of the round trip time of light in the cavity. In the case of dye lasers, an actively mode-

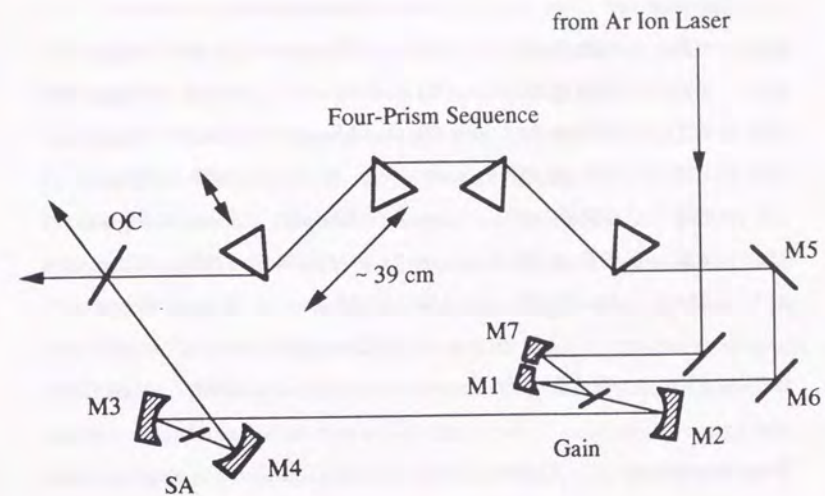
locked laser can be used as an excitation light source. This technique is called "synchronous pumping," which is also a type of active mode locking. On the other hand, the passively mode-locked lasers include a saturable absorber in the cavity [83-86]. This acts as a passive loss modulator. The low intensity parts of the light are absorbed, while the high intensity parts are transmitted because the material's absorption gets saturated. Both techniques can be used together, which is called "hybrid mode locking," as in the case of a synchronously pumped dye laser containing a saturable absorber. More recently a new type of technique, "additive-pulse mode locking" or "coupled-cavity mode locking," was invented [87,88]. Mode-locking technique is still making progress now. A current topic in this area is the Kerr-lens mode-locking mechanism in Ti:sapphire lasers, which corresponds to passive phase modulation [80,81].

Colliding-pulse mode locking (CPM)[10], which helped initiate the ultrashort pulse technology, is one of the passive mode-locking techniques. The two counterpropagating pulses collide at a saturable absorber which is thinner than the spatial pulse length. The two pulses interfere in the saturable absorber and form a transient grating which enhances the pulse shortening effect because of the higher amplitude of the electric field at grating peaks than that of a single pulse having the same pulse energy as the sum of the two pulses, and/or the backward diffraction of a part of the pulse from the transient grating [83,89]. Because of this pulse shortening enhancement, pulses shorter than 100 fs are easily obtained. Moreover, the colliding pulses form a mechanism to stabilize the laser oscillation. Such effects in the CPM were confirmed in the anti-resonant ring dye laser [28]. That is why the CPM technique is often utilized for femtosecond-pulse generation and also why it was chosen for our system.

The pulse shortening mechanism in this type of passively mode-locked dye lasers is the balance of the absorption saturation, the gain saturation, self-phase modulation (SPM), and group velocity dispersion (GVD) [20]. Among these factors the latter two effects are significantly important for the generation of pulses shorter than 100 fs. SPM happens in a saturable absorber jet or in a gain jet, where the laser beam is tightly focused, and is controlled by changing the spot size in the jets or the pump power of the excitation laser source. GVD is caused in each optical element, which the laser beam passes through or is reflected by. By introducing prism pairs to the cavity the total amount of dispersion can be controlled by adjusting the position of one of the prisms to change the pass length of the beam inside the glass. Proper balancing of SPM and GVD can yield soliton-like pulse shaping and result in ultrashort pulses.

2.3. Colliding-pulse mode-locked ring dye laser

In the present system, a colliding-pulse mode-locked (CPM) ring dye laser is utilized as a source of femtosecond pulse trains, which was pumped by a cw Ar-ion laser (Model 171-09 or Model 2030, Spectra Physics) operated at 514.5 nm [20]. The schematic of our dye laser is shown in Fig. 2-1. The specifications of the optical elements are listed in Table 2-1. The dye-laser cavity consists of seven mirrors, a four-prism sequence for balancing the dispersion in the cavity, a gain-dye jet (rhodamine 6G / ethylene glycol, $ca. 2 \times 10^{-3}$ mol/l), and a saturable-absorber-dye jet (DODCI / ethylene glycol, $ca. 1.5 \times 10^{-3}$ mol/l). At this condition the threshold power of the pump laser for dye laser operation was between 2 and 3 W. A focusing concave mirror for the pump laser (M7) is separated from the cavity mirror (M1) so that extra dispersion is not introduced in the cavity. The cavity length is $ca. 3$ m, which corresponds to a repetition rate of 100 MHz, and the gain jet and the saturable-



- M1-7 : Dielectric coated high-reflectance mirrors
- OC : Output coupler
- SA : Saturable Absorber

Figure 2-1 Cavity configuration of colliding-pulse mode-locked (CPM) ring dye laser

	λ /nm	Reflectivity	r /mm	Diameter	Thickness	Comment
M1	620	HR @ 0°	100	15 mm	10 mm	Virgo
				(D-shape)		
M2	620	HR @ 0°	100	15 mm	10 mm	Virgo
M3	620	HR @ 0°	50	15 mm	11 mm	Virgo
M4	620	HR @ 0°	50	15 mm	11 mm	Virgo
M5	620	HR @ 45°	∞	1"	1/4"	Virgo
or	620	HR @ 45°	∞	30 mm	5 mm	Sigma
M6	620	HR @ 45°	∞	1"	1/4"	Virgo
M7	514.5	HR @ 0°	100	15 mm	10 mm	Virgo
				(D-shape)		
OC	630	98.5% @ 0°	∞	1"	1/4"	Virgo

Brewster prisms Quartz

Gain jet

~300 μ m thick Rhodamine 6G / EG ~ 2×10^{-3} mol/l

Saturable absorber jet

~50 μ m thick DODCI / EG ~ 1.5×10^{-3} mol/l

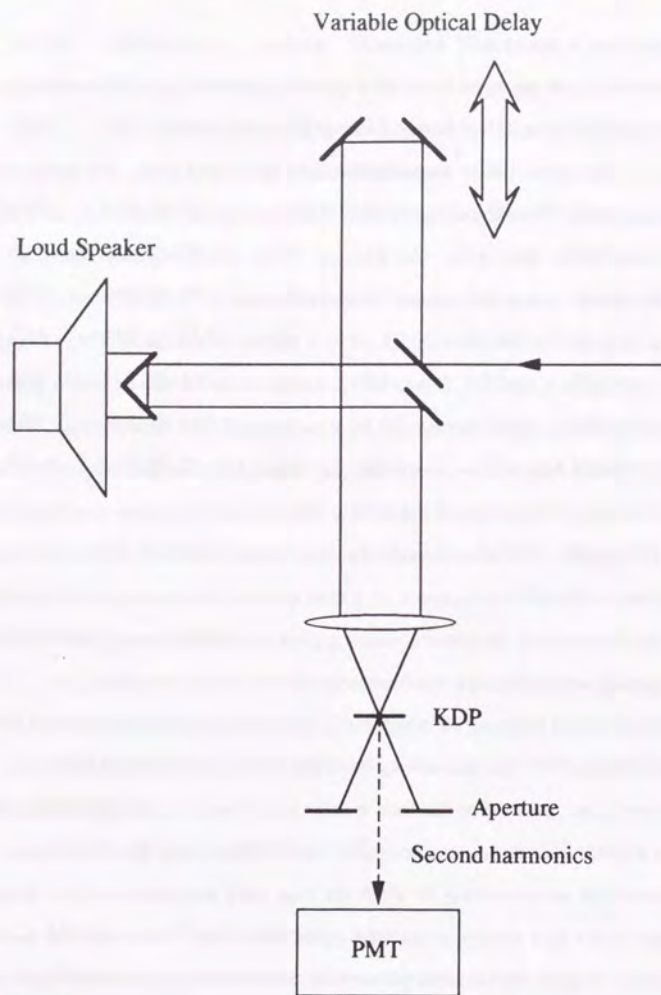
λ : Center wavelength of mirror coating

r : Radius of curvature of concave mirrors

Table 2-1 Specifications of optical elements used in the colliding-pulse mode-locked (CPM) ring dye laser

absorber jet are separated by about a quarter of the cavity length in order to obtain almost the same gain for both counter-propagating pulses.

The output pulses were characterized by several ways. The pulse train was detected by a PIN photodiode (S2840, Hamamatsu) and observed by an oscilloscope (Model 2465B, Tektronix). The spectrum of the output was observed by a spectrometer with a multichannel photodiode array (USP-500, Unisoku), which can display a spectrum at about 20 Hz, or by a photomultiplier tube (PMT) through a monochromator (MC-10, Ritsu) with a stepper-motor-driven rotatable grating. Its autocorrelation trace was obtained by a background-free autocorrelator, which is illustrated in Fig. 2-2, by measuring the second-harmonic intensity generated by the contribution of two delayed pulses in a 100- μ m thick potassium dihydrogen phosphate (KDP) crystal. The autocorrelator has two scanning modes. A fast-scan mode utilizes a retroreflector mounted on a loud speaker, which modulates the optical delay at the frequency of the electric pulses applied to the loud speaker (*ca.* 50 Hz). By triggering an oscilloscope synchronously with the delay modulation, the autocorrelation trace can be monitored in real time, which is convenient in the fine adjustment of the dye laser cavity. However, since the displacement of the retroreflector mounted on the loud speaker is not linear to the applied voltage, it does not display an accurate autocorrelation trace. Therefore, a slow-scan mode was used for accurate measurements, in which the time delay was controlled by a translation stage driven by a stepper motor with 3.3-fs resolution. Since, once the dye laser was properly aligned, reproducible pulses were obtained daily, optimization of the cavity alignment was usually done by monitoring the output pulses diffracted onto a screen and adjusting the position of one of the prisms to maximize the spectral width. The fluctuation of the output intensity was at most 3%.

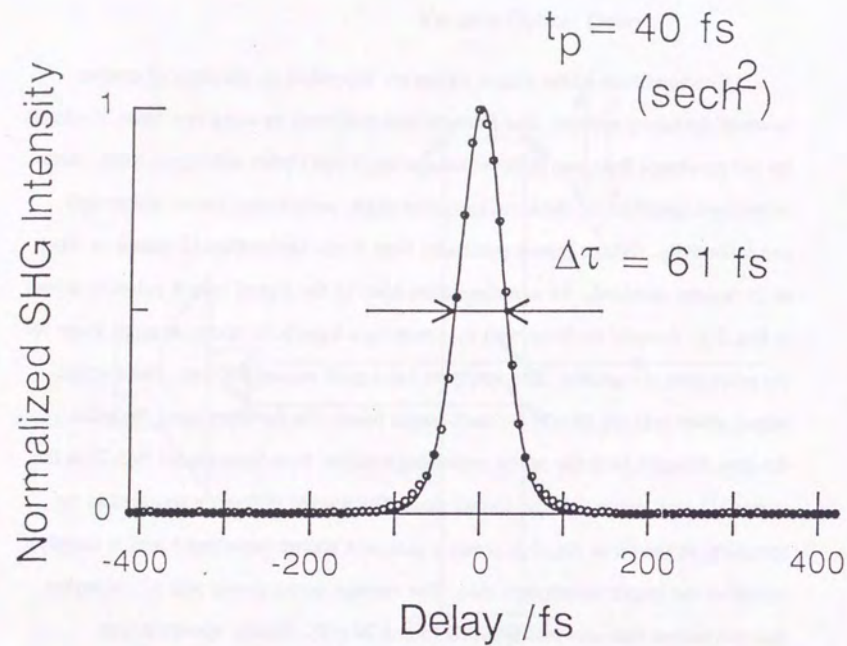


PMT: Photomultiplier Tube

Figure 2-2 Autocorrelator

Characteristics of the output pulses are dependent on the stack of coating layers of the cavity mirrors. The property was confirmed by using two types of mirrors for M5 purchased from two different companies, Virgo Optics and Sigma-Koki. Both mirrors are specified for the same incidence angle, polarization, center wavelength, and reflectivity. With a mirror purchased from Virgo Optics (M5-1), pulses as short as 34 fs were obtained. An autocorrelation trace of the typical output pulses is shown in Fig. 2-3. It could be fitted well by assuming a hyperbolic-secant-squared shape for the pulse-intensity profile. The spectrum has a peak around 630 nm. The average output power was *ca.* 10 mW for each output beam. On the other hand, the pulse duration obtained from the cavity containing a mirror from Sigma-Koki (M5-2) as the mirror M5 was longer than the former case. The marked difference appeared in the spectrum, as shown in Fig. 2-4; it has a peak at a shorter wavelength and is sharply cut-off at the longer wavelength side. The average output power was a little higher than the former case and was between 15 and 20 mW. Similar spectrum was observed when the dye laser cavity was constructed with six mirrors by replacing the pair of 45° mirror, M5 and M6, with a high reflectance mirror at normal incidence purchased from Virgo Optics. In this case the spectrum of the output was also sharply cut-off at longer wavelength side and the duration of stable pulses was longer than 50 fs.

Although the cavity containing the mirror M5-1 produced the shortest pulse, double pulsing took place frequently in this configuration. This is explained as follows by using a scheme shown in Fig. 2-5. Because the gain jet and the saturable absorber jet are separated by about a quarter of the perimeter of the cavity, two counterpropagating pulses starting from the saturable absorber jet at time zero arrive at the gain jet at time $t_{r,t}/4$ and $3t_{r,t}/4$, respectively, where $t_{r,t}$ is the round trip time of light along the cavity. When the pumping rate is high enough to recover the gain



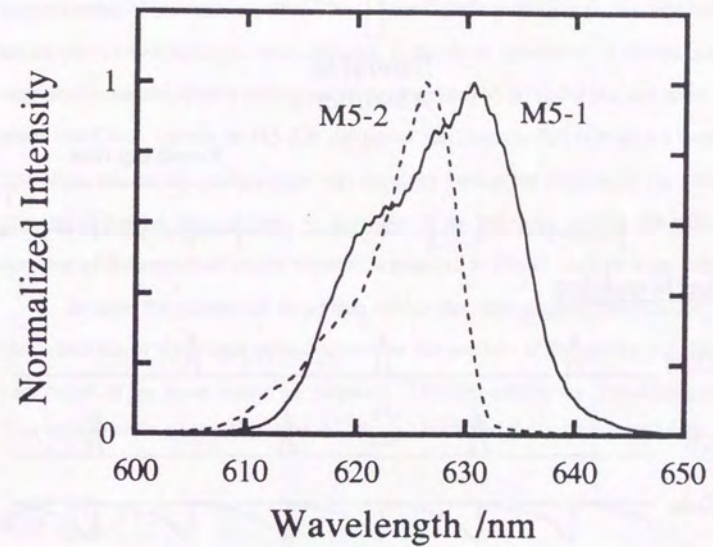
○ : Data

— : Fitting curve for hyperbolic-secant squared pulses shape

$\Delta\tau$: FWHM of autocorrelation trace

t_p : FWHM of intensity profile for hyperbolic-secant squared pulses

Figure 2-3 Background-free SHG autocorrelation of CPM ring dye laser pulses



Solid line : from the cavity containing a mirror M5-1

Dashed line : from the cavity containing a mirror M5-2

Figure 2-4 Spectra of the shortest pulses of the CPM dye laser output

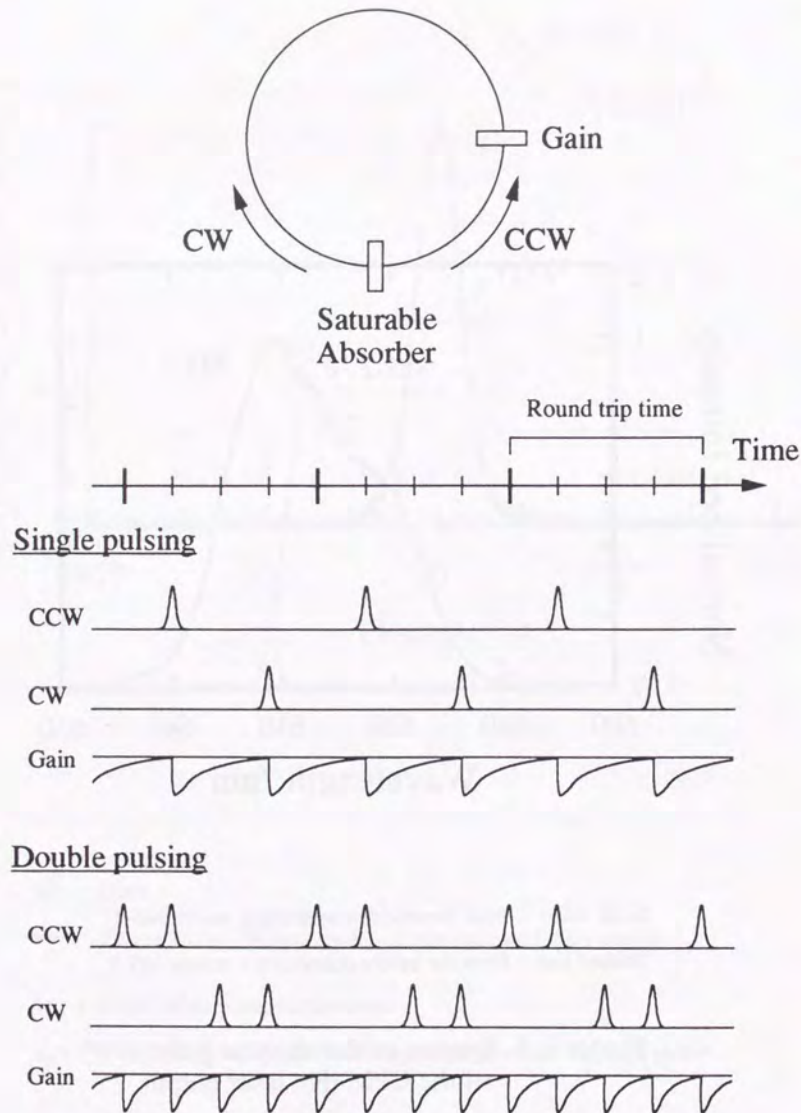


Figure 2-5 Schematics of single and double pulsing of CPM ring laser

within $t_{r,t}/4$, another pair of counter propagating pulses is generated and undergoes gain at time $t_{r,t}/2$ and $t_{r,t}$, which are the middle of the gain minima for single pair of pulse generation. Thus, two similar pulses separated by $t_{r,t}/4$ come out from the laser into each output direction. In the same manner, a higher pumping rate produces larger number of pulses in a period. Since this multiple pulsing is an obstacle in the actual use for spectroscopic measurements, it should be prevented. It turned out empirically that the double pulsing could be prevented by pumping the dye laser constructed with the mirror M5-2 at the power less than *ca.* 200 mW above threshold. Therefore, this cavity configuration was normally used at the expense of the pulse duration of the dye-laser output. As described in the following section, the pulse duration of the amplified pulses is rather insensitive to that of the dye-laser output.

Because the amount of dispersion affects the pulse shaping process, the characteristics of the output pulses depend on the position of the prisms, *i.e.*, the total path length of the beam inside the prisms, l . This dependence was also examined. The second-order phase distortion ϕ'' ($= \frac{\partial^2 \phi}{\partial \omega^2}$) is related to the path length l by

$$\phi'' = \frac{\lambda^3}{2\pi c^2} n'' \cdot l, \quad (2-1)$$

where c is the velocity of light, λ is the wavelength of the pulse, and n'' is the second-order derivative of refractive index with respect to wavelength at λ . The coefficient of r.h.s. of the above equation is about 51, 69, and 299 (fs)²/mm for SiO₂, BK7, and SF11, respectively, at 620 nm. The dependence of spectra on the intracavity dispersion is shown in Fig. 2-6. As the total pass length inside the prisms l increased, the spectrum became broader and its peak shifted to longer wavelength. But after certain length l_0 , the spectrum showed a sharp peak. When l was shorter than l_0 , *i.e.*, more

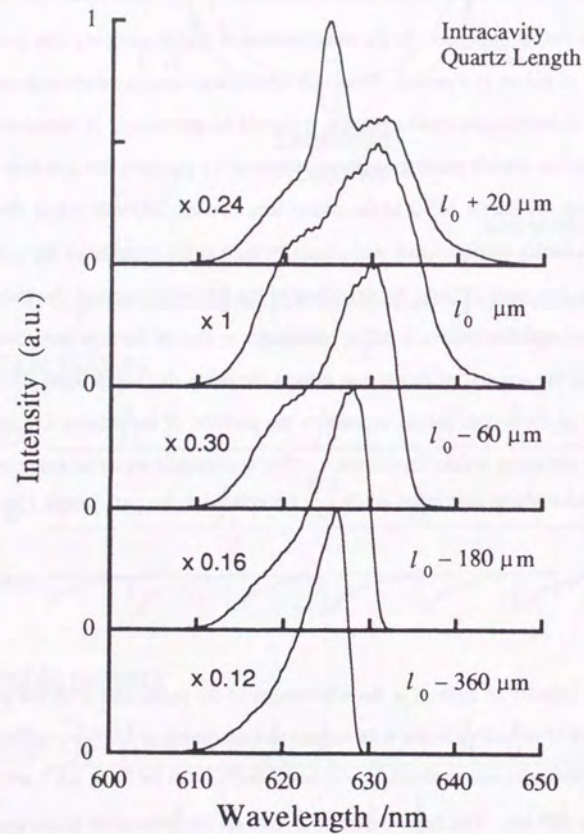


Figure 2-6 Dependence of dye laser spectra on intracavity dispersion

negative dispersion, the dye laser showed stable mode locking, whereas at longer cases, *i.e.*, less negative dispersion, it would not be mode-locked. The pulse duration was the shortest at the critical point l_0 and increased as l decreased.

The autocorrelation trace at $l - l_0 = 0 \mu\text{m}$ ($\phi'' - \phi''_0 = 0(\text{fs})^2$) fitted well to that of hyperbolic-secant squared pulse as shown in Fig. 2-3. But at shorter l the trace could not be fitted by that pulse shape. For example, an autocorrelation trace at $l - l_0 = -230 \mu\text{m}$ ($\phi'' - \phi''_0 = -12(\text{fs})^2$) is shown in Fig. 2-7. In order to explain this trace, the following asymmetric pulse shape,

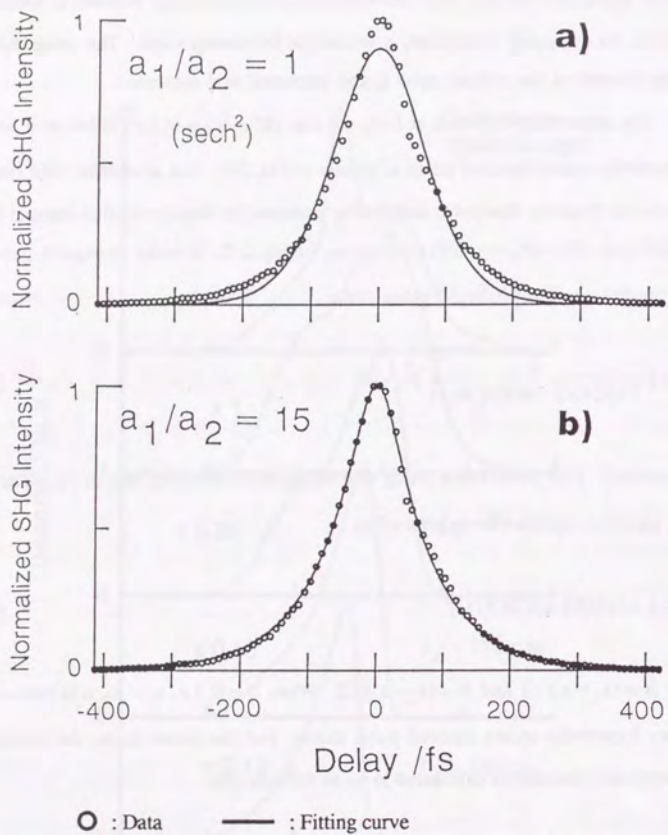
$$I(t) = \left[\frac{2}{\exp[a_1 t] + \exp[-a_2 t]} \right]^2, \quad (2-2)$$

was assumed. This pulse has a rising rate of $2a_2$ and a decaying rate of $2a_1$. The above equation can also be expressed as

$$I(t) = \left[\exp[Bt] \cdot \text{sech}(At) \right]^2, \quad (2-3)$$

where $A = (a_2 + a_1) / 2$ and $B = (a_2 - a_1) / 2$. When $B = 0$, *i.e.*, $a_1 = a_2$, it is reduced to ordinary hyperbolic-secant squared pulse shape. For this pulse shape, the intensity autocorrelation function is calculated to be as follows [90]:

$$\begin{aligned} I_{\text{SH}}(\tau) &= \frac{\int_{-\infty}^{\infty} dt I(t) \cdot I(t - \tau)}{\int_{-\infty}^{\infty} dt |I(t)|^2} \\ &= 3 \frac{A^2}{A^2 - 4B^2} \cdot \text{cosech}^2(A\tau) \\ &\quad \times \left[A \frac{\sinh(2B\tau)}{2B} \cdot \coth(A\tau) - \cosh(2B\tau) \right] \end{aligned} \quad (2-4a)$$



- a) Hyperbolic-secant squared pulse shape ; $a_1/a_2 = 1$ in Eq. (2-2).
 b) Asymmetric pulse shape ; $a_1/a_2 = 15$ in Eq. (2-2).

Figure 2-7 Fitting of autocorrelation trace of the dye laser output at intracavity quartz length $l_0 = 230 \mu\text{m}$

$$= 3 \operatorname{cosech}^2(A\tau) [A\tau \cdot \operatorname{coth}(A\tau) - 1] ; B = 0 \quad (2-4b)$$

$$= \frac{3 \sinh(2A\tau) - 6A\tau}{4 \sinh^3(A\tau)} ; B = \pm \frac{A}{2} . \quad (2-4c)$$

This function yielded a good fit to the trace at the absolute value of the ratio $a_1/a_2 = 15$ as shown in Fig. 2-7b. This behavior can be explained qualitatively in connection with the asymmetric spectrum as follows. Because of the gain saturation, the trailing edge of the pulse decays more rapidly than the rise of the leading edge. Since the generated pulse is down-chirped because of the introduction of negative dispersion in the cavity, the red component at the trailing edge of the pulse is suppressed and hence the sharp cut-off of the spectrum at the long wavelength side. However, this asymmetry in the temporal profile seems to be quite large. On the other hand, a symmetric function which has much sharper peak than that of a hyperbolic-secant-squared shape should have an autocorrelation function similar to Fig. 2-7b. As such a function, the following function is known from the theory of passive mode locking [84]:

$$I(t) = \frac{1 - \alpha}{\cosh^2 u - \alpha} ; a \cdot t = u - \alpha \cdot \tanh u \quad (0 \leq \alpha < 1) . \quad (2-5)$$

The asymptotic shape of this function is as follows:

$$I(t) \sim \frac{1}{1 + \frac{1}{(1 - \alpha)^3} (at)^2} ; t \sim 0 \quad (2-6a)$$

and

$$I(t) \sim 4(1 - \alpha) \exp[-2\alpha] \exp[-2\alpha|t|] ; t \sim \infty . \quad (2-6b)$$

When $\alpha = 0$, this function is reduced to a hyperbolic-secant squared pulse shape. As the parameter α increases, the pulse shape becomes sharper. The data in Fig. 2-7 could also be fitted well by the autocorrelation function of this pulse shape with $\alpha \sim 0.6$. From the above consideration, when negative dispersion is introduced, the pulse is expected to be chirped and have an asymmetric temporal shape because of the marked asymmetry in its spectrum. But slight sharpening of the pulse shape should also exist as observed in the autocorrelation trace largely deviated from that of a hyperbolic-secant squared shape. Recently, a sophisticated method was developed to characterize pulse shape and chirp by measuring its interferometric SHG autocorrelation and interferogram [91]. This technique would be helpful in the analyses of such pulses.

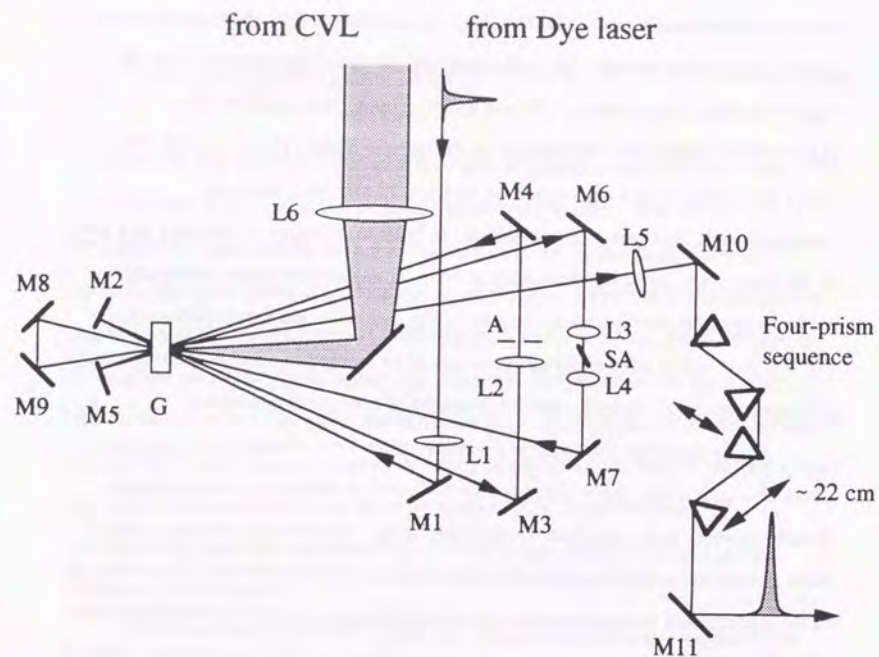
The characteristics of the output also depended on the displacement of the saturable absorber jet from the focal point of the concave-mirror pair, *i.e.*, the degree of SPM [20]. At the focal point, the peak wavelength was the shortest and the spectrum was the narrowest. As the displacement increased up to a few hundred micrometers, the spectrum became red shifted and broader and the pulse duration was reduced. But, when the displacement was too large, the laser would not be mode-locked.

2.4. High-repetition-rate amplifier

Because the output-pulse energy of the dye laser was between 0.1 and 0.2 nJ, it was necessary to amplify these pulses to obtain intensity high enough for spectroscopy, particularly, for the generation of white light continuum. Several pump

sources are commonly used [35-47], which are characterized by their repetition rates and amplified pulse energy. Generally speaking, the lower the repetition rate, the higher the output pulse energy. Among them, a copper vapor laser (CVL) (MLT/30/SP, Metalaser) was adopted in the present system [38-41,92-94]. This pump laser operates at a high repetition rate, *ca.* 10 kHz, and produces compromisingly high gain of amplification. In order to minimize the focusing spot size of the laser beam, its cavity was made to be in an unstable-resonator configuration. With the amplifier configuration depicted in Fig. 2-8, so-called a multipass amplifier [38,40], 2- μ J pulses were obtained, which could be focused to provide about one order of magnitude higher intensity than the threshold of continuum generation.

In this amplifier, the incident dye laser pulses were focused by the first lens L1 into a flow cell of gain dye solution (*ca.* 3×10^{-4} mol/l of rhodamine 640 perchlorate). Several solvents were examined, as described later. The flow dye cell was 3-mm thick and anti-reflection coated for broadband between 400 and 700 nm. The flow rate of the dye solution was high enough to exchange the gain medium between each shot of CVL pump. It was *ca.* 14 l/min., which corresponds to (800 μ m)/(100 μ s), whereas the spot size of CVL was *ca.* 1 mm. The incidence angle of the pump beam to the flow dye cell was relatively large, *ca.* 20°, to prevent lasing of the dye amplifier itself. The dye laser beam was almost normally reflected back for the second pass by the mirror located just behind the dye cell, focused into the dye cell again for the third pass by the lens L2, and reflected back again in the same way for the fourth pass. Then, the pulse was focused into a saturable absorber jet (malachite green / ethylene glycol, *ca.* 1×10^{-3} mol/l) to suppress the amplified spontaneous emission (ASE). After propagating through the dye cell for the last two passes, the beam was collimated and passed through a four-prism sequence made of SF11 glass to recompress the pulse broadened by the dispersion in several optical elements of the amplifier stage. In this



- G : Gain dye (Rhodamine 640) flow cell (3 mm)
 SA : Saturable absorber (Malachite Green) jet (500 μm)
 M1-9 : Enhanced aluminum coated mirrors
 M10,11 : Dielectric coated high-reflectance mirrors
 L1-6 : Lenses (L1: f300, L2: f250, L3: f40, L4: f40,
 L5: f600, L6: f400)
 A : Aperture
 Prisms : SF11

Figure 2-8 Configuration of amplifier

configuration, because mirrors M2, M3, M4, and M5 forms a nearly closed cavity, strong ASE was easily generated. In order to prevent this phenomenon the incidence angle to the mirror M2 was set as large as possible and an aperture was placed between M3 and M4. In addition, sometimes, a sharp-cut glass filter (R62, Toshiba) was introduced between M3 and M4. Because the center wavelength of ASE was about 605 nm, it could be removed efficiently by this filter from amplified pulses, which were centered around 620 nm. By these means, the energy of ASE was suppressed to less than 0.5 % of the total pulse energy.

The total gain of the amplifier was dependent on the solvent of the gain dye and the incident pulse energy of the CVL pump. The dependence is shown in Table 2-2. As solvents, water, methanol, and their mixture were used. The dye concentration was $ca. 3 \times 10^{-4}$ mol/l in all the cases. Ammonyx LO, an aqueous solution of N,N-dimethyldodecylamine-N-oxide, was added in order to prevent the dye compound from forming aggregates in water. Otherwise, the excited state in the dye molecule is quenched by a charge-transfer interaction in the dye aggregates [95]. In the case of 2-vol% aqueous solution of Ammonyx LO, the gain was relatively low probably because of the low solubility of the dye. When methanol, which dissolves the dye better than water, was used as the solvent, the gain was higher. However, there were a few problems. One was optical damage produced at the inner surface of the flow cell. This damage was prevented by adding a few percent of the surface surfactant, Ammonyx LO. The cause of this damage is not well understood, but, presumably, it is because of adhesive interaction between the surface of the cell and the dye molecules, which absorb high energy of the pump pulse. The second problem was a distortion of the spatial pattern of the amplified beam because the refractive index of methanol is more sensitive to temperature than that of water. The last problem was rapid degradation of the dye solvent within 25 hours of operation. In

Solvent	CVL Input / mJ	Output / μ J	Life of Dye / hr.
• H ₂ O + Ammonyx LO (2 vol%)	1.4	1.5	≥ 500
• MeOH	0.5	2	~ 25
• MeOH / H ₂ O 1/3(v/v) + Ammonyx LO (2 vol%)	0.8	2	≥ 500
• H ₂ O + Ammonyx LO (20 vol%)	0.6	2	≥ 500

• H ₂ O + Ammonyx LO (30 %)	1.8	50 *	

* : Reference [40]

Table 2-2 Dependence of amplified pulse energy on dye solvents

order to overcome these problems, a solvent of a mixture of methanol and water (1:3 in volume fraction) containing 2-vol% Ammonyx LO was tested and it provided fairly good efficiency and stability. On the other hand, Nickel *et al.* reported that they could obtain 50 μ J pulses with water containing 30 % Ammonyx LO as a dye solvent [40], which contains the surface surfactant of higher fraction. With a solvent similar to this condition, gain as high as in the case of methanol was achieved without losing a long lifetime of the dye. However, because the increase in the pump intensity leads to a higher fraction of ASE and saturation of the gain, the ASE-free output-pulse energy is limited to 2 μ J so far [96].

In typical cases, the gain of each pass measured by the magnitude of the peak signal of a PIN photodiode's output was about 20 for from the first to the third passes, and was about 6 for the fourth pass. This decrease in gain is due to saturation at this stage. The total gain in energy after four passes was about 5,000 and the fraction of ASE was about 20 %. By focusing the pulses into a saturable absorber jet, the pulse energy was reduced by about a factor of 3 and ASE was suppressed to much less than 1 %. The gain in energy for the last two passes was 4-5 and 2-3 in the fifth and the sixth passes, respectively. Hence, the total energy gain was about 20,000. In order to increase the gain more than the present one, it is necessary to achieve better configuration to remove ASE generation. For the sake of suppression of the gain saturation, dividing the amplifier into two parts, *i.e.*, a pre-amplifier with a smaller focus spot of CVL pump and a power-amplifier with a larger spot size, would work well [97,98].

Synchronization of CVL with the dye laser was achieved by the following way as illustrated in Fig. 2-9. The dye laser pulse train was detected by a fast PIN photodiode (S2840, Hamamatsu), of which rise time is shorter than 1 ns. Its output electric signal was transferred to a synchronization circuit. In this circuit the output of

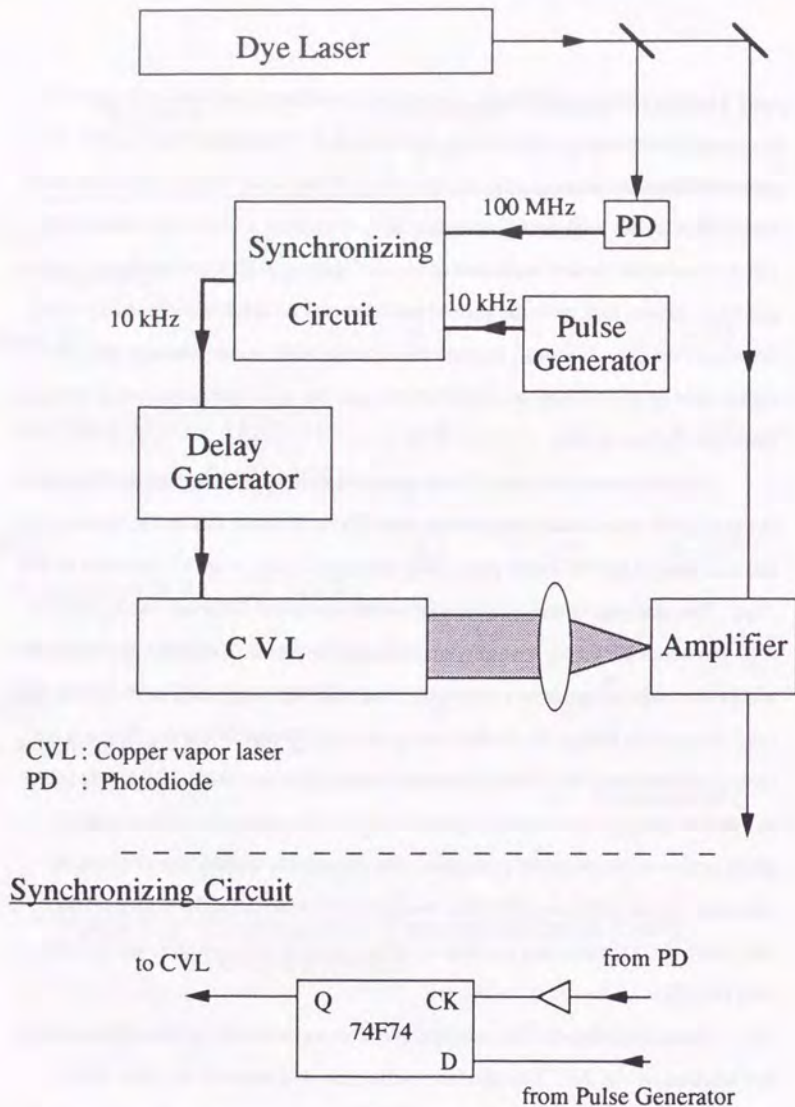
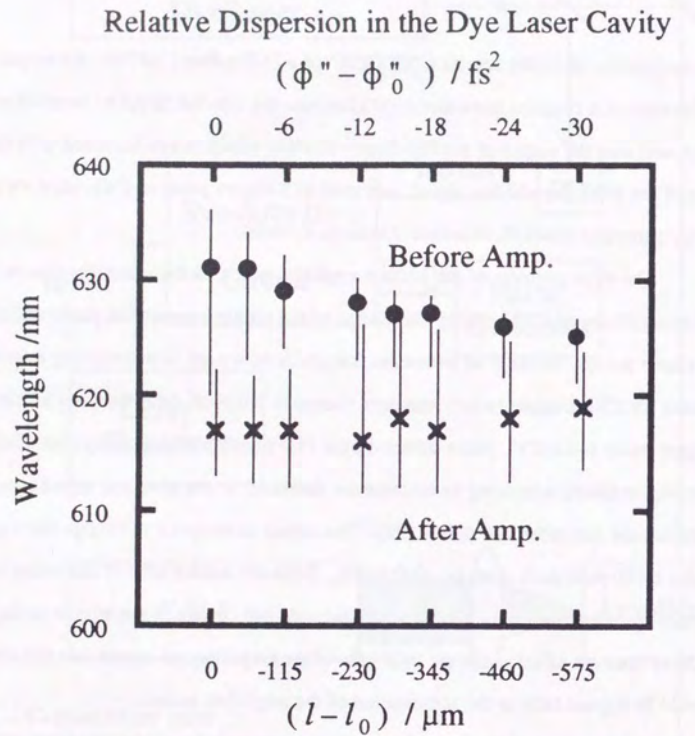


Figure 2-9 Schematic of synchronization of copper vapor laser with dye laser

photodiode (~100 MHz) acts as a "CLOCK" of a D-flip-flop (74F74). An output pulse train of a function generator (~10 kHz) was fed into the "DATA" terminal of the chip, and then the output of the flip-flop (~10 kHz), which is synchronized with the rise of the PIN photodiode's signal, was used as a trigger pulse of CVL via a variable delay generator (DG535, Stanford Research Systems).

The main problem of the present amplifier system is the instability due to drift of lasing timing of CVL causing the change of the timing between the pump and the dye laser pulses. In order to overcome this problem, we are now designing a feedback circuit for CVL triggers, which monitors change in temporal delay between an electric trigger pulse and a CVL pulse detected by a PIN photodiode and delays (or advances) the trigger timing according to increase (or decrease) in the temporal separation between the two reference pulses [99]. The circuit is designed to change the trigger delay by 50 ps at each shot, *i.e.*, 500 ns/1 s. Since the sudden drift in the lasing timing causes the change in delay by a few nanoseconds and change in the trigger timing by ± 50 ps does not affect much the total gain of the amplifier, we expect that this circuit would be a great help to the stabilization of the amplified pulses.

As described in the preceding section, characteristics of the dye laser output, such as pulse durations and spectra, vary substantially when the amount of intracavity dispersion controlled by the position of the internal prisms is changed. This change in the dye laser output also affects the properties of the amplified pulses. The dependence of the pulse durations and spectra of amplified pulses on the dye laser output is discussed in the following. Figure 2-10 shows the dependence of spectral peak and width of pulses both before and after amplification on intracavity dispersion of the dye laser. The spectra of pulses before and after amplification are shown in Fig. 2-11 for three different amounts of intracavity dispersion. This spectral dependence might be because the peak of ASE of the amplifier lies around 605 nm and



- : Before amplification.
- × : After amplification.
- Bars indicate FWHM of spectra.

Figure 2-10 Dependence of laser spectra on intracavity dispersion of dye laser

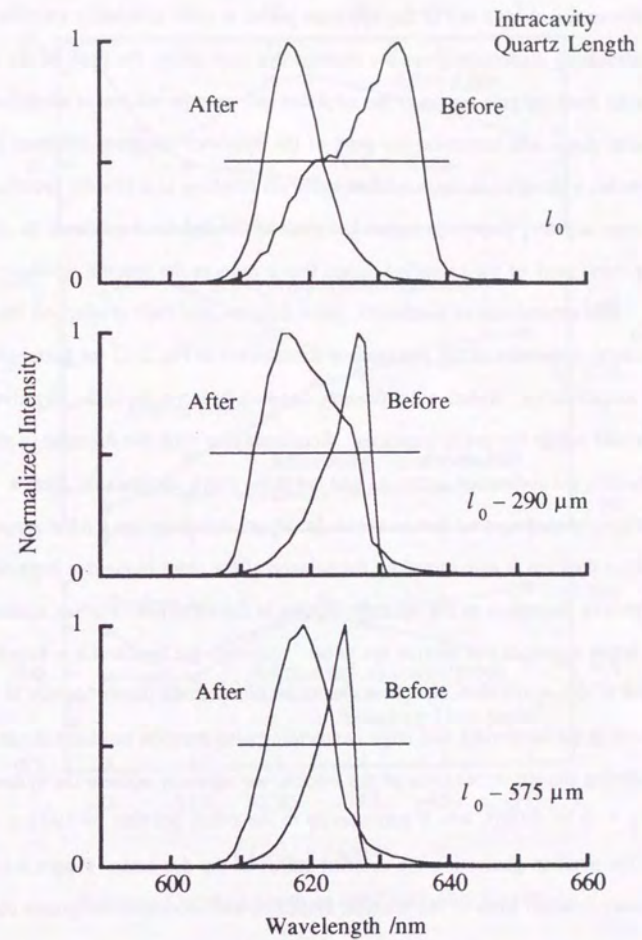
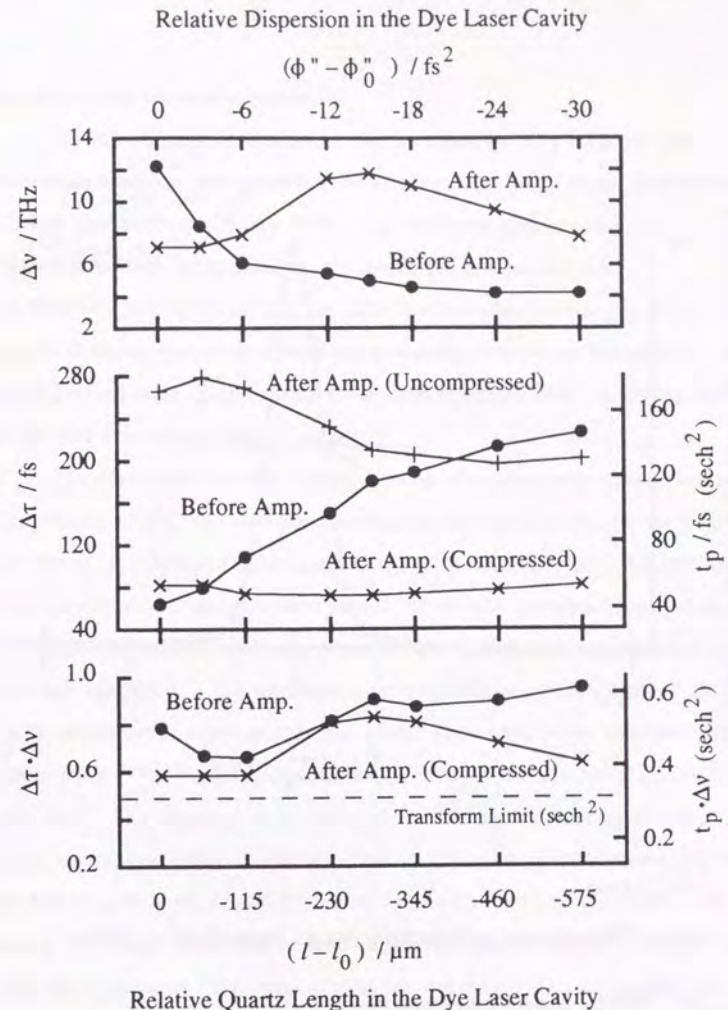


Figure 2-11 Spectra of pulses before and after amplification

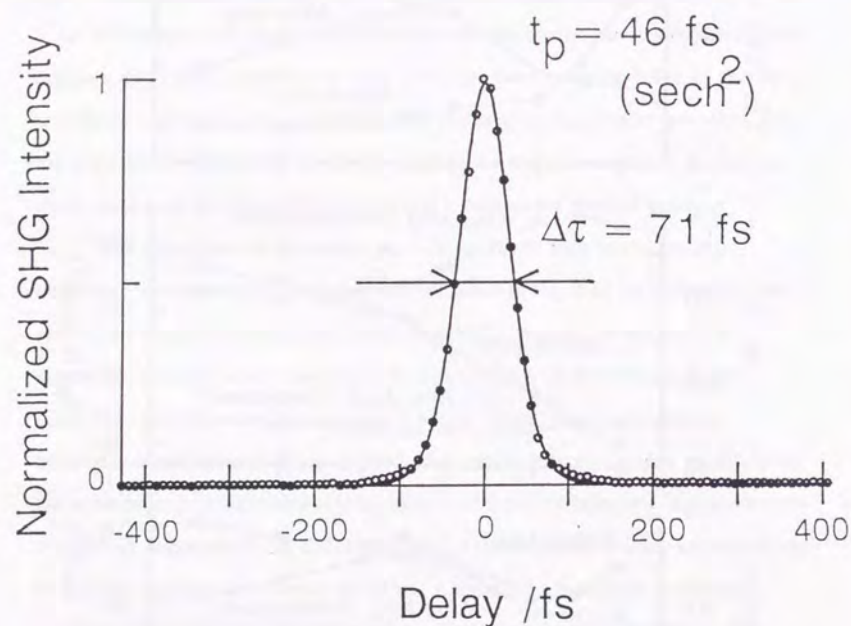
the shorter-wavelength tail of the dye laser pulses is more efficiently amplified. When the intracavity dispersion gives the shortest dye laser pulse, the peak of the spectrum is too far from the gain region of the amplifier and only the tail part is amplified. As the negative dispersion increases, the peak of the dye-laser spectrum becomes shorter and makes a shoulder in the amplified spectrum resulting in a broader spectrum. But too large negative dispersion makes the peak of the dye-laser spectrum so close to the spectral peak of the amplified pulses that it reduces the spectral width.

The dependence of bandwidth, pulse duration, and their product on the intracavity dispersion of the dye laser is summarized in Fig. 2-12 for both before and after amplification. Before amplification, bandwidth decreases as the negative dispersion inside the cavity increases. Accompanying with the decrease in the bandwidth, pulse duration increases and the pulse shape becomes far from a hyperbolic-secant squared one as shown in the preceding section. After amplification, the pulse duration is determined by the balance of the chirp in the dye laser output and the positive dispersion of the optical elements in the amplifier. Further recompression by a prism sequence can shorten the pulse. Although the bandwidth is broadest around $\phi'' - \phi''_0 = -15$ (fs)², the pulse cannot be compressed proportionally to the increase in the bandwidth and large bandwidth-pulse duration products result. By considering the above behavior of the system, we normally operate the system at $\phi'' - \phi''_0 = -3$ to -6 (fs)², which corresponds to the prism position 50-100 μm extracted from the position generating the shortest pulses of the dye laser. Figure 2-13 shows an autocorrelation trace of the shortest amplified and recompressed pulses obtained so far.



$\Delta\nu$: FWHM of power spectrum $\Delta\tau$: FWHM of autocorrelation trace
 t_p : FWHM of intensity profile for hyperbolic-secant squared pulses

Figure 2-12 Dependence of spectral width, pulse duration, and their product on the intracavity dispersion of the dye laser



○ : Data

— : Fitting curve for hyperbolic-secant squared pulses shape

$\Delta\tau$: FWHM of autocorrelation trace

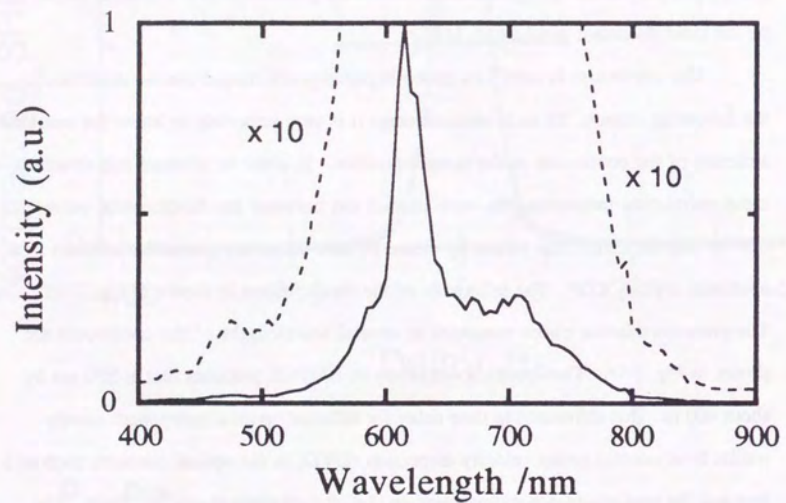
t_p : FWHM of intensity profile for hyperbolic-secant squared pulses

Figure 2-13 Background-free SHG autocorrelation of amplified pulses

2.5. White-light continuum pulses

By focusing the amplified pulses into an ethylene glycol jet, femtosecond white-light continuum was obtained, extending from wavelength shorter than 400 nm to longer than 1000 nm as shown in Fig. 2-14. The mechanism of continuum generation has been investigated for picosecond and femtosecond pulses [48,100-104]. Spectral broadening can arise from self-phase modulation (SPM), stimulated Raman scattering, cross-phase modulation, four-photon parametric generation, and so on. In femtosecond continuum generation SPM has been known to be the most dominant mechanism [48].

The continuum is used as a probe in pump-probe measurements described in the following section. In such measurements it is very important to know the temporal structure of the continuum at the sample position. In order to measure this structure, cross-correlation measurements were carried out between the fundamental pulses at 620 nm and the continuum pulses by means of sum-frequency generation of them in a nonlinear crystal, KDP. The schematic of the measurement is shown in Fig. 2-15. The cross-correlation traces measured at several wavelengths of the continuum are shown in Fig. 2-16. The spectral component at 1000 nm precedes that at 550 nm by about 400 fs. This difference in time delay for different spectral component mainly results from normal group velocity dispersion (GVD) in the optical elements such as a lens and the continuum-generating medium, *i.e.*, the ethylene glycol jet, itself. The relative time delays of the peak of cross-correlation traces are plotted in Fig. 2-17 as a function of frequency. The fitting of these data including GVD effect explains this behavior fairly well. However, the data deviate from this fitting curve around the wavelength of the fundamental pulses, 620 nm. Similar behavior has also been reported more clearly in Ref. [48]. This deviation is expected to be due to the SPM process, which is dominant in femtosecond continuum generation. The mechanism of



Sensitivity of the detection system is not compensated for.

Figure 2-14 Spectrum of continuum

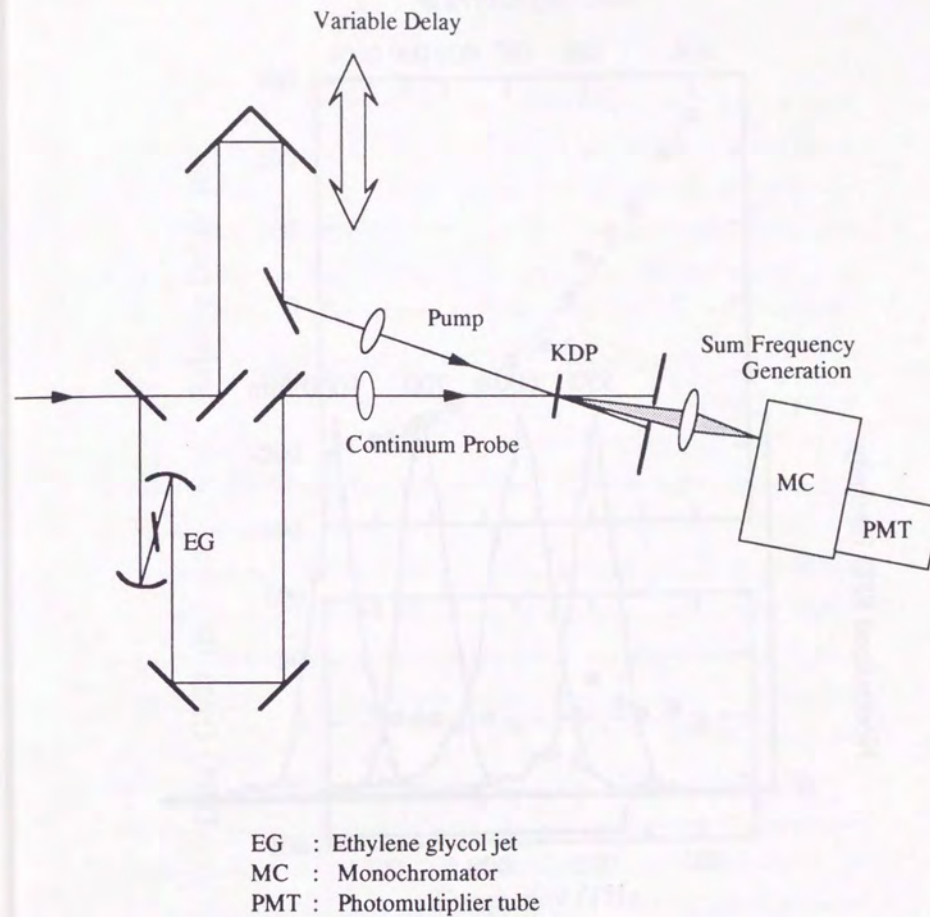


Figure 2-15 Schematic of cross-correlation measurement

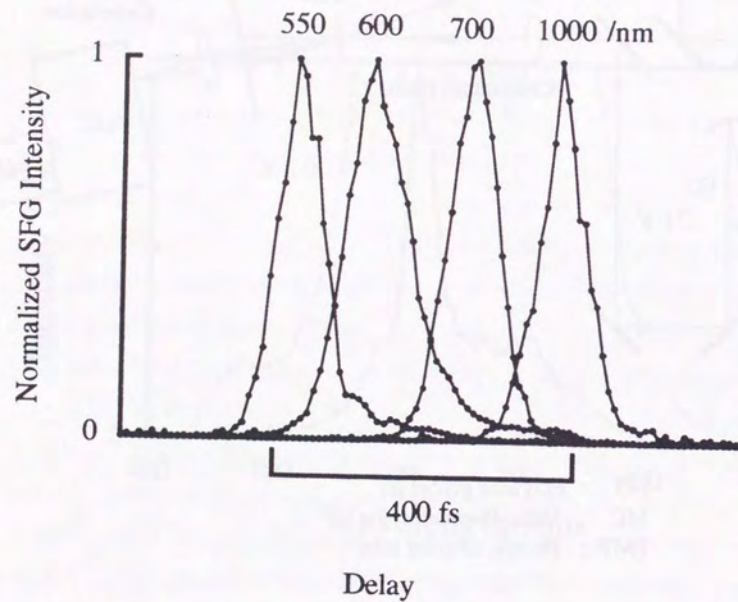
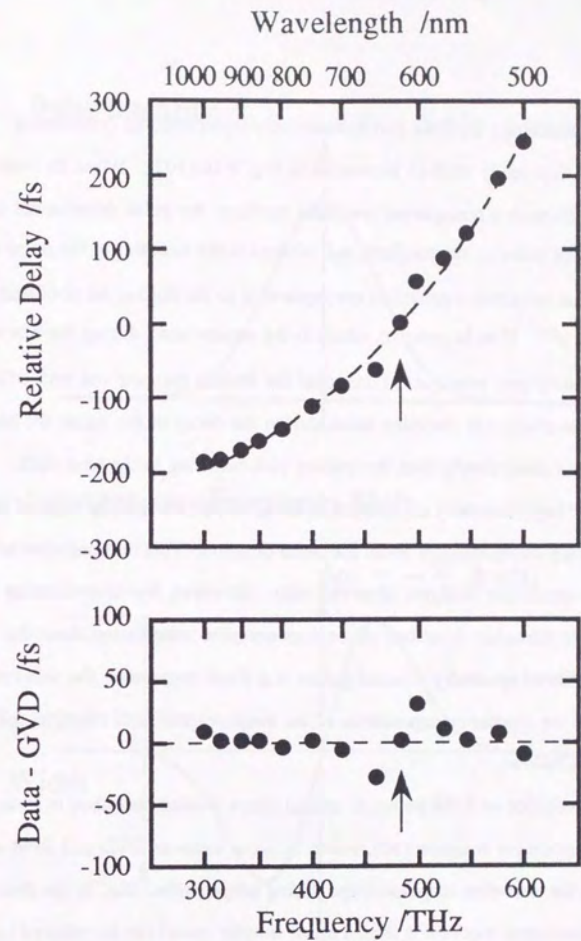


Figure 2-16 Cross-correlation traces



- Data
 - Dependence calculated by group velocity dispersion (GVD)
- Arrows indicate the fundamental wavelength 620 nm.

Figure 2-17 Relative delay of continuum as a function of frequency

the spectral broadening by SPM can be intuitively understood by considering instantaneous frequency shift as illustrated in Fig. 2-18 [102]. When an intense pulse passes through a transparent nonlinear medium, the pulse experiences change in the refractive index of the medium, $n_2 I$, where I is the intensity of the pulse and n_2 is the nonlinear refraction coefficient corresponding to the third-order nonlinear optical susceptibility $\chi^{(3)}$. If n_2 is positive, which is the present case, during the rise of the pulse, the leading part propagates faster than the trailing part and red shift of the spectrum takes place. On the other hand, during the decay of the pulse, the leading part propagates more slowly than the trailing part, resulting in the blue shift. Therefore, the high frequency component of the SPM pulse originally delayed from the lower frequency component by about the pulse duration. This interpretation is qualitatively consistent with the observed data. However, the instantaneous frequency approximation described above does not offer information about the temporal profile of spectrally selected pulses at a fixed frequency. For this reason, the calculation of the frequency dependence of the temporal profile of the SPM pulse was carried out as follows.

The evolution of SPM pulses in optical fibers is often described in terms of the nonlinear Schrödinger equation [50], which includes terms of GVD and SPM to take into account the evolution of pulse shape during propagation. But, in the present case, because the nonlinear medium is thin, a much simpler model can be adopted by neglecting the propagation effect. That is, we calculate frequency dependence of electric field of a pulse including chirp caused by SPM and filter out a portion of it centered at a certain frequency. Then, by Fourier transformation of this filtered electric field, a temporal profile of the pulse intensity at the selected frequency can be obtained.

The electric field of the SPM pulse is written in time domain as follows:

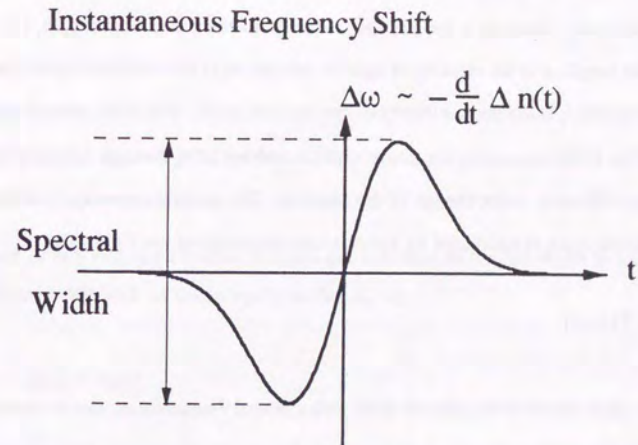
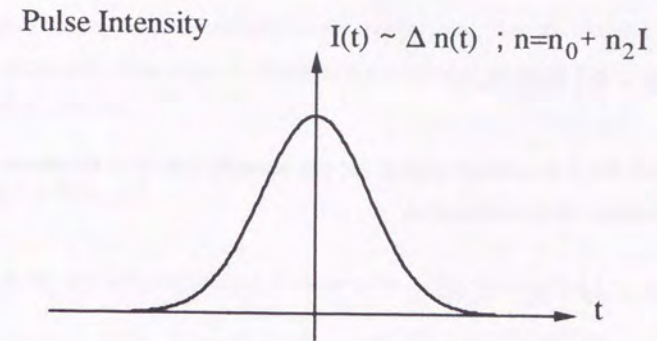


Figure 2-18 Instantaneous frequency shift model of self-phase modulation

$$E(t) = \tilde{E}(t) \exp[-i \cdot \varphi(t)] \quad (2-7)$$

where $\tilde{E}(t)$ is an envelope function and $\varphi(t)$ represents a phase of the electric field. The phase can be expressed as

$$\varphi(t) = \omega_0 t - \varphi_0 - \varphi_2 \cdot \hat{I}(t) \quad (2-8)$$

where $\varphi_0 = \omega_0 \cdot (l/c) \cdot n_0$, $\varphi_2 = \omega_0 \cdot (l/c) \cdot n_2 I_0$, and $\hat{I}(t)$ is pulse intensity normalized to unity at its peak. Here ω_0 is the angular frequency of the center wavelength, l is the interaction length, c is the velocity of light in vacuum, n_2 is the nonlinear refraction coefficient, and I_0 is the peak intensity of the incident pulse. The third term of the r.h.s. of Eq. (2-8) represents the phase shift caused by SPM through intensity-dependent refractive index change of the medium. The spectral dependence of this electric field, $\epsilon(\omega)$, is expressed by Fourier transformation of the field $E(t)$:

$$\epsilon(\omega) = \mathcal{F}[E(t)] \quad (2-9)$$

The time dependence of the electric field with a central frequency ω_c can be obtained by inverse Fourier transformation of spectrally filtered electric field in frequency domain as follows:

$$E(t, \omega_c) = \mathcal{F}^{-1}[\epsilon(\omega) \cdot f(\omega - \omega_c)] \quad (2-10)$$

where $f(\omega)$ is a bell-shaped filtering function peaked at zero. Then the temporal profile of the pulse intensity can be calculated as a function of the center frequency of the spectral filter, ω_c :

$$I(t, \omega_c) \propto |E(t, \omega_c)|^2 \quad (2-11)$$

In the following calculation a Gaussian pulse profile was assumed, *i.e.*,

$$\tilde{E}(t) = \exp[-2(\frac{t}{\Delta t})^2] \quad (2-12)$$

and

$$\varphi(t) = \omega_0 t - \varphi_0 - \varphi_2 \cdot \exp[-4(\frac{t}{\Delta t})^2] \quad (2-13)$$

where Δt is a measure of pulse duration and is related to the full width at half maximum (FWHM) of the intensity profile, t_p , by

$$\frac{t_p}{\Delta t} = \sqrt{\ln 2} \cong 0.833 \quad (2-14)$$

The spectral-filter function was also assumed to have a Gaussian profile, *i.e.*,

$$f(\omega) = \exp[-\frac{1}{8}(\frac{\omega}{\delta\omega})^2] \quad (2-15)$$

where $\delta\omega$ is a measure of its spectral width. The maximum phase shift, φ_2 , was assumed to be 2, which is reasonable in our experimental condition, where $n_2 I_0$ was of the order of 10^{-4} and the interaction length was about 1 mm.

Results of calculation are shown in Fig. 2-19 for the filter bandwidth, $\delta\omega \cdot \Delta t = 1$. It is clear that the peak of the intensity profile changes rapidly by about $0.7t_p$ around the center frequency $\nu_0 \pm 0.5/t_p$. Although what was observed is not a pulse-intensity profile of filtered continuum itself but its cross-correlation with fundamental pulse shape, a similar structure should appear also in the cross-correlation data. By taking into account this effect the data could be fitted much better as shown in Fig. 2-20.

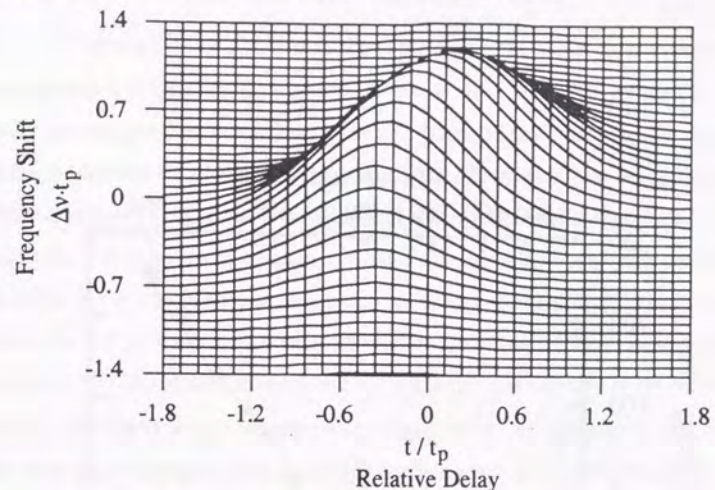
2.6. Measurement techniques

This section describes the experimental setups we have constructed for the research of ultrafast phenomena. One is a system for degenerate four-wave mixing measurements and the other is for pump-probe measurements. Detailed theoretical treatments of these measurements will be described in the following chapter. The present femtosecond laser source has been utilized several other ways, such as Kerr shutter measurements, optical-heterodyne-detected induced phase modulation (OHD-IPM) measurements [105], and interferometric measurements.

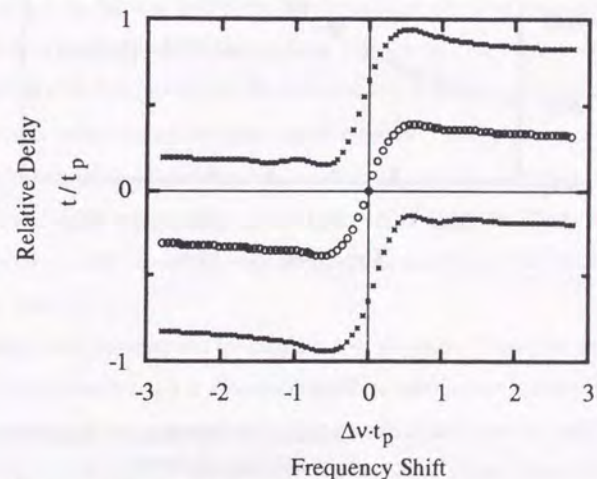
2.6.1. Degenerate four-wave mixing

The principle of this technique is that three incident pulses interact among themselves in a sample, of which nonlinearity generates a fourth pulse. By delaying one of the incident pulses relative to the other two, the temporal evolution of the nonlinearity can be measured.

Dependence of temporal intensity profile on frequency shift



Temporal peak (○) and half maximum (×)



Frequency filter width $\delta\omega \cdot \Delta t = 1$.

t_p : FWHM of intensity profile of Gaussian pulse.

Figure 2-19 Calculation of frequency dependent temporal distribution of self-phase modulated pulses

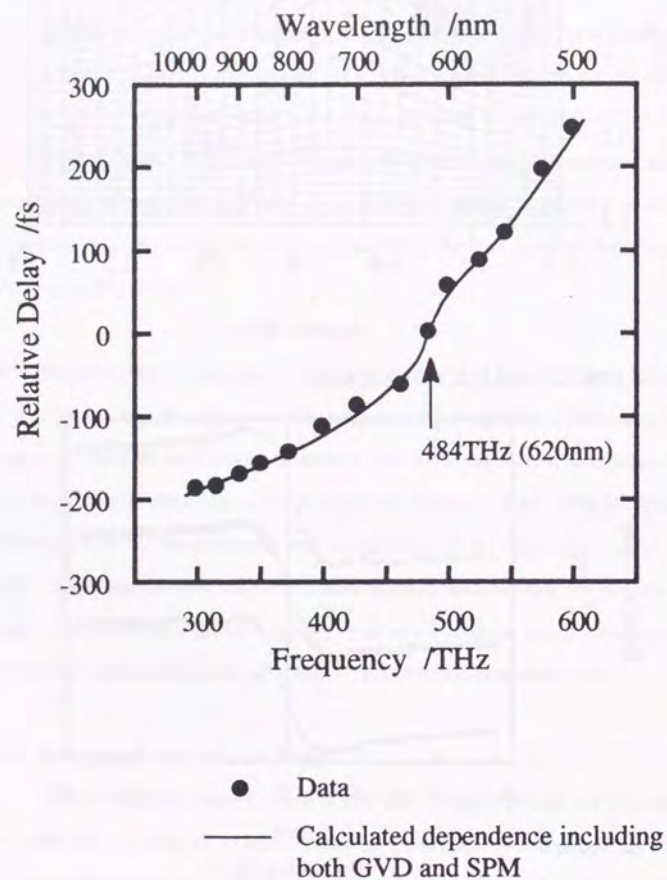
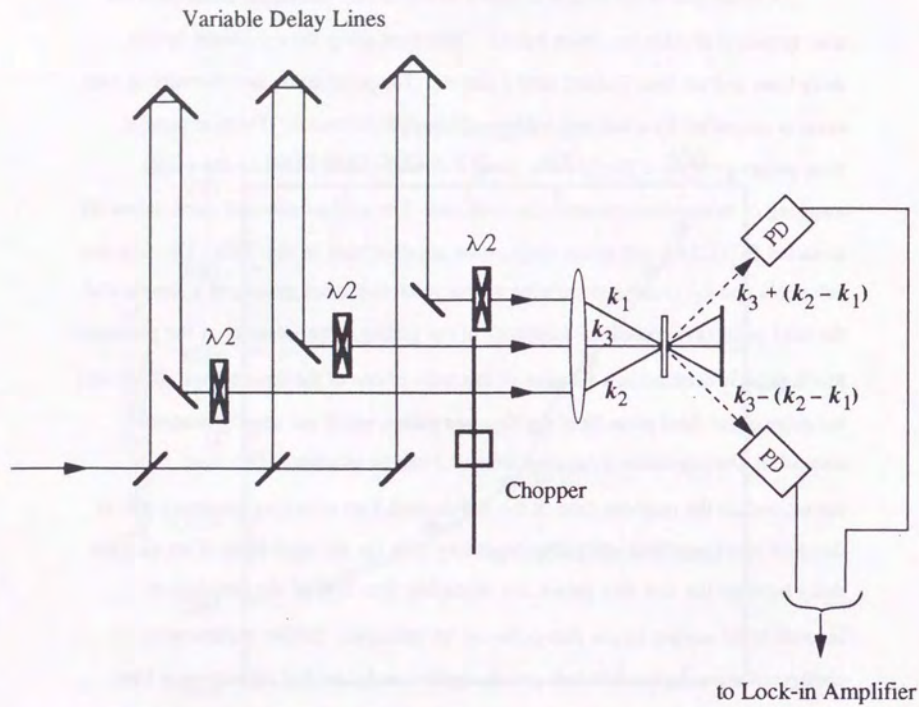


Figure 2-20 Fitting of chirp in continuum

A schematic of the system is shown in Fig. 2-21. The output beam from the laser system is divided into three beams. They pass along three different optical delay lines and are then focused onto a sample. The polarization and intensity of each beam is controlled by a half-wave plate-polarizer combination. These sequential three pulses generate a fourth pulse along a direction determined by the phase-matching or momentum-conservation condition. The configurations of these beams for so-called BOXCARS and phase conjugation are illustrated in Fig. 2-22. The first two pulses (k_1 and k_2) create a population and/or refractive-index grating in a sample and the third pulse (k_3) probes the amplitude of the grating. The intensity of the generated fourth pulse is detected as a function of the delay of one of the three beams. If we vary the delay of the third pulse from the first two pulses, which are usually temporally coincident, the population-relaxation time (T_1) can be obtained. This time corresponds to the response time of the real (optical Kerr effect) or imaginary part of the third-order nonlinear optical susceptibility $\chi^{(3)}$. On the other hand, if we vary the delay between the first two pulses, the dephasing time (T_2) of the polarization induced in the sample by the first pulse can be measured. Similar experimental configurations using two incident pulses, such as two-pulse self diffraction, a Kerr shutter, and also the pump-probe, are the special cases of the three-incident-pulse configuration, in which one of the two incident pulses contributes twice to the nonlinear process.

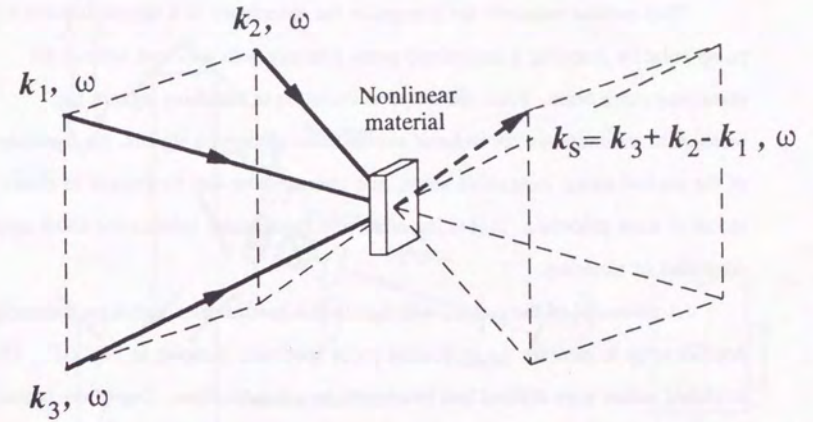
Detection was performed by using a lock-in amplifier. Two of the three incident beams were blocked at different frequencies by a chopper and their sum frequency was used as a reference of the phase sensitive detection. A small portion of the laser output was split off and detected by a photodiode whose output signal passed through a low-pass filter with a time constant of the lock-in amplifier, and was used to monitor laser-intensity fluctuation.



PD : Photodetector

Figure 2-21 Schematic of a degenerate four-wave mixing system with three incidence pulses

a) Folded BOXCARS Configuration



b) Phase-Conjugation Configuration

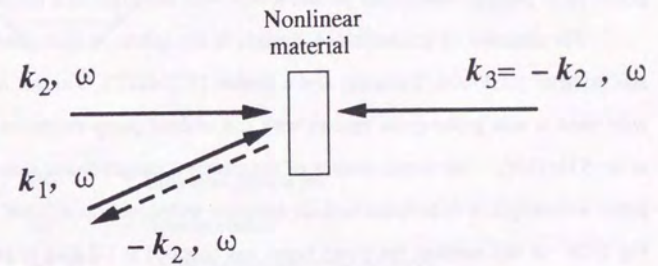


Figure 2-22 Beam configurations of degenerate four-wave mixing

2.6.2. Pump-probe measurement

This method measures the changes in the absorbance of a sample induced by a pump pulse by detecting a transmitted probe intensity both with and without the perturbing pump beam. From the temporal evolution of bleaching signals, *i.e.*, increase in transmittance, or induced excited-state absorption signals, the dynamics of the excited states, metastable states, and intermediates can be studied to obtain a model of these processes. This is important and fundamental information about optical properties of materials.

A schematic of the system, which utilizes a spectrometer with a multichannel detector array to measure the continuum probe spectrum, is shown in Fig. 2-23. The amplified pulses were divided into two beams by a beam splitter. One of the beams was used as a pump and focused onto the sample after passing through a variable optical delay line. A half-wave plate – polarizer combination was used to vary polarization and intensity of this beam. The other beam was focused into an ethylene glycol jet to generate continuum pulses, which were then used as a broadband probe.

For detection of transmittance changes in the spectra, a multichannel spectrometer (USP-500, Unisoku) and a shutter (VS14S2T1, Vincent Associates) were used to take probe-pulse spectra with and without pump excitation alternatively at *ca.* 5 Hz [106]. For measurements of the transient transmittance change at a fixed probe wavelength, a differential lock-in detection technique was utilized, as shown in Fig. 2-24. In this method, the pump beam was chopped at 1-2 kHz to generate a reference frequency. A portion of the probe was split off before the sample, spectrally filtered, and then compared with probe light of the same wavelength which had passed through the sample. A small portion of the excitation beam was split off and its average power was monitored to discriminate signals. The chirp in the probe continuum was measured by cross-correlation traces obtained by the sum-frequency

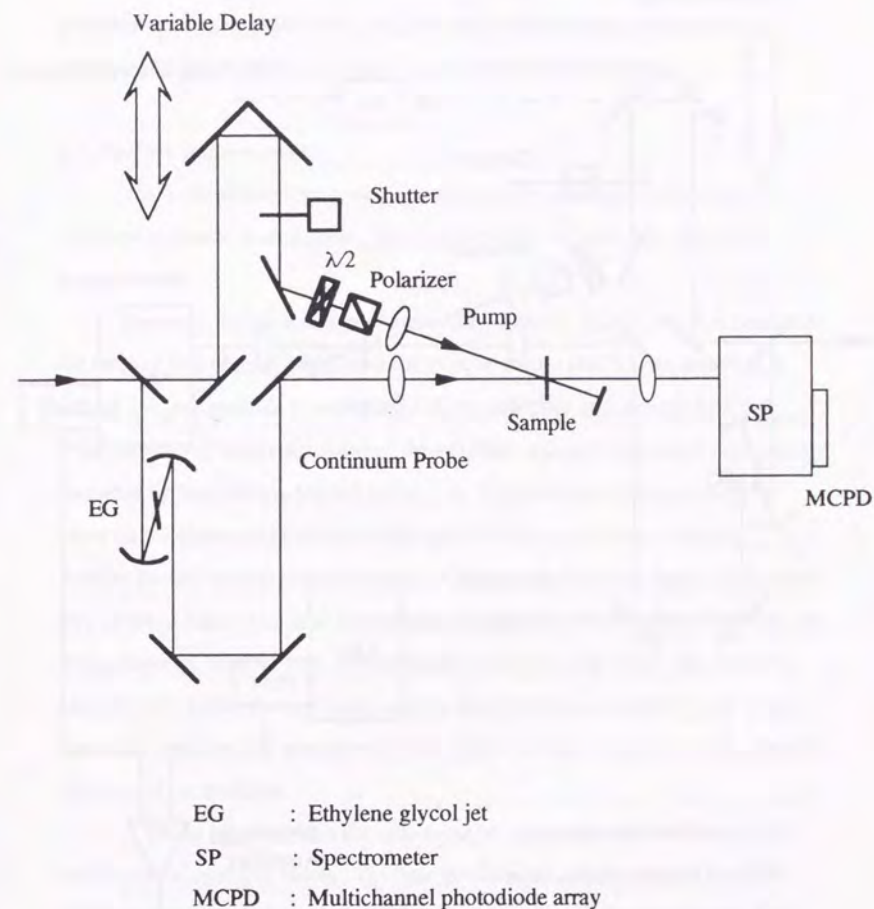


Figure 2-23 Schematic of a pump-probe system using a multichannel photodetector

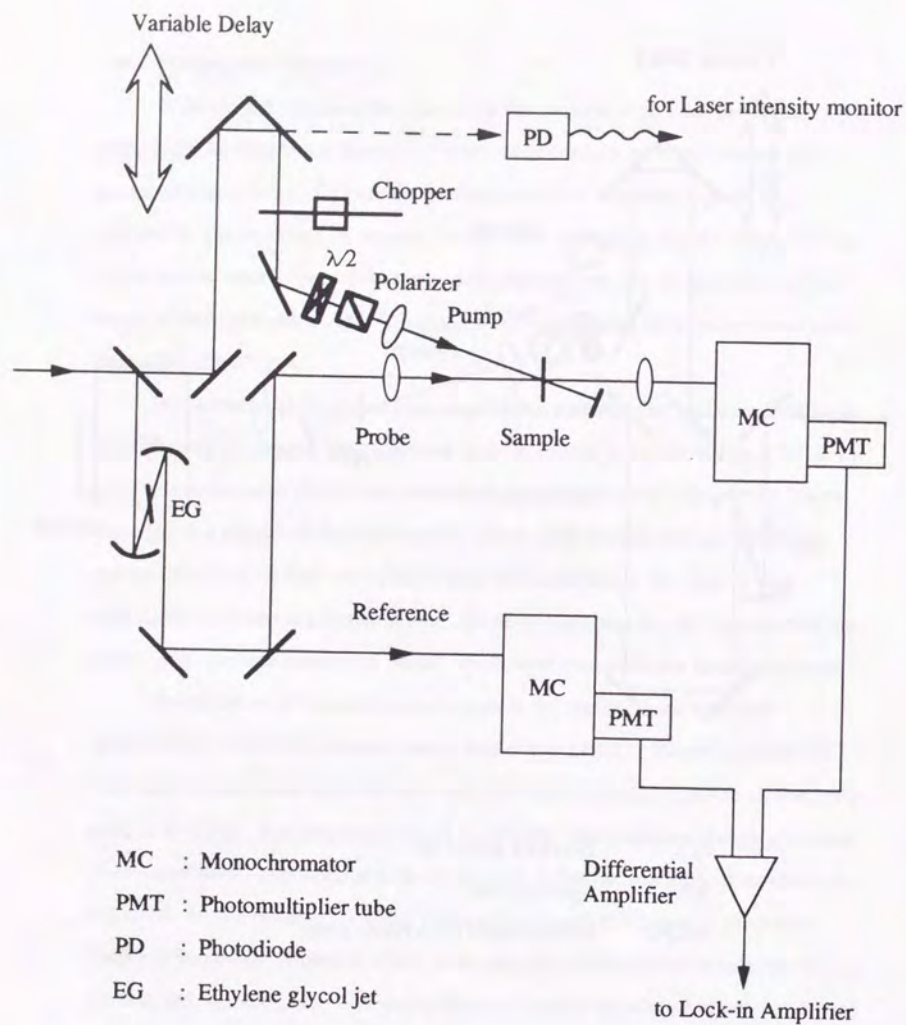


Figure 2-24 Schematic of a pump-probe system for single wavelength measurements

generation of the pump and probe, as described in the preceding section, and subsequently removed from the data in a data processing procedure.

2.7. Further improvements

The femtosecond laser system described in the preceding sections can be improved and made more flexible. This section points out some possible further improvements.

Presently, the pulse energy of amplified pulses is 1 to 2 μJ , which is lower than the value of tens of microjoules reported by other groups [40,78]. As described in Section 2.4., one possible reason is the efficient amplified spontaneous emission (ASE) because of the configuration of the amplifier, especially the nearly closed cavity formation by four mirrors, M2-M5 in Fig. 2-8. This problem will be solved by changing the alignment to such a configuration without quasi-cavity formation. Another possible reason is the saturation of the gain at the latter stages. One simple way to obtain higher gain is to increase the gain dye concentration [96]. However, for the fundamental improvement, it is preferable to use two gain media, one for a pre-amplifier with tightly focused beams and the other for a power amplifier with larger spot size to prevent gain saturation [97,98]. Either of these methods will improve the total gain of the amplifier.

A second way, in which the system can be improved, is by increasing the stability of the amplified pulses. The main problems are now the trigger jitter and timing drift of the thyatron of CVL. As described in Section 2.4., we are now designing a feedback circuit which stabilizes the temporal delay between electric trigger pulses and CVL output pulses [99]. This circuit should provide short and long term stabilities not only of the intensity but also of the spectrum.

Third, the detection scheme can be improved. In single wavelength experiments, phase-sensitive detection with a lock-in amplifier is used in the present system. However, in experiments using amplified pulses, the repetition rate of 10 kHz is low enough for each pulse to be detected individually with a photodiode and a commercially available fast analog-to-digital (A/D) converter. This shot-by-shot detection technique provides fine data discrimination, and will result in higher sensitivity and signal-to-noise (S/N) ratio.

Fourth, the amplified-pulse duration, *ca.* 50 fs, can be reduced by pulse compression techniques [1], thus permitting higher time resolution. Short pulses provide a broader continuum spectrum with smaller chirp. This makes pump-probe data more accurate and reliable.

Last, laser tunability is needed for the studies of various systems with different transition photon energy. A second amplifier to amplify a selected wavelength region of continuum pulses is under construction [44,73,74]. The CVL output is divided into two pump beams, one of which is used for the first amplifier and the other for the second continuum amplifier after an optical delay line for the CVL pulse to coincide with the output pulse of the first amplifier. The output pulses of the first amplifier are recompressed by a four-prism sequence and focused into an ethylene glycol jet to generate continuum pulses. The preferred spectral component of the continuum is picked out by an interference filter with a spectral width of *ca.* 10 nm, and fed into the second amplifier. So far, a single-pass gain of *ca.* 10 has been achieved at 750 nm with LDS 751 as a gain dye and 5-W CVL pump power. We expect that this system, along with suitable dyes, will provide tunability ranging from 550 to 800 nm. A much simpler alternative method can be used if we have a high enough output from the first amplifier. This scheme utilizes a travelling-wave amplifier arrangement [76-78].

The implementation of all of these improvements is a long-term goal, which will make the present femtosecond laser system a much more reliable and flexible system.

CHAPTER 3

THEORY OF MEASUREMENTS

In measurements using ultrashort light pulses, the observations are based on nonlinear optical processes. This chapter outlines a perturbation theory used to describe such light-matter interactions.

3.1. Third-order nonlinear polarization

What is measured in ultrafast spectroscopies can be described, in the lowest-order approximation, by the third-order nonlinear optical processes. We outline the theory for these processes in a two-level system for simplicity. In a two-level system interacting with electric fields, the third-order nonlinear polarization arises as the lowest-order nonlinear polarization, which emits radiation or modulates another electric field. This phenomenon can be treated by perturbative solution of density matrix equations.

For a two-level system, whose ground and excited states are represented as $|1\rangle$ and $|2\rangle$, respectively, the evolution of density operator, $\hat{\rho}$, can be described by the following Liouville equation:

$$\frac{\partial \hat{\rho}}{\partial t} = \frac{i}{\hbar} [\hat{\rho}, \hat{H}] + \left(\frac{\partial \hat{\rho}}{\partial t}\right)_{\text{relax}}, \quad (3-1)$$

where

$$\hat{H} = \begin{pmatrix} H_{11} & H_{12} \\ H_{21} & H_{22} \end{pmatrix} = \hat{H}_0 + \hat{H}', \quad (3-2)$$

$$\hat{H}_0 = \begin{pmatrix} 0 & 0 \\ 0 & \hbar\Omega \end{pmatrix}, \quad (3-3)$$

$$\hat{H}' = -\bar{\mu} E(r,t) = \begin{pmatrix} 0 & H_{12}' \\ H_{21}' & 0 \end{pmatrix} = -E(r,t) \begin{pmatrix} 0 & \mu \\ \mu & 0 \end{pmatrix}, \quad (3-4)$$

and $(\partial \hat{\rho} / \partial t)_{\text{relax}}$ is a phenomenological function which takes relaxation effects into account. Here \hat{H} is a Hamiltonian of the whole system, \hat{H}_0 is a Hamiltonian of the isolated two-level system with energy separation $\hbar\Omega$, \hat{H}' represents the interaction between the electric field and the two-level system which has a transition dipole moment μ between $|1\rangle$ and $|2\rangle$, and $E(r,t)$ is total incident electric field. The above equation leads to the following set of equations:

$$\frac{\partial \rho_D}{\partial t} = 2 \frac{i}{\hbar} (\rho_{12} H_{21}' - H_{12}' \rho_{21}) - \Gamma (\rho_D - \rho_D^{(0)}), \quad (3-5a)$$

$$\frac{\partial \rho_{21}}{\partial t} = \frac{\partial \rho_{12}^*}{\partial t} = -\frac{i}{\hbar} H_{21}' \rho_D - (\gamma + i\Omega) \rho_{21}, \quad (3-5b)$$

where $\rho_D^{(0)}$ is an equilibrium value of $\rho_D = \rho_{11} - \rho_{22}$, Γ is an inverse of the energy relaxation time T_1 , and γ is an inverse of the phase relaxation time T_2 .

The above sets of equations can be solved in a perturbative way under the initial conditions, $\rho_{21}^{(0)} = \rho_{12}^{*(0)} = 0$ and $\rho^{(n)(-\infty)} = 0$ ($n \geq 1$), according to the procedure $\rho_D^{(0)} \rightarrow \rho_{21}^{(1)} \rightarrow \rho_D^{(2)} \rightarrow \rho_{21}^{(3)}$ when the incident light is one-photon resonant with the transition of the system. We obtain for $\rho_{21}^{(3)}$,

$$\rho_{21}^{(3)}(r,t) = 2 \rho_D^{(0)} \left(\frac{i}{\hbar} \mu \right)^3 \int_{-\infty}^t dt_3 \int_{-\infty}^{t_3} dt_2 \int_{-\infty}^{t_2} dt_1 E(r,t_3) E(r,t_2) E(r,t_1) \\ \times \left[\exp[-(\gamma + i\Omega)(t - t_3) - \Gamma(t_3 - t_2) - (\gamma - i\Omega)(t_2 - t_1)] \right. \\ \left. + \exp[-(\gamma + i\Omega)(t - t_3) - \Gamma(t_3 - t_2) - (\gamma + i\Omega)(t_2 - t_1)] \right]. \quad (3-6)$$

The complex representation of the third-order polarization $P^{(3)}(r,t)$ is related to $\rho_{21}^{(3)}$ as follows:

$$P^{(3)}(r,t) = N \int_0^\infty d\Omega g(\Omega) \mu \rho_{21}^{(3)}(r,t,\Omega), \quad (3-7)$$

where N is a number density of the two levels and $g(\Omega)$ is a distribution function of the transition frequency Ω , which characterizes the inhomogeneous broadening of the system.

This polarization gives rise to a new electric field, whose phase is retarded by $\pi/2$ from the original polarization, according to the Maxwell's equations. The electric field generated by this polarization is observed as light intensity or as modulation of a coupled field. For instance, degenerate four-wave mixing detection using a BOXCARS or phase-conjugation configuration corresponds to the former case, while optical heterodyne detection in pump-probe or degenerate four-wave mixing measurements is the latter case.

When n pulses are present, the total electric field is expressed as

$$E(r,t) = \sum_{j=1}^n \{ \hat{E}_j(t) \exp[ik_j r - i\omega_j t] + \text{c.c.} \}, \quad (3-8)$$

where $\hat{E}_j(t)$ is an envelope function of the j -th electric field including a fixed phase factor depending on the time delay from the origin of time. In this case Eq. (3-6) consists of $(2n)^3/2$ terms and their complex-conjugate terms with various wave vectors and frequencies. Different experiments are carried out to selectively observe a superposition of some of these terms.

3.2. Degenerate four-wave mixing

In the degenerate four-wave mixing depicted in Fig. 3-1, the signal intensity in the direction of $k_4 = k_3 + k_2 - k_1$ with frequency ω is calculated as follows. The incident electric field is expressed as

$$E(r,t) = \{ \hat{E}_1(t) \exp[ik_1 r - i\omega t] + \hat{E}_2(t) \exp[ik_2 r - i\omega t] \\ + \hat{E}_3(t) \exp[ik_3 r - i\omega t] \} + \text{c.c.}, \quad (3-9)$$

where

$$\hat{E}_1(t) = \tilde{E}(t + \tau) \exp[-i\omega\tau], \quad (3-10a)$$

$$\hat{E}_2(t) = \tilde{E}(t), \quad (3-10b)$$

$$\hat{E}_3(t) = \tilde{E}(t - T) \exp[i\omega T]. \quad (3-10c)$$

In the above equations, the delay of pulse 2 from pulse 1 is τ , the delay of pulse 3 from pulse 2 is T , and the envelope function of these pulses are the same, $\tilde{E}(t)$. Picking out terms which satisfy the momentum requirement $k_4 (= k_3 + k_2 - k_1)$ in Eq. (3-6), we find that six terms contribute. By using the rotating-wave approximation, four terms remain:

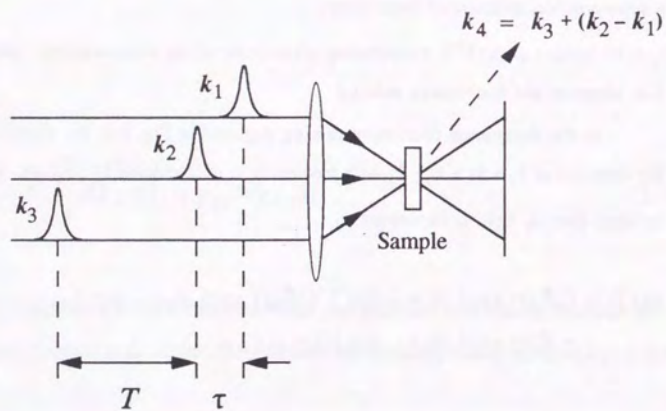


Figure 3-1 Schematic of degenerate-four-wave mixing for T_1 and T_2 measurements

$$\rho_{21}^{(3)}(r, t; \tau, T; k_4, \omega) \propto \left(\frac{i}{\hbar} \mu\right)^3 \int_{-\infty}^t dt_3 \int_{-\infty}^{t_3} dt_2 \int_{-\infty}^{t_2} dt_1 \exp[ik_4 r - i\omega t]$$

$$\times \left[\exp[-(\gamma + i\Delta\omega)(t - t_3) - \Gamma(t_3 - t_2) - (\gamma - i\Delta\omega)(t_2 - t_1)] \right.$$

$$\times \{ \tilde{E}(t_3 - T) \tilde{E}(t_2) \tilde{E}^*(t_1 + \tau) + \tilde{E}(t_3) \tilde{E}(t_2 - T) \tilde{E}^*(t_1 + \tau) \}$$

$$+ \exp[-(\gamma + i\Delta\omega)(t - t_3) - \Gamma(t_3 - t_2) - (\gamma + i\Delta\omega)(t_2 - t_1)]$$

$$\times \{ \tilde{E}(t_3 - T) \tilde{E}^*(t_2 + \tau) \tilde{E}(t_1) + \tilde{E}(t_3) \tilde{E}^*(t_2 + \tau) \tilde{E}(t_1 - T) \} \left. \right], \quad (3-11)$$

where $\Delta\omega = \Omega - \omega$ is the detuning of incident laser frequency from the transition frequency of the two-level system. The corresponding polarization $P^{(3)}(r, t; \tau, T; k_4, \omega)$ can be calculated by using Eq. (3-7), and the light intensity as a function of the delays τ and T is given by

$$I_4(\tau, T) \propto \int_{-\infty}^{\infty} dt | P^{(3)}(r, t; \tau, T; k_4, \omega) |^2. \quad (3-12)$$

This time-delay dependence of the intensity of the fourth beam is the signal trace in degenerate four-wave mixing experiments.

As a simple but essential example, we consider δ -function incident pulses. In this case, when $T, \tau > 0$,

$$P^{(3)}(r, t; \tau, T; k_4, \omega) \propto \int_0^{\infty} d\Omega g(\Omega) \exp[-\Gamma T - \gamma(t - T + \tau)]$$

$$\times \exp[-i\Delta\omega(t - T - \tau)] \theta(t - T), \quad (3-13)$$

where $\theta(t)$ is the Heaviside function, which is unity for $t \geq 0$ and zero for $t < 0$. If we assume a Gaussian distribution of the transition frequency centered at Ω_0 with a width of $\Delta\Omega$, *i.e.*,

$$g(\Omega) = \frac{1}{\sqrt{\pi} \Delta\Omega} \exp\left[-\left(\frac{\Omega - \Omega_0}{\Delta\Omega}\right)^2\right], \quad (3-14)$$

the time-delay dependence of the signal intensity I_4 is obtained by using Eqs. (3-12)-(3-14) as follows:

$$I_4(\tau, T) \propto \exp[-2\Gamma T] \exp[-4\gamma\tau] \operatorname{erfc}\left[-\frac{\Delta\Omega}{\sqrt{2}}\left(\tau - \frac{2\gamma}{(\Delta\Omega)^2}\right)\right], \quad (3-15)$$

where erfc is the complementary error function:

$$\operatorname{erfc}[x] = \int_x^\infty du \exp[-u^2]. \quad (3-16)$$

When the transition spectrum of the system has an extremely large inhomogeneous broadening, *i.e.*, $\Delta\Omega \rightarrow \infty$, Eq. (3-15) is reduced to

$$I_4(\tau, T) \propto \exp[-2\Gamma T] \exp[-4\gamma\tau]. \quad (3-17)$$

For another extreme, when the transition of the system has no inhomogeneous broadening, *i.e.*, $\Delta\Omega \rightarrow 0$, Eq. (3-15) yields

$$I_4(\tau, T) \propto \exp[-2\Gamma T] \exp[-2\gamma\tau]. \quad (3-18)$$

Thus, we can obtain the energy relaxation time $T_1 (= \Gamma^{-1})$ and the phase relaxation time $T_2 (= \gamma^{-1})$ by varying the delay T of the pulse 3 and the delay τ of the pulse 1, respectively.

The detailed theoretical treatment of T_2 measurements was discussed in the previous studies [107,108]. Here, we discuss T_1 measurements. For simplicity, it is assumed that the phase relaxation time T_2 is much shorter than the pulse duration. By using Eqs. (3-11) and (3-7), we find that

$$P^{(3)}(r, t; \tau, T; k_4, \omega) \propto \int_{-\infty}^t dt' \exp[-\Gamma(t-t')] \times [\tilde{E}(t-T) \tilde{E}(t') \tilde{E}^*(t'+\tau) + \tilde{E}(t) \tilde{E}(t'-T) \tilde{E}^*(t'+\tau)], \quad (3-19)$$

for both homogeneous and inhomogeneous broadening cases. In T_1 measurements delay τ is fixed and T is varied. The observed light intensity I_4 is expressed as a function of delay T by using Eq. (3-12):

$$I_4(T) \propto D(T) + C_1(T) + C_2(T) + C_3(T), \quad (3-20)$$

where

$$D(T) = \int_{-\infty}^{\infty} dt |\tilde{E}(t-T)|^2 |G_r(t, \tau)|^2, \quad (3-21a)$$

$$C_1(T) = \int_{-\infty}^{\infty} dt \tilde{E}(t-T) \tilde{E}^*(t) G_r(t, \tau) G_r^*(t-T, \tau+T), \quad (3-21b)$$

$$C_2(T) = C_1^*(T) , \quad (3-21c)$$

and

$$C_3(T) = \int_{-\infty}^{\infty} dt | \tilde{E}(t) |^2 | G_r(t - T, \tau + T) |^2 . \quad (3-21d)$$

Here G_r is the following function:

$$G_r(t + x_1, x_2 - x_1) = \int_0^{\infty} du \exp[- \Gamma u] \tilde{E}(t - u + x_1) \tilde{E}^*(t - u + x_2) . \quad (3-22)$$

The first term, $D(T)$, in the r.h.s. of Eq. (3-20) represents the decay profile determined by Γ , while the last three terms $C_i(T)$ ($i = 1, 2$, and 3) have finite values only when the three incident pulses overlap temporally and do not give information of T_1 , *i.e.*, they represent coherent artifacts. The magnitude of the coherent artifacts is sensitive to the delay τ , which is usually fixed near zero. Small positive shift of τ increases the artifacts, while its negative shift decreases the artifacts. The reason of this behavior is explained as follows. The term $D(T)$, whose decay represents T_1 , arises from the process where pulses 1 and 2 form a grating and pulse 3 is diffracted by it, while the terms of coherent artifacts arise in the case where pulses 1 and 3 form a grating and pulse 2 is diffracted. In the former process, since the grating amplitude is the same for positive delay τ and negative delay $-\tau$, the signal intensity $D(T, \tau) = D(T, -\tau)$. On the other hand, in the latter process, the area of pulse 2 arriving after pulse 1 is larger, so

that the diffraction intensity I_4 is higher, at positive delay τ than at negative delay $-\tau$, when pulse 3 overlaps with pulse 1, *i.e.*, $T \sim -\tau$. We should be careful about the contribution of such coherent artifacts in the discussion of the behavior around zero delay.

Although three incident pulses were assumed in the above discussion, the other DFWM processes can be treated in the same way. For example, two-pulse self-diffraction is a process, where $k_3 = k_2$ and $T = 0$.

It has been shown that ultrashort T_1 or T_2 measurements with the above techniques can be performed by using not only short pulses but also temporally incoherent light because these measurements are based on nonlinear optical phenomena [109-113].

3.3. Pump-probe spectroscopy

In pump-probe spectroscopy, we measure the intensity change of probe, which has wave vector k_p and frequency ω_p , transmitted through a sample material perturbed by excitation pulses, which have wave vector k_L and frequency ω_L and precede the probe by delay τ . This process is also described as a third-order nonlinear optical response under weak excitation condition. The total electric field is expressed as

$$E(r, t) = \{ \tilde{E}_L(t + \tau) \exp[- i\omega_L \tau] \exp[ik_L r - i\omega_L t] + \tilde{E}_p(t) \exp[ik_p r - i\omega_p t] \} + \text{c.c.} , \quad (3-23)$$

where $\tilde{E}_L(t)$ and $\tilde{E}_p(t)$ are envelope functions of pump and probe pulses, respectively, peaked at $t = 0$. By substituting this expression for $E(r, t)$ in Eq. (3-6), we find that six terms have wave vector k_p and contribute to $\rho_{21}^{(3)}(t, k_p)$. By using the rotating-

wave approximation, $\rho_{21}^{(3)}(t, k_p)$ is reduced to the sum of the following three components of different physical origin:

$$\rho_{21}^{(3)}(t, k_p) = \rho_{21}^{(3)}(t, k_p)_{[\text{INC}]} + \rho_{21}^{(3)}(t, k_p)_{[\text{PPC}]} + \rho_{21}^{(3)}(t, k_p)_{[\text{FID}]} \quad (3-24)$$

where

$$\begin{aligned} \rho_{21}^{(3)}(t, k_p)_{[\text{INC}]} = & 2 \rho_D^{(0)} \left(\frac{i}{\hbar} \mu \right)^3 \int_{-\infty}^t dt_3 \int_{-\infty}^{t_3} dt_2 \int_{-\infty}^{t_2} dt_1 \exp[ik_p r - i\omega_p t] \\ & \times \exp[- \{ \gamma + i(\Omega - \omega_p) \} (t - t_3) - \Gamma (t_3 - t_2)] \\ & \times [\exp[- \{ \gamma - i(\Omega - \omega_L) \} (t_2 - t_1)] \tilde{E}_p(t_3) \tilde{E}_L(t_2 + \tau) \tilde{E}_L^*(t_1 + \tau) \\ & + \exp[- \{ \gamma + i(\Omega - \omega_L) \} (t_2 - t_1)] \tilde{E}_p(t_3) \tilde{E}_L^*(t_2 + \tau) \tilde{E}_L(t_1 + \tau)], \end{aligned} \quad (3-25a)$$

$$\begin{aligned} \rho_{21}^{(3)}(t, k_p)_{[\text{PPC}]} = & 2 \rho_D^{(0)} \left(\frac{i}{\hbar} \mu \right)^3 \int_{-\infty}^t dt_3 \int_{-\infty}^{t_3} dt_2 \int_{-\infty}^{t_2} dt_1 \exp[ik_p r - i\omega_p t] \\ & \times \exp[- \{ \gamma + i(\Omega - \omega_p) \} (t - t_3) - \{ \Gamma + i(\omega_L - \omega_p) \} (t_3 - t_2)] \\ & \times \exp[- \{ \gamma - i(\Omega - \omega_L) \} (t_2 - t_1)] \tilde{E}_L(t_3 + \tau) \tilde{E}_p(t_2) \tilde{E}_L^*(t_1 + \tau) , \end{aligned} \quad (3-25b)$$

and

$$\begin{aligned} \rho_{21}^{(3)}(t, k_p)_{[\text{FID}]} = & 2 \rho_D^{(0)} \left(\frac{i}{\hbar} \mu \right)^3 \int_{-\infty}^t dt_3 \int_{-\infty}^{t_3} dt_2 \int_{-\infty}^{t_2} dt_1 \exp[ik_p r - i\omega_p t] \\ & \times \exp[- \{ \gamma + i(\Omega - \omega_p) \} (t - t_3) - \{ \Gamma + i(\omega_L - \omega_p) \} (t_3 - t_2)] \\ & \times \exp[- \{ \gamma + i(\Omega - \omega_p) \} (t_2 - t_1)] \tilde{E}_L(t_3 + \tau) \tilde{E}_L^*(t_2 + \tau) \tilde{E}_p(t_1) . \end{aligned} \quad (3-25c)$$

The corresponding third-order nonlinear polarizations, *i.e.*, $P^{(3)}_{[\text{INC}]}$, $P^{(3)}_{[\text{PPC}]}$, and $P^{(3)}_{[\text{FID}]}$, are calculated by Eq. (3-7). The total third-order nonlinear polarization $P^{(3)}$ is the sum of them, *i.e.*,

$$P^{(3)}(t, k_p) = P^{(3)}(t, k_p)_{[\text{INC}]} + P^{(3)}(t, k_p)_{[\text{PPC}]} + P^{(3)}(t, k_p)_{[\text{FID}]} \quad (3-26)$$

Here $P^{(3)}_{[\text{INC}]}$ corresponds to an incoherent process, where level population is changed by pump, $P^{(3)}_{[\text{PPC}]}$ a pump-polarization coupling process, where probe field interacts with pump induced polarization to create population grating, and $P^{(3)}_{[\text{FID}]}$ a perturbed free-induction decay process, where the probe-induced polarization is modified by the pump field [114]. For simplicity, we assume that probe pulses are extremely short, *i.e.*, $\tilde{E}_p(t) = \delta(t)$, and that pump pulses are rectangular with the width of $2\Delta t$, *i.e.*, $\tilde{E}_L(t) = \theta(t + \Delta t) - \theta(t - \Delta t)$. Then it is found that $P^{(3)}_{[\text{INC}]}$ is non-zero at the probe delay $\tau > -\Delta t$, $P^{(3)}_{[\text{PPC}]}$ at $|\tau| < \Delta t$, and $P^{(3)}_{[\text{FID}]}$ at $\tau < \Delta t$. That is, when the probe follows the pump, $P^{(3)}_{[\text{INC}]}$ gives the dominant contribution, and, when the probe precedes the pump, $P^{(3)}_{[\text{FID}]}$ is dominant, while, when they overlap, we observe the superposition of the three terms.

Differential transmission spectra (DTS) are the change in the transmittance spectra induced by pump pulses, *i.e.*,

$$\frac{\Delta T(\omega)}{T(\omega)} \equiv \frac{T'(\omega) - T(\omega)}{T(\omega)} \quad (3-27)$$

where $T(\omega)$ and $T'(\omega)$ are transmittance spectra unperturbed and perturbed by the pump, respectively. This spectrum is expressed in terms of nonlinear polarization as follows:

$$\frac{\Delta T(\omega)}{T(\omega)} \propto -\text{Im}\left[\frac{P^{(3)}(\omega)}{\epsilon_p(\omega)}\right], \quad (3-28)$$

where $P^{(3)}(\omega)$ is the spectral dependence of the nonlinear polarization, *i.e.*, a Fourier transformation of $P^{(3)}(t, k_p)$, and $\epsilon_p(\omega)$ is the spectral dependence of unperturbed transmitted probe field. Since this signal arises from the coupling of the nonlinear polarization with the probe field, the signal is proportional to the nonlinear polarization, which is different from the case where the light intensity is detected. Therefore, the detected signal is also the superposition of the above three processes. A significant feature of the contribution of $P^{(3)}_{\text{[PPC]}}$ and $P^{(3)}_{\text{[FID]}}$ appears as an oscillatory structure in DTS around the frequencies of pump pulse and/or sharp absorption peak. The oscillation period, corresponding to the inverse of the delay between pump and probe, is about 10 nm for 100-fs delay, while it is about 1 nm for 1-ps delay. Therefore, such phenomena are more significant in femtosecond region than in picosecond region, and have been observed for the first time with femtosecond pulses [114-121].

Although the above discussion is concerned with the imaginary part of $\chi^{(3)}$, the effect of the real part of $\chi^{(3)}$ can be discussed in the same way, which gives rise to, *e.g.*, induced phase modulation of probe field by an intense pump pulse [48,105] described in Subsection 4.5.5.

In the above two-level model, bleaching of the absorption from the ground to the excited state in resonance with the incident pump pulses was discussed. However, induced excited-state absorption is also observed in this type of pump-probe experiment. In order to discuss this phenomenon, it is necessary to consider a three-level system, which has the ground state $|1\rangle$, the first excited state $|2\rangle$, and

the second excited state $|3\rangle$. The induced excited-state absorption from $|2\rangle$ to $|3\rangle$ arises from the third-order nonlinear polarization caused by the density matrix element $\rho_{32}^{(3)}$. The three-level density matrix can be treated in the similar way by Eq. (3-1). Then, it is found that $\rho_{32}^{(3)}$ arises through the perturbation processes $\rho_{11}^{(0)} \rightarrow \rho_{21}^{(1)} \rightarrow \rho_{22}^{(2)} \rightarrow \rho_{32}^{(3)}$, when the pump is resonant with the transition between $|1\rangle$ and $|2\rangle$. Therefore, the level population of the first excited state can be probed by detecting the induced excited-state absorption caused by $\rho_{32}^{(3)}$.

CHAPTER 4

EXCITED-STATE DYNAMICS IN VANADYL PHTHALOCYANINES

4.1. Introduction

The development of practical optical devices, which employ optical nonlinearities of the constituent materials for the control of light, is a research of great interest. There are several requirements for materials in such applications: high nonlinear optical susceptibility, fast response, processibility, and thermal and chemical stability. Of the candidates for materials for such purposes, organic materials have superior flexibility in processing and manipulation. And, particularly, conjugated π -electron systems have long been known to possess large optical nonlinearities and ultrafast optical responses [3]. These attractive properties are due to the π -electron delocalization extending in one dimension, as in polymers, or in two dimension, as in macrocyclic molecules. Among such materials, intense interest has recently centered on conjugated macrocyclic compounds possessing a ring π -electron conjugation, especially phthalocyanines (tetraazatetrabenzporphyrins), of which nonlinear optical properties have been investigated extensively [122-131].

A distinct property of phthalocyanines is their extremely strong absorption in the wavelength range between 600 and 700 nm (Q band), in which the molar extinction coefficient exceeds 10^5 l/mol-cm. This absorption band arises predominantly from an $a_{1u}(\pi) - e_g(\pi^*)$ molecular orbital transition. Phthalocyanines have a molecular structure similar to that of porphyrins, some of which are contained in biological systems such as chlorophylls (photosynthetic materials) and heme proteins. However, porphyrins have a much weaker Q-band transition because the first and the second highest-occupied molecular orbitals (HOMO), *i.e.*, $a_{2u}(\pi)$ and $a_{1u}(\pi)$, lie close in energy and have an extensive configuration interaction, which results in a reduced

oscillator strength of the Q band. This difference in the excited electronic states of phthalocyanines and porphyrins is due to either the aza-bridges or the benzo groups contained in a phthalocyanine ring, which lift the accidental degeneracy of $a_{1u}(\pi)$ and $a_{2u}(\pi)$ orbitals [132,133]. Because of their strong Q band, phthalocyanines exhibit fairly high efficiencies in various optoelectronic responses such as photosensitizing, photoconducting, and xerographic properties.

In phthalocyanine molecules, it is known that various kinds of metals can coordinate to the center of their large aromatic ring and markedly change the properties of the molecule [132]. The nonlinear optical susceptibilities of third-harmonic generation (THG) in films of several metallophthalocyanines (VO, Sn, Co, and Ni) and metal-free (H_2) phthalocyanine have been examined [123]. Among these phthalocyanines, vanadyl phthalocyanine showed the largest value of $\chi^{(3)}$, which is in the same order of magnitude of those of conjugated polymers such as polydiacetylenes. For this reason intense interest is focused on this compound, vanadyl phthalocyanine.

In their condensed phases, phthalocyanines can exist in several morphological forms with different stacking arrangements of the disk-like molecules [132]. Such a structural variation also causes modifications in their properties. Vanadyl phthalocyanine, investigated in the present study, has been known to exist in three phases, phases I, II, and III, which were characterized by differential scanning calorimetry, X-ray diffraction, and optical absorption spectroscopy [134,135]. Its crystal in phase II has been found to have a triclinic crystal structure, a slipped-stacked form. For phases I and III, their crystal structures have not been determined yet because of a lack of suitable single crystals. However, a cofacially-stacked form has been inferred for phase I from its absorption spectrum. Various properties of these phases have been studied extensively. Electronic properties were studied by

optical absorption and luminescence spectroscopies [136] and electroabsorption spectroscopy [137,138]. Studies of photoconductivity have reported higher efficiency of photogeneration in phase II than in phase I [139]. The structures of these polymorphs have also been studied by scanning electron microscopy (SEM) and infrared and Raman spectroscopies [140]. Recently the third-order nonlinear optical susceptibilities $\chi^{(3)}$ of these polymorphs have been evaluated by third-harmonic-generation measurements and greater values of $\chi^{(3)}$ were found in phase II than in phase I at fundamental wavelengths of 1.9 and 1.5 μm [129,130]. Thus, several differences between these phases have been observed.

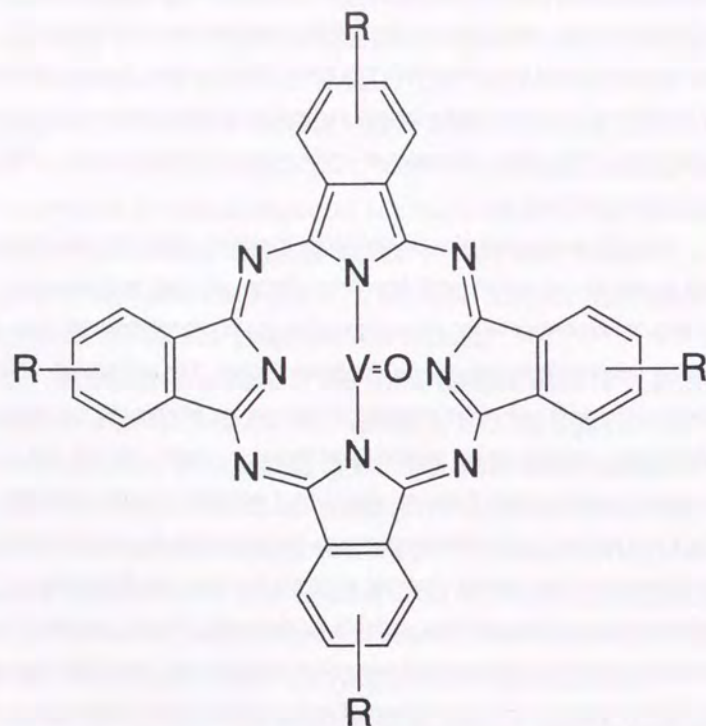
Now relaxation processes of their excited electronic states, *i.e.*, dynamical properties of excitons created in these materials by short light pulses, are the interesting topics to be investigated. A few groups have reported femtosecond studies on several phthalocyanines. Greene and Millard showed that the initial exciton decay can be interpreted in terms of a $(t^{-1/2})$ time-dependent singlet exciton-exciton annihilation rate in a polycrystalline sample of β -hydrogen phthalocyanine (H_2Pc) by observing temporal response of induced excited-state absorption [141]. Ho and Peyghambarian studied a polycrystalline film of fluoro-aluminium phthalocyanine (AlPc-F) and explained the decay kinetics of bleaching due to excitons by a model including constant rates of exciton-exciton annihilation and exciton-phonon coupling [142]. Casstevens *et al.* also observed excitation-intensity-dependent decay of degenerate four-wave mixing (DFWM) signals from evaporated films of H_2Pc and Langmuir-Blodgett (LB) films of silicon phthalocyanine (SiPc) [143]. DFWM measurements on SiPc derivatives in several molecular environments in LB and polymer-doped films were reported by Neher *et al.* [144], in which differences in the transient response were observed and an explanation in terms of the strength of the electronic coupling between phthalocyanine rings was proposed. More recently

Williams *et al.* studied polarization dependence of spectral hole burning and observed rapid intraband decay, taking place within 200 fs, of excitons created in the lowest-energy absorption band in a AlPc-F thin film [145]. These studies, however, have not fully clarified the relaxation mechanisms of excitons yet and also systematic studies of the dependence of the exciton dynamics on central metals and morphological forms have not been performed yet.

From the above points of view, since investigation of morphology dependence should precede that of central metal dependence, the present study was focused on the effects of morphology on the relaxation mechanisms of excited electronic states in one of the metallophthalocyanines, vanadyl phthalocyanine. For this purpose, time-resolved studies were carried out by means of femtosecond pump-probe spectroscopy on the phthalocyanine in various morphological forms, *i.e.*, phase I, phase II, and a novel phase prepared as thin films, and also isolated molecular systems in solution and in a host polymer. In the following sections, the preparation of such polymorphs and the features of their excited electronic states are described, and differences in transient optical responses of these materials are discussed. Finally, as general phenomena appearing in femtosecond pump-probe measurements, novel behaviors of time-resolved transmission spectra observed around the excitation wavelength on a femtosecond time scale are also discussed.

4.2. Sample preparation

For the present study, both unsubstituted vanadyl phthalocyanine (VOPc) [129,130] and tertiary-butyl substituted vanadyl phthalocyanine ($(t\text{-Bu})_n\text{VOPc}$) [129,131,139,146] were prepared. The molecular structure is shown in Fig. 4-1. The *t*-butyl substitution makes this compound soluble in several organic solvents such as chloroform, which is a great advantage in processing the compound. Several types of



R = H or *t*-butyl (C(CH₃)₃)

Figure 4-1 Molecular structure of vanadyl phthalocyanine

samples were studied as listed in Table 4-1. Isolated molecular phases were prepared in a solvent and in a host polymer, polystyrene, containing the molecule at low concentration. Aggregated systems were prepared as thin films. Three kinds of such films were made on quartz substrates: a spin-coated film of (*t*-Bu)_nVOPc doped in polystyrene, a similar film without the host polymer, and a vapor-deposited film of VOPc. A vapor-deposited film of VOPc on an alkali halide crystal, KBr, prepared by the molecular-beam-epitaxy technique [147] was also studied.

(*t*-Bu)_nVOPc was synthesized from a mixture of 4-*t*-butylphthalonitrile, phthalonitrile, and vanadium trichloride by heating at 250°C. The obtained product was purified by column chromatography on silica gel by using chloroform as an eluent, followed by precipitation from chloroform to methanol. The average number of substituted *t*-butyl groups was 1.1 in the present study. Field deposition mass spectroscopy showed that the product was a mixture of mono- and di-substituted derivatives.

A solution sample of (*t*-Bu)_{1.1}VOPc in chloroform was prepared in a 1-mm-pathlength cuvette. The concentration was about 8×10^{-5} mol/l, which corresponds to the mean intermolecular distance of 280 Å. Since the size of the molecule is *ca.* 14 Å in diameter, interaction between molecules must be very weak in this solution, *i.e.*, a monomeric phase. Its absorption spectrum is shown in Fig. 4-2, which has a sharp peak at *ca.* 700 nm. Similar molecular environment could be prepared also in solid state by casting chloroform solution of (*t*-Bu)_{1.1}VOPc mixed with polystyrene at relatively low concentration, 0.01 wt%, on quartz substrates. This concentration corresponds to 1.6×10^{-4} mol/l, or one molecule in (220 Å)³. This dilute film showed an absorption spectrum similar to that of the solution.

Thin films were cast on quartz substrates by spin-coating the compound dissolved in chloroform either with or without polystyrene. The reason for the choice

- Solution
 $(t\text{-Bu})_{1,1}\text{VOPc} / \text{CHCl}_3$
- Casting
 $(t\text{-Bu})_{1,1}\text{VOPc} / \text{PS} \quad 0.01 \text{ wt}\%$
- Spin Coating (on quartz)

{	$(t\text{-Bu})_{1,1}\text{VOPc} / \text{PS} \quad 10 \text{ wt}\%$	Phase I
{	$(t\text{-Bu})_{1,1}\text{VOPc} / \text{PS} \quad 10 \text{ wt}\%$	Phase II
{	$(t\text{-Bu})_{1,1}\text{VOPc}$	Phase I
{	$(t\text{-Bu})_{1,1}\text{VOPc}$	Phase II
- Vapor Deposition (on quartz)

{	VOPc	Phase I
{	VOPc	Phase II
- Vapor Deposition (on KBr)
 VOPc

PS : Polystyrene

Table 4-1 List of samples

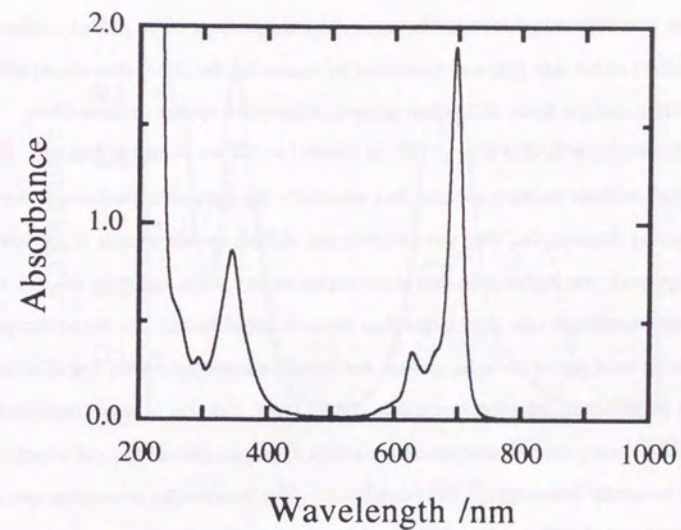


Figure 4-2 Absorption spectrum of chloroform solution of $(t\text{-Bu})_{1,1}\text{VOPc}$

of polystyrene as a host polymer is that this polymer provided the best stability of samples against intense laser-pulse irradiation among several typical polymers such as polymethyl methacrylate, polycarbonate, polyvinyl acetate, and so forth. Thickness of the films with and without host polymer were measured to be *ca.* 0.5 μm and *ca.* 0.1 μm , respectively. These films prepared by the above procedure had phase I structure and were changed into phase II structure by exposure to dichloroethane vapor in a desiccator for *ca.* 20 hours at room temperature. The phase I-to-phase II transition of the thin film was monitored by measuring the UV-visible absorption spectrum and the X-ray diffraction pattern. Absorption spectra of these films containing 10 wt% of $(t\text{-Bu})_{1,1}\text{VOPc}$ in phases I and II are shown in Fig. 4-3. Those of films without the host polymer had essentially the same structures except for the following features, *i.e.*, they were slightly red-shifted; the absorbance at the lower energy peak was higher than that at the higher energy peak; and also, the tails at the longer wavelength side were larger than those of doped films. The absorption peaks in the Q band region are split, shifted, and broadened compared with that of solution. This suggests that in rather dense spin-coated films, and also in vapor deposited films described later, the phthalocyanine molecules aggregate and there exist strong intermolecular interactions. The marked difference between the absorption spectra of phases I and II is the peak at 810 nm after solvent vapor treatment, which is due to differences in the molecular arrangements between the two phases.

VOPc was purchased from Eastman-Kodak and purified by sublimation at 440°C under a 10^{-6} Torr vacuum. Because VOPc is not soluble, thin films were formed by vacuum deposition onto quartz substrates. Thickness of the films were measured to be *ca.* 0.1 μm . Samples obtained in this manner had phase I structure which could be changed to phase II stacking structure by heating them at 125°C under atmospheric pressure. The thermally induced structural change was monitored in the same way as

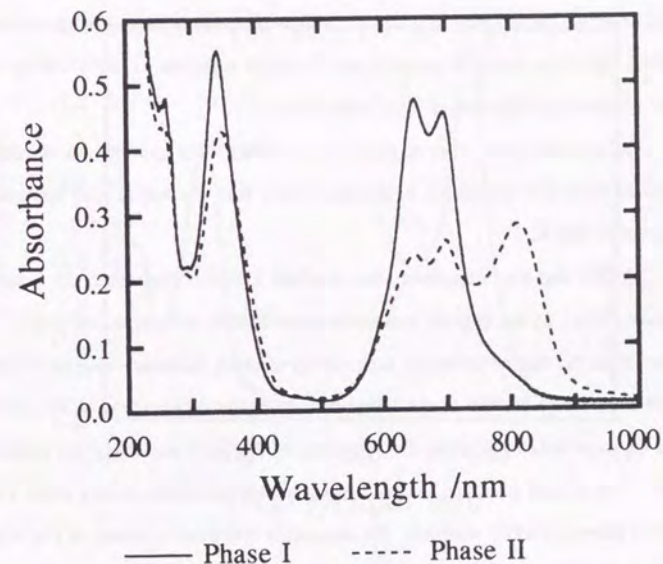


Figure 4-3 Absorption spectra of $(t\text{-Bu})_{1,1}\text{VOPc}$ doped in polystyrene at 10 wt%

described above. The changes in the absorption spectra were similar to those obtained in spin-coated films of $(t\text{-Bu})_{1,1}\text{VOPc}$ without host polymer, except that absorption peaks were slightly red-shifted both in phase I and in phase II.

Similarity in the absorption spectra of VOPc and $(t\text{-Bu})_{1,1}\text{VOPc}$ suggests that the *t*-butyl substituent does not affect much the structure of the molecular aggregates. However, the one with four substituents, $(t\text{-Bu})_4\text{VOPc}$, existed only in phase I and could never be transformed to phase II. This is probably because the molecular packing density is higher in phase II and the phase transition is prevented by the steric hindrance in the case of tetra substitution.

X-ray diffraction measurements showed that these spin-coated or vapor-deposited films are amorphous in structure rather than crystalline with domain sizes of the order of 100 Å.

VOPc was also deposited onto an alkali halide crystal substrate, potassium-bromide (KBr), by the organic molecular-beam-epitaxy technique [147-152]. It is known from the data of reflection high-energy electron diffraction (RHEED) that, in layers close to the surface of the KBr substrate, epitaxially stacked VOPc molecules form a square lattice reflecting the symmetry of the (001) surface of the substrate [147]. This crystal structure has not been observed previously in any other VOPc crystals grown by other methods. Its absorption spectrum is shown in Fig. 4-4. Because the film used for measurements had thickness corresponding to several tens of layers, it is not certain whether the whole film has the same crystal structure.

4.3. Excited electronic states

Figure 4-5 shows a schematic of the energy level diagram of the phthalocyanine ligand. The notation of the states adopted in Ref. [153] was used. The lowest allowed optical transition at 600 - 700 nm wavelength region, Q band,

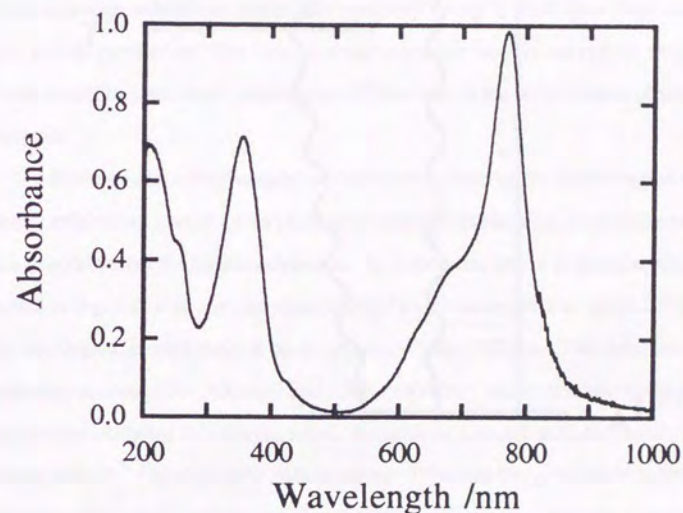
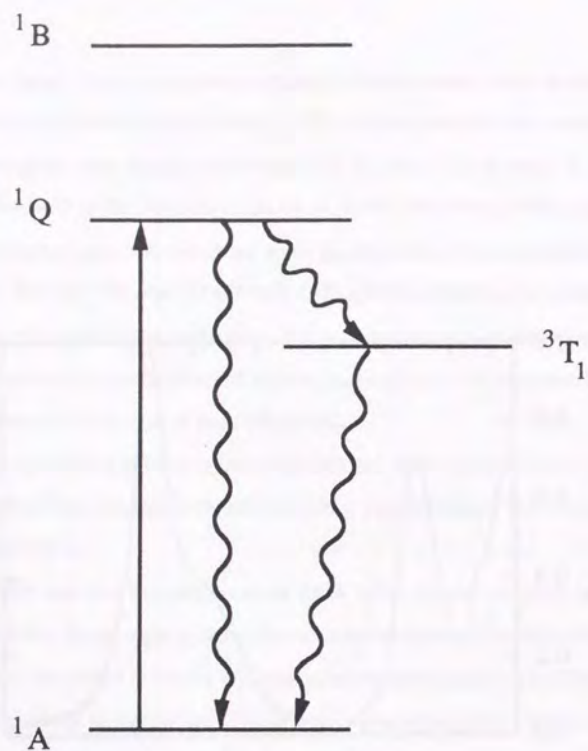


Figure 4-4 Absorption spectrum of VOPc deposited on KBr



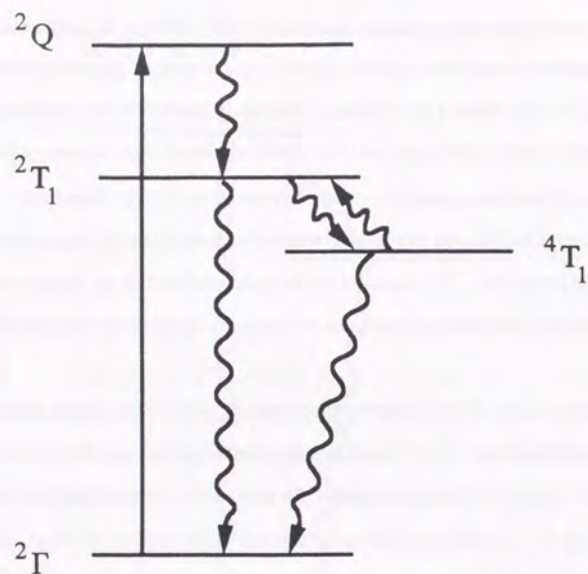
- 1A : Ground singlet state
 1Q : First excited singlet state (Q band)
 1B : Second excited singlet state (B band)
 3T_1 : Triplet state

Figure 4-5 Energy level diagram of phthalocyanine ligand

arises from a doubly degenerate transition $a_{1u}(\pi) \rightarrow e_g(\pi^*)$ of the phthalocyanine ring. The next lowest energy absorption band at 300 - 400 nm, B band, arises from a doubly degenerate transition $a_{2u}(\pi) \rightarrow e_g(\pi^*)$. In the case of phthalocyanines the orbital a_{1u} lies well above the orbital a_{2u} , whereas in porphyrins the orbital a_{2u} , which gives rise to Q band in this case, and the orbital a_{1u} lie so close in energy that extensive configuration interaction occurs between them [132]. Therefore, phthalocyanines exhibit red shifted and relatively strong Q-band absorption compared with normal porphyrins. This isolated single electronic band in red region, which has a molar extinction coefficient greater than 10^5 l/mol-cm, is the novel feature of this molecule.

Excited states of the vanadyl phthalocyanine lying in the visible region are mostly originating from $\pi - \pi^*$ transitions of phthalocyanine ring, as described above as a general property of phthalocyanines. In monomers, whose absorption spectrum is shown in Fig. 4-2, a strong and sharp Q-band transition appears at about 700 nm and the next higher excited state, B band, appears at about 350 nm. The shoulders appearing at about $700 - 800$ cm^{-1} and $1500 - 1600$ cm^{-1} higher than the sharp peak of Q band are attributed to vibronic states. Because, in vanadyl phthalocyanine, the diamagnetic Pc^{2-} ligand couples with an unpaired electron in d_{xy} orbital of a central metal ion VO^{2+} , it is a paramagnetic molecule. Because of this electron coupling, singlet states of Pc^{2-} become singdoublet and triplet states become tripdoublet and tripplet in the molecule [153]. These multiplets have Kramers degeneracy [136]. The energy level diagram of VOPc monomer is shown in Fig. 4-6.

In solid states, transitions of the monomer shift and split because of the intermolecular interaction in molecular aggregates. In phase I there appear two peaks in the Q-band region, as shown in Fig. 4-3. The slight blue shift of the absorption can be explained by the cofacially and collinearly associated dimer formation

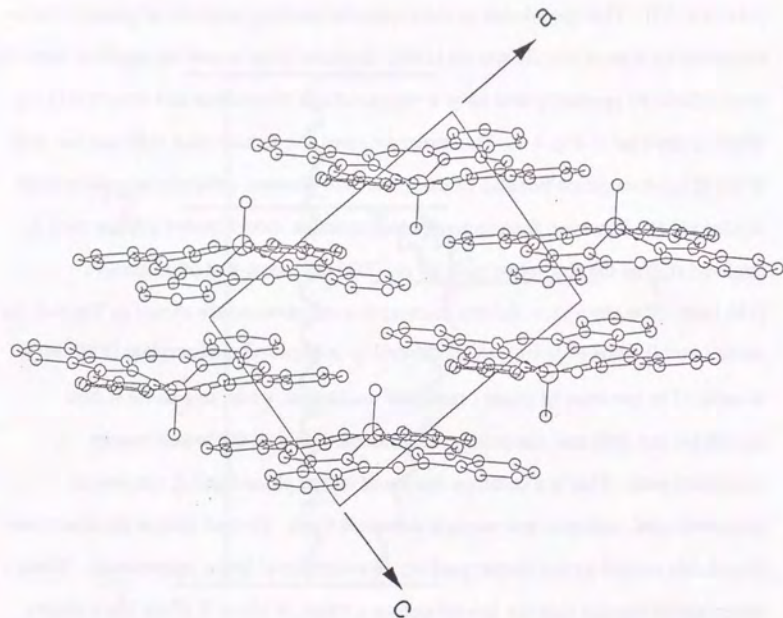


- 2Γ : Ground singdoublet state
 $2Q$: Excited singdoublet state (Q band)
 $2T_1$: Tripdoublet state
 $4T_1$: Tripquartet state

Figure 4-6 Energy level diagram of paramagnetic phthalocyanine with an unpaired electron

[134,154,155]. This speculation of the molecular stacking structure of phase I is also supported by Raman and IR spectra [140]. In phase II the crystal structure is found to have triclinic $P\bar{1}$ symmetry and have a staggered and slipped stacked structure [135], which is depicted in Fig. 4-7. This structure gives rise to both blue shift and red shift of the Q band transition because of the interaction between obliquely aligned exciton dipoles [154]. However, the dipole-dipole interaction model cannot explain such a large red shift of the absorption peak by *ca.* 2000 cm^{-1} from that of monomers [134,140]. The absorption spectra taken at low temperature are shown in Fig. 4-8 for phase I and II films of $(t\text{-Bu})_{1,1}\text{VOPc}$ doped in polymethyl methacrylate (PMMA) at 40 wt%. The spectrum of phase I remained unchanged, while, in a phase II film, significant red shift and sharpening was observed only at the lowest-energy absorption peak. This is a common feature of all the phase I and II samples of polymer-doped, undoped, and vacuum deposited films. The red shift of the absorption is probably caused by the denser packing of molecules at lower temperature. These observations suggest that the lowest-energy exciton in phase II films has a nature different from other excitons and is strongly affected by intermolecular interaction.

In tin (SnPc) and lead (PbPc) phthalocyanines, appearance of intermolecular charge-transfer transitions in the wavelength region 800 - 900 nm has been pointed out [156,157]. These two molecules possess C_{4v} symmetry as VOPc. Inferring from the similarity in the molecular symmetry, it might be possible that this charge-transfer nature is also the case for VOPc. And also, electroabsorption [137,138] and photoconductivity [139] measurements have reported the intermolecular charge-transfer nature of excitons in phase II VOPc. On the other hand, however, charge-transfer excitons were predicted to appear at energy higher than Frenkel excitons and were observed in several phthalocyanines [158,159]. The origin of the lowest energy exciton in phase II VOPc has not been well understood yet.



Space group : $P\bar{1}$

$a = 12.027 \text{ \AA}$, $b = 12.571 \text{ \AA}$, $c = 8.690 \text{ \AA}$

$\alpha = 96.04^\circ$, $\beta = 94.80^\circ$, $\gamma = 68.20^\circ$

Figure 4-7 Crystal structure of VOPc in phase II

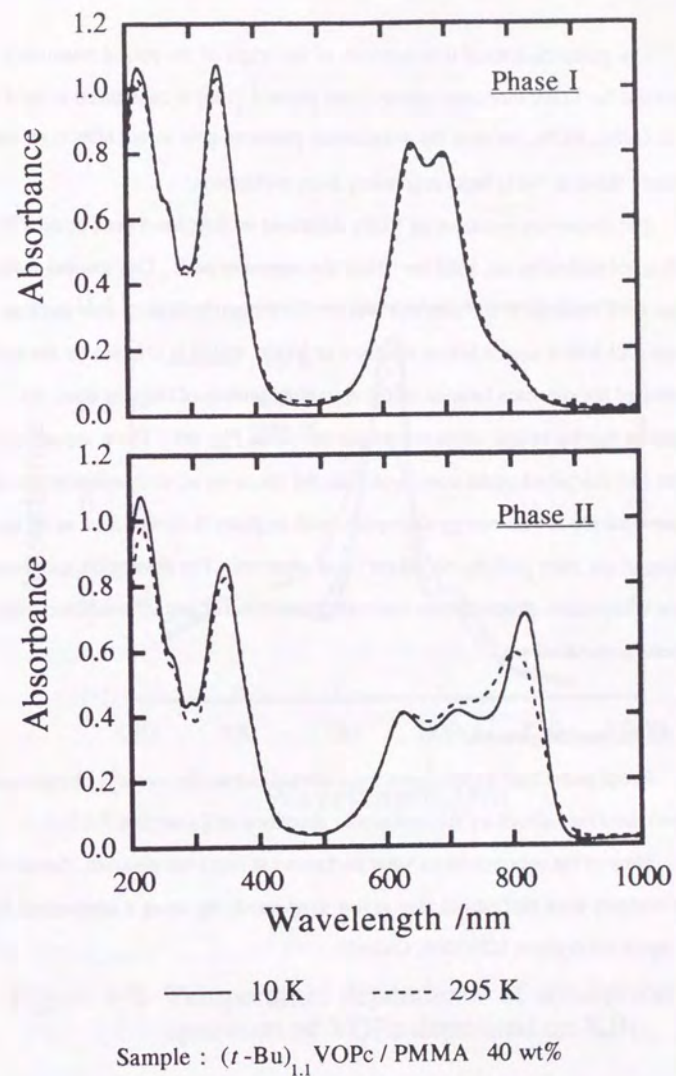


Figure 4-8 Temperature dependence of absorption spectra of $(t\text{-Bu})_{1,1}\text{VOPc}$ in phases I and II

The group theoretical interpretation of the origin of the optical transitions carried out for VOPc monomer, phase I, and phase II [136] is considered to hold valid also in (*t*-Bu)_nVOPc, because the substitution produces only minor effects on their electronic states in the Q band originating from π electrons.

The absorption spectrum of VOPc deposited on KBr has a peak at *ca.* 770 nm, which is red shifted by *ca.* 1300 cm⁻¹ from the monomer peak. This spectral feature has not been reported in the previous works. This might indicate a new stacking arrangement with a square lattice structure of VOPc, which is affected by the surface structure of the substrate because of the epitaxital growth of the thin film. Its absorption spectra at low temperatures are shown in Fig. 4-9. There appear red shifted and sharpened peaks compared with the spectrum at room temperature, as also seen for the lowest-energy absorption peak in phase II films. And, at 10 K, the splitting of the main peak by *ca.* 60 cm⁻¹ was observed. The absorption spectrum has a more complicated structure than those of phases I and II and its electronic origin has not been understood yet.

4.4. Experimental procedure

Pump-probe type experiments were carried out on the vanadyl phthalocyanine samples described above by the techniques described in Subsection 2.6.2.

Most of the measurements were performed at room temperature. Some of the measurements were carried out also at low temperature by using a continuous-flow type liquid He cryostat (CF-1204, Oxford).

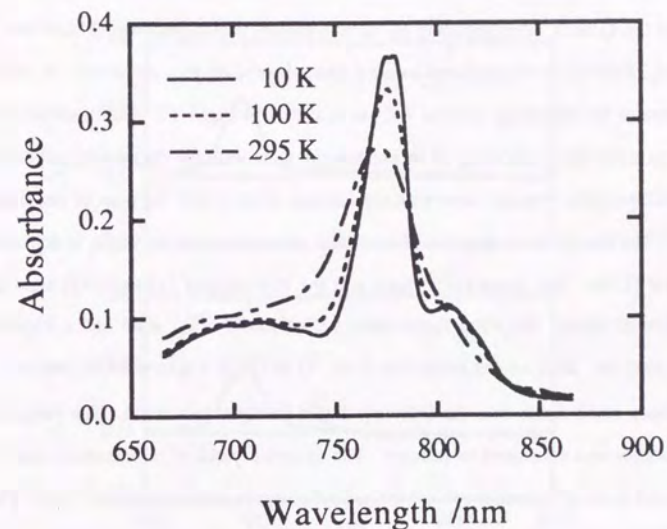


Figure 4-9 Temperature dependence of absorption spectrum of VOPc deposited on KBr

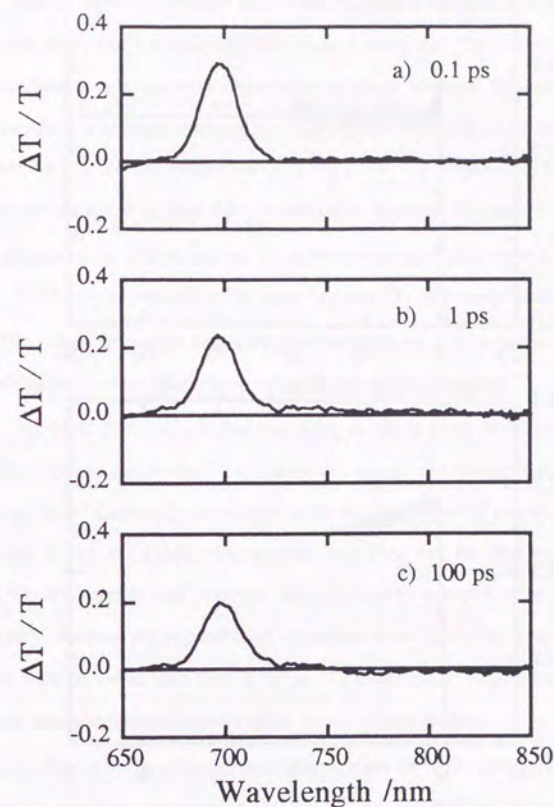
4.5. Results and discussion

4.5.1. Isolated molecular phase

Differential transmission spectra (DTS) of chloroform solution of $(t\text{-Bu})_{1,1}\text{VOPc}$ are shown in Fig. 4-10. The excitation wavelength, 620 nm, lies in the tail of the higher energy side of the Q band absorption. Significant bleaching, *i.e.*, absorption saturation, was observed at the Q band transition. At the higher energy side of the Q band, corresponding to the transparent region between Q band and B band, relatively weak induced excited-state absorption was observed. A transient response of the bleaching peak at 700 nm is shown in Fig. 4-11. This trace could be fitted to a function consisting of an exponential term with the decay-time constant of 0.7 ± 0.2 ps and a constant term with the fraction of *ca.* 0.8 of the peak of the signal.

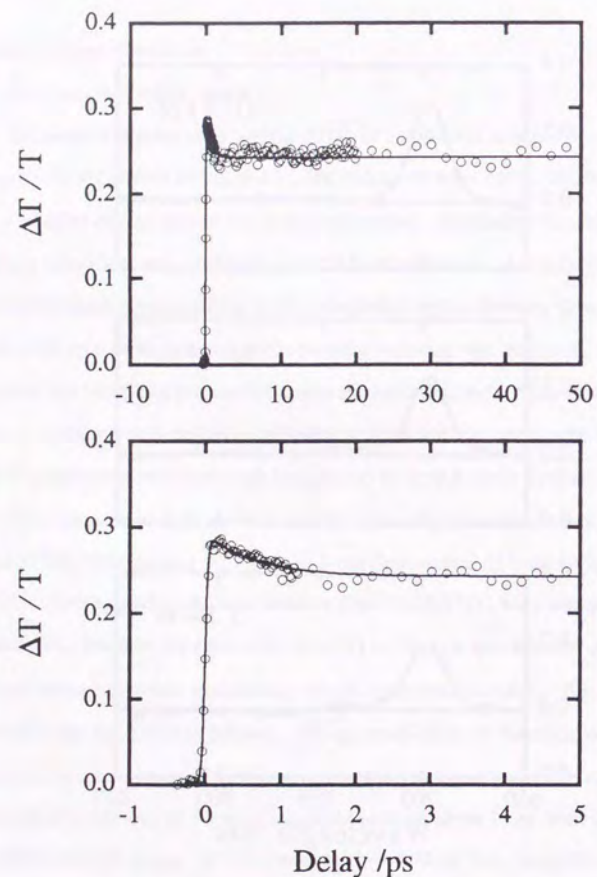
The energy-level diagram of a vanadyl phthalocyanine molecule is depicted in Fig. 4-6 [136]. The ground (${}^2\Gamma$) state and the first-excited Q-band (${}^2\text{Q}$) state are singdoublet states. Between these states a tripdouplet (${}^2\text{T}_1$) state and a triquartet (${}^4\text{T}_1$) state lie. Because the relaxation from ${}^2\text{Q}$ to ${}^2\text{T}_1$ is a spin allowed process, it can take place much faster than the ordinary singlet to triplet relaxation. The decay rate of this process was estimated as follows. The quantum yield of fluorescence was measured to be of the order of 10^{-6} in vanadyl phthalocyanine molecule [136]. The natural radiative lifetime of ${}^2\text{Q}$ state is calculated to be about 15 ns from the absorption spectrum ($\epsilon_{\text{max}} \sim 2 \times 10^5 \text{ l/mol}\cdot\text{cm}$, $\Delta\nu \sim 500 \text{ cm}^{-1}$) by using Strickler-Berg relation [160]. Thus, the relaxation time is estimated to be 15 fs, which is shorter than the time resolution of the present system. Therefore, the observed decay with the time constant of 0.7 ps cannot be attributed to the process from ${}^2\text{Q}$ to ${}^2\text{T}_1$.

For the observed decay, there are two other possibilities. One is the thermalization process between ${}^2\text{T}_1$ and ${}^4\text{T}_1$. Similar phenomena were observed in solutions of paramagnetic copper and silver protoporphyrins. Because copper and



$$\lambda_{\text{exc.}} = 620 \text{ nm}$$

Figure 4-10 Differential transmission spectra of $(t\text{-Bu})_{1,1}\text{VOPc} / \text{CHCl}_3$



$\lambda_{exc.} = 620 \text{ nm} ; \lambda_{probe} = 700 \text{ nm}$

○ : Data

— : Fitting curves consisting of an exponential term with time constant of 0.7 ps and a constant term

Figure 4-11 Transmittance change of $(t\text{-Bu})_{1,1}\text{VOPc} / \text{CHCl}_3$ as a function of time delay

silver have an unpaired electron as in vanadyl, their electronic energy-level schemes are similar to that of a vanadyl phthalocyanine molecule. The energy separation between these two states were reported to be about 100 and 300 cm^{-1} for copper phthalocyanine and copper porphyrin, respectively [161,162,163]. In these protoporphyrins, the fast relaxation from ^2Q to $^2\text{T}_1$ was reported to take place within the time resolution, 8 ps, and the thermalization between $^2\text{T}_1$ and $^4\text{T}_1$ followed at the time constant of *ca.* 450 ps and *ca.* 11 ps for copper and silver porphyrins, respectively [164]. If the energy separation between $^2\text{T}_1$ and $^4\text{T}_1$ in vanadyl phthalocyanine is larger than those in copper and silver protoporphyrins, it is possible that the thermalization process takes place much faster in this molecule.

The other possibility is that the decay is taking place in dimers. In dimers, since the unpaired electrons of two molecules couple and Kramers degeneracy is lifted, the energy level diagram is considered to be similar to that of phthalocyanine ligand illustrated in Fig. 4-5 [136]. The ground state (^1A) and the first-excited Q-band state (^1Q) are singlets and between these two states a triplet state ($^3\text{T}_1$) lies. In this system, because the nonradiative transition from ^1Q to $^3\text{T}_1$ is spin forbidden and the rate must be lower than that of ^2Q to $^2\text{T}_1$ transition, it is possible that the observed decay component corresponds to the relaxation from ^1Q to $^3\text{T}_1$ in dimers. However, although it is reported that dimerization of VOPc molecules takes place even at the molecular concentration as low as 10^{-5} mol/l [136], the present compound, $(t\text{-Bu})_{1,1}\text{VOPc}$, has high solubility in chloroform and the dimer fraction was estimated to be less than 1 % at 10^{-4} mol/l from the concentration dependence of the absorption spectrum. Therefore, we attribute the decay to the thermalization process between $^2\text{T}_1$ and $^4\text{T}_1$ in monomers rather than the latter process in dimers.

The relatively large constant term persisting for longer than hundreds of picoseconds is due to the high yield of $^2\text{T}_1$ and $^4\text{T}_1$. Their lifetimes, which have not

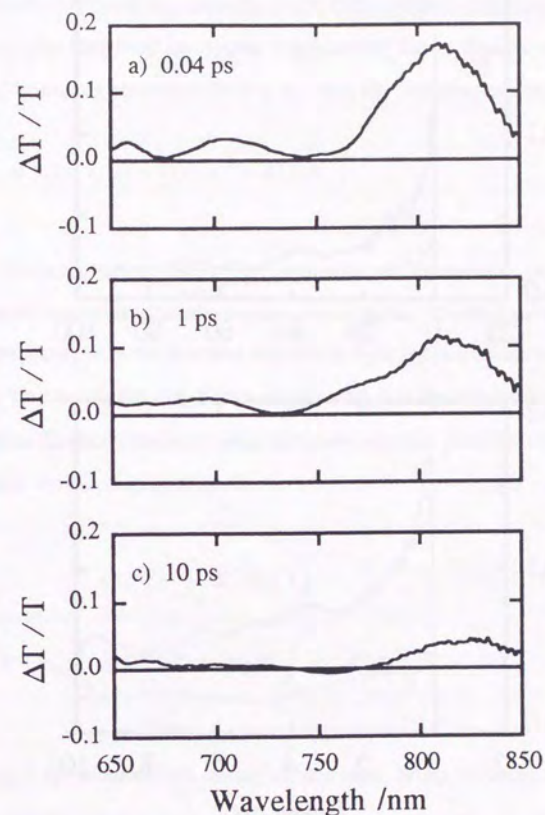
been determined yet because of the low phosphorescence yields, are much longer than the temporal range of observation (~ 100 ps) but are shorter than $100 \mu\text{s}$, the period of excitation pulses. This is consistent with the phosphorescence lifetime of $3 \mu\text{s}$ observed in copper phthalocyanine [161].

The pump-probe measurements were also carried out on a dilutely doped polystyrene film of the same molecule. The results were similar to those obtained for the above solution sample.

4.5.2. Phase II

Figure 4-12 shows DTS of phase II films of $(t\text{-Bu})_{1,1}\text{VOPc}$ doped in polystyrene (10 wt%). The outstanding feature is that significant bleaching appears at the lowest energy absorption peak (*ca.* 810 nm), while the higher energy absorption peaks bleach very weakly. This indicates that excitons created by the femtosecond pulses at 620 nm either undergoes very rapid internal conversion to the lowest excited state, and/or induced excited-state absorption in this energy region cancels the bleaching signals. In the spectral range of 500-600 nm, corresponding to the window of the ground-state absorption, induced excited-state absorption was observed, which was much weaker than the bleaching signal.

In the following, we focus on the decay kinetics of the bleaching peak. The temporal response of bleaching at 810 nm is shown in Fig. 4-13 for excitation intensities of 20 and $5 \text{ GW}/\text{cm}^2$, respectively. The decay curve of the transmittance change consists of three components: a fast (subpicosecond) component, a slower (tens of picoseconds) component, and a much slow (more than hundreds of picoseconds) component. Because the fast decay rate appears to have excitation-intensity dependence, it is considered to represent a bimolecular process, *i.e.*, exciton-exciton annihilation. The slower decay is rather independent of excitation



$$\lambda_{\text{exc.}} = 620 \text{ nm}$$

Figure 4-12 Differential transmission spectra of phase II $(t\text{-Bu})_{1,1}\text{VOPc}$ / polystyrene (10 wt%)

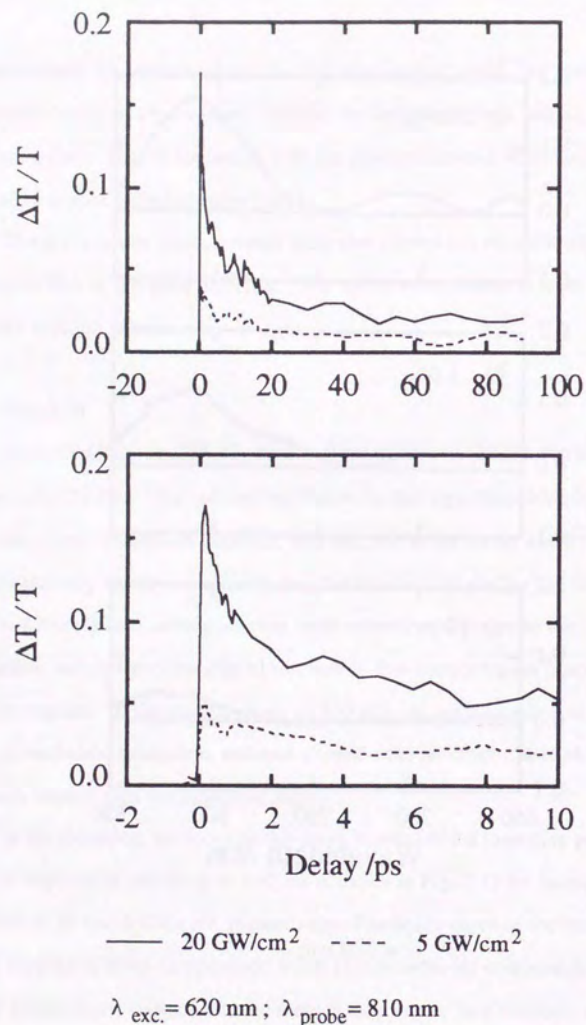


Figure 4-13 Excitation-intensity dependent time evolution of transmittance change of phase II (t-Bu)_{1,1} VOPc / polystyrene

intensity and attributed to a monomolecular decay without interaction between excitons. The long-lived component is presumably due to triplet-state formation.

The exciton population density, n , obeys the following rate equation:

$$\frac{dn}{dt} = \sigma n_g(t) I_L(t) - \Gamma(t) \cdot n^2 - K(t) \cdot n \quad (4-1)$$

where $\Gamma(t)$ is the exciton-decay rate via bimolecular annihilation processes and $K(t)$ is the decay rate without interaction between excitons. The first term of the r.h.s. of the above equation is the pumping rate, where $I_L(t)$ is the excitation-laser intensity, $n_g(t)$ is the ground-state population density, and σ is the absorption cross section. For a delta-function excitation pulse, the above equation gives the following time-dependent exciton density at $t > 0$:

$$\frac{n}{n_0} = \frac{\exp \left[- \int_0^t dt' K(t') \right]}{1 + n_0 \int_0^t dt'' \Gamma(t'') \exp \left[- \int_0^{t''} dt' K(t') \right]} \quad (4-2)$$

where n_0 is the initial exciton density at time zero. When the decay rate via bimolecular processes is much greater than that of monomolecular ones, the differential transmission $\Delta T/T$, which is the value observed in experiments, is related to this exciton density, n , by the sum of a term proportional to n and a constant term, which is due to bottleneck states, e.g., triplet states, photocarriers, and/or trap states, possessing lifetimes much longer than the time range of the observation.

In our experimental condition, the monomolecular decay rate, $K(t)$, is considered to be a constant, k , because there are no energy acceptors in the samples.

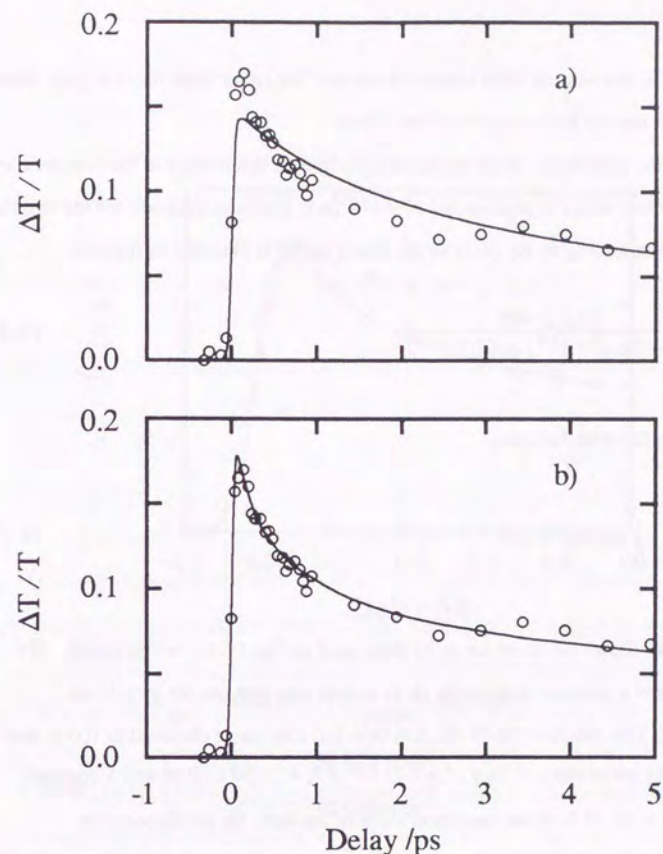
On the other hand, $\Gamma(t)$ can be either a constant, γ , or a certain time-dependent rate, $\gamma \cdot t^{-1/2}$, depending on the nature of the interaction mechanism between excitons. The constant decay rate reflects the annihilation of excitons during their hopping migration in the crystallines, while the inverse of square-root-time dependence describes the annihilation via the long-range dipole-dipole interaction between excitons [165-168] or that in the manner of the motion-limited diffusion [168].

Similar experimental results were observed by other groups. Ho and Peyghambarian have studied a polycrystalline film of AlPc-F [142], of which absorption spectrum was similar to our phase II films. They explained the decay of the bleaching by assuming a constant decay rates for $\Gamma(t)$ and $K(t)$. On the other hand, Greene and Millard [141], have studied a polycrystalline film of β -H₂Pc and found out that the initial decay of induced excited-state absorption signal is described by a time-dependent ($t^{-1/2}$) exciton-exciton annihilation rate, although they did not included a monomolecular decay term.

The present data were fitted in two ways in order to clarify the dominant mechanism of the exciton annihilation process in the present molecular system. In the model, which assumes constant decay rates for both $\Gamma(t)$ and $K(t)$, which are represented as γ and k here, respectively, the time-dependent exciton density after delta-function-pulse excitation is calculated from Eq. (4-2) as follows [169,170]:

$$\frac{n}{n_0} = \frac{\exp[-kt]}{1 + (n_0\gamma/k)(1 - \exp[-kt])} \quad (4-3)$$

Fitting of our data of 20-GW/cm² excitation intensity according to this model is shown in Fig. 4-14a. The long-lived component was included by adding a constant term in



- a) for the model with constant mono- and bimolecular decay rates
 b) for the model with a $t^{-1/2}$ dependent bimolecular and a constant monomolecular decay rates

$$\lambda_{\text{exc.}} = 620 \text{ nm} ; \lambda_{\text{probe}} = 810 \text{ nm}$$

○ : Data — : Fit

Figure 4-14 Fitting of the decay of transmittance change of phase II (*t*-Bu)_{1,1} VOPc / polystyrene

Eq. (4-3). In this way we were able to fit our data for either short times or long times, but not over the full time range from 0 to 100 ps.

On the other hand, in the model containing time dependence in the bimolecular decay rate $\Gamma(t)$, which is represented as $\gamma' \cdot t^{-1/2}$ here, a similar equation for the exciton density corresponding to Eq. (4-3) in the above model is obtained as follows:

$$\frac{n}{n_0} = \frac{\exp[-kt]}{1 + (2n_0\gamma' / k^{1/2}) \operatorname{erf}[(kt)^{1/2}]}, \quad (4-4)$$

where erf is the error function:

$$\operatorname{erf}[x] = \int_0^x du \exp[-u^2]. \quad (4-5)$$

Figure 4-14b shows the fit of the same data, used in Fig. 4-14a, to this model. We have included a constant term in Eq. (4-4) to take into account the long-lived component. This function can fit the data over full time range observed to 100 ps and yields fitting parameters of $(n_0\gamma')^{-1} = 1.1 \times 10^{-6} \text{ s}^{1/2}$, $k^{-1} = 50 \pm 20 \text{ ps}$ and a constant term which is ca. 10% of the maximum value of the data. By considering the excitation density inside the polystyrene film, γ' is estimated to be $6.5 \times 10^{-14} \text{ cm}^3 \text{ s}^{-1/2}$. However, the effective excitation density should be higher in phthalocyanine aggregates by a factor of the inverse of the volume fraction of the aggregates in the host polymer. This compensation leads the effective value of γ' to $3.8 \times 10^{-15} \text{ cm}^3 \text{ s}^{-1/2}$. The dependence of bleaching decay on excitation intensity is also shown in Fig. 4-15.

Measurements were carried out also on other phase II films of vanadyl phthalocyanines, *i.e.*, a spin-coated film of $(t\text{-Bu})_{1,1}\text{VOPc}$ without host polymer and a

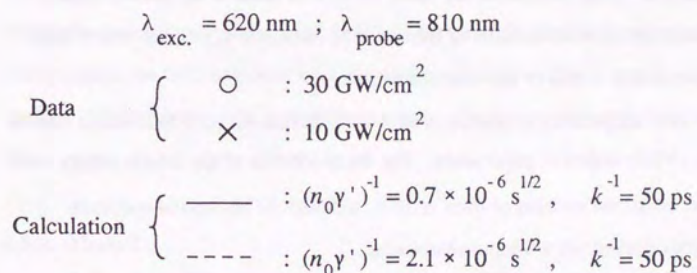
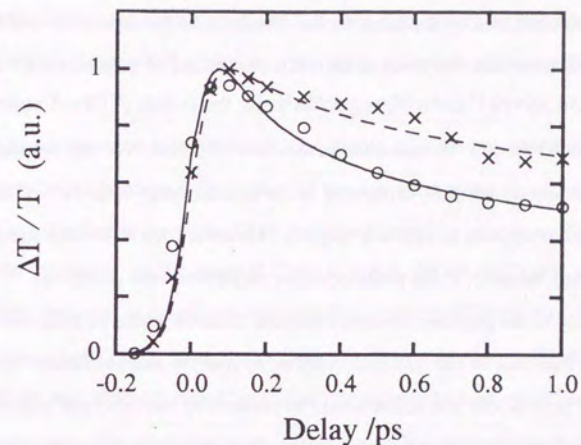


Figure 4-15 Comparison of bleaching decay of phase II $(t\text{-Bu})_{1,1}\text{VOPc}$ / polystyrene excited at two different intensities

vapor-deposited film of VOPc, in order to examine the effect of the host polymer as well as the steric hindrance of *t*-butyl substituents. The decay curves of their bleaching peak at *ca.* 810 nm showed almost the same behavior as the above case and were also well described by the latter model including a time-dependent exciton-exciton annihilation rate. In these cases, estimated values of parameters k^{-1} and γ' were 50 ps and $5.9 \times 10^{-15} \text{ cm}^3 \text{ s}^{-1/2}$, respectively, for the $(t\text{-Bu})_{1,1}$ VOPc film, and were 50 ps and $6.0 \times 10^{-15} \text{ cm}^3 \text{ s}^{-1/2}$, respectively, for the VOPc film. We can say that the *t*-butyl substituent causes little difference in the exciton decay rates both γ' and k . The host polymer appears to reduce γ' slightly. However, this difference should be said to be small, because, if the phthalocyanine molecules were distributed homogeneously in the polymer, the intermolecular distance would be from two to three times longer than that of the undoped samples, so that the energy-transfer rate through the dipole-dipole interaction would be reduced by two orders of magnitude and also the exciton mobility would be much lower. Thus we conclude that the effect of the host polymer on the exciton decay rates, γ' and k , is weak in the present dopant concentration (10 wt%) because of formation of molecular aggregates with a local structure similar to that of the undoped films.

Low temperature experiments have been carried out on a spin-coated film of $(t\text{-Bu})_{1,1}$ VOPc doped in polystyrene. The decay kinetics of the lowest energy excitons remained unchanged even at 10 K, although its absorption spectrum undergoes marked red shift and sharpening.

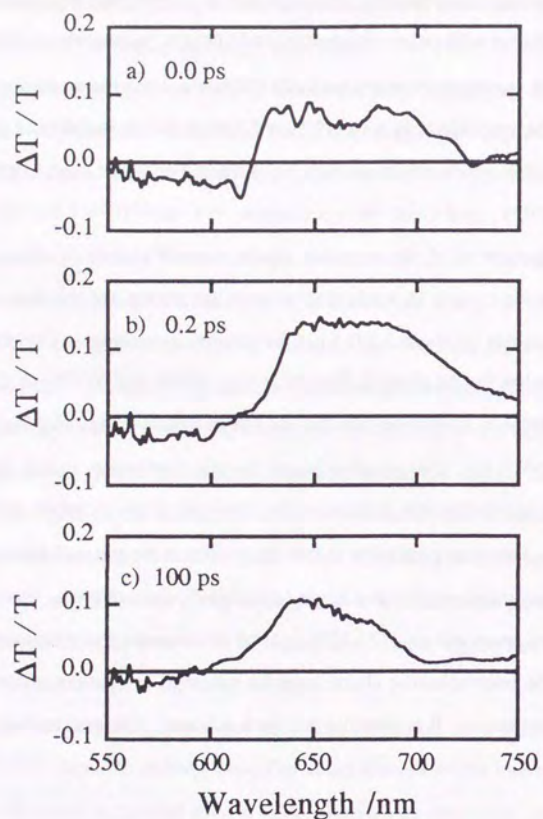
The fact that the initial decay kinetics of excitons is described by the time-dependent ($t^{-1/2}$) bimolecular-decay-rate model suggests either that the interaction between excitons are dominated by the long-range dipole-dipole interaction [141,165-168] rather than direct collision of excitons at neighboring molecules, or that excitons diffuse in a motion-limited manner [141,168]. The long-range dipole-dipole

interaction model seems to be consistent with that this decay rate was insensitive to temperature, and also with our experimental condition, *i.e.*, n_0 was about $2 \times 10^{20} \text{ cm}^{-3}$ under the typical excitation intensity used (20 GW/cm^2), while the molecular density is estimated to be approximately $1.65 \times 10^{21} \text{ cm}^{-3}$ from lattice parameters of phase II VOPc crystal [135], which means one exciton is created on about every eight molecules.

From the value of γ' , the transition-dipole moment between excited states was estimated to be about 3 D, while that between the ground and the first excited state was estimated to be about 3.2 D from the absorption spectrum. The coefficients γ' of our estimation for the phase II films of $(t\text{-Bu})_{1,1}$ VOPc and VOPc are greater by more than one order of magnitude than that for a polycrystalline film of $\beta\text{-H}_2\text{Pc}$, $1.0 \times 10^{-16} \text{ cm}^3 \text{ s}^{-1/2}$ [141]. One possible reason for this discrepancy is that the value for $\beta\text{-H}_2\text{Pc}$ was underestimated because of the extremely high excitation density in the experiment. The other possibility is that the exciton in the phase II form of vanadyl phthalocyanines might have larger transition-dipole moments. The data of electroabsorption spectroscopy [137,138] and the photoconductivity measurements [139] suggest the intermolecular charge-transfer nature of excitons in phase II vanadyl phthalocyanines. It is possible that such a feature is related to their faster decay rates.

4.5.3. Phase I

In Fig. 4-16, DTS of a phase I film of $(t\text{-Bu})_{1,1}$ VOPc doped in polystyrene (10 wt%) are shown. Contrary to those of phase II samples, bleaching of the absorption appeared over the full spectral range of the Q band, which has absorption peaks at *ca.* 650 and 700 nm, and also induced excited-state absorption appeared at shorter wavelength side, 500-600 nm, which was stronger than that in phase II



$$\lambda_{\text{exc.}} = 620 \text{ nm}$$

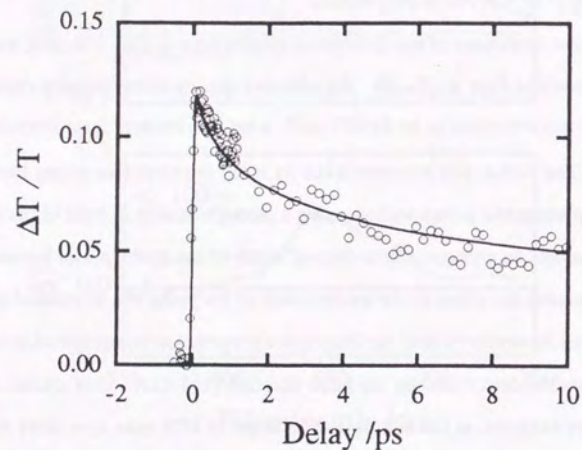
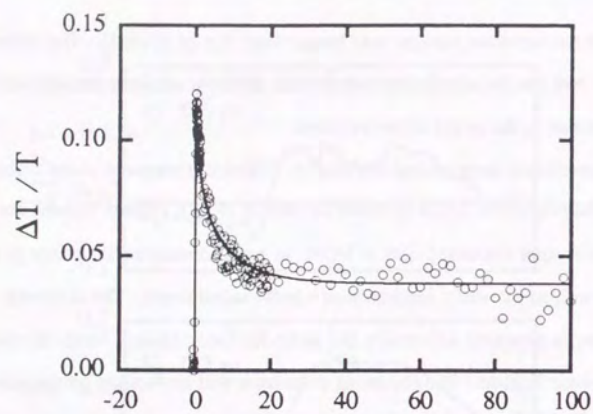
Figure 4-16 Differential transmission spectra of phase I $(t\text{-Bu})_{1,1}\text{VOPc}$ / polystyrene (10 wt%)

samples. Its excited-state lifetime was longer than that of phase II. The differences between the two spectra are clearly due to their different stacking arrangements and hence differences in the origin of the excitons.

Measurements were carried out also on differently prepared phase I films of vanadyl phthalocyanines, *i.e.*, a spin-coated film of $(t\text{-Bu})_{1,1}\text{VOPc}$ without the host polymer and a vapor-deposited film of VOPc, in order to examine the effect of the host polymer as well as the steric hindrance of *t*-butyl substituents. The observed transient spectra appeared essentially the same for those phase I films, as was also the case in phase II films. The following discussion will be focused on the spin-coated film of $(t\text{-Bu})_{1,1}\text{VOPc}$ doped in polystyrene.

Temporal evolutions of the differential transmission at 700, 650, 620, and 550 nm are shown in Figs. 4-17 – 20. The effective density of the initially created excitons, n_0 , was estimated to be $3 \times 10^{20} \text{ cm}^{-3}$, when the incident laser intensity was 20 GW/cm^2 . The data at 620 nm were taken by using the amplified pulses themselves for both pump and probe pulses without using a monochromator in front of the detector. This allows to take an average over a spectral width of the probe pulses around 620 nm and remove the effect of the spectral shift of the probe due to induced phase modulation and the artifact due to the high spectral resolution compared with the temporal resolution determined by the pulse duration [114-121]. This artifact is manifested, for example, as the antisymmetric shape of DTS near zero delay observed around excitation wavelength (620 nm) in Fig. 4-16a. These kinds of behaviors will be discussed in Subsection 4.5.5.

The decay kinetics at 700 nm had excitation-intensity dependence, as shown in Figs. 4-17 and 4-21, and consisted of three components just as in the case of the bleaching observed in phase II samples. We attribute the fast component to exciton-exciton annihilation process, the slower component to monomolecular nonradiative



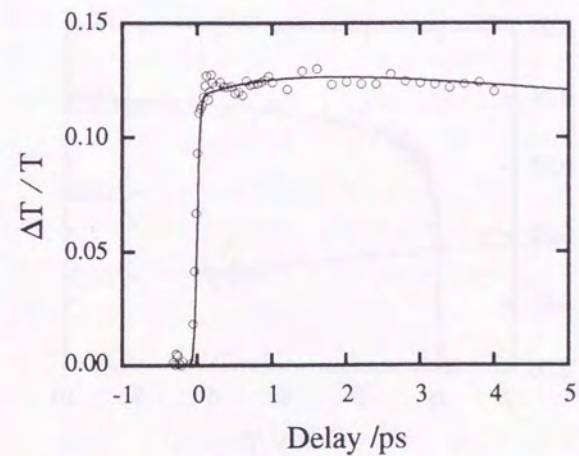
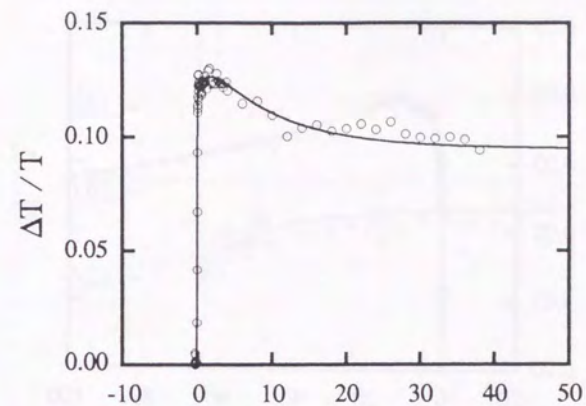
$\lambda_{exc.} = 620 \text{ nm} ; \lambda_{probe} = 700 \text{ nm}$

○ : Data

— : Fitting curves for the model with a $t^{-1/2}$ dependent bimolecular decay rate

$$(n_0 \nu)^{-1} = 2.5 \times 10^{-6} \text{ s}^{1/2}, k^{-1} = 10 \text{ ps}$$

Figure 4-17 Transmittance change of phase I $(t\text{-Bu})_{1.1}$ VOPc / polystyrene as a function of time delay (1)

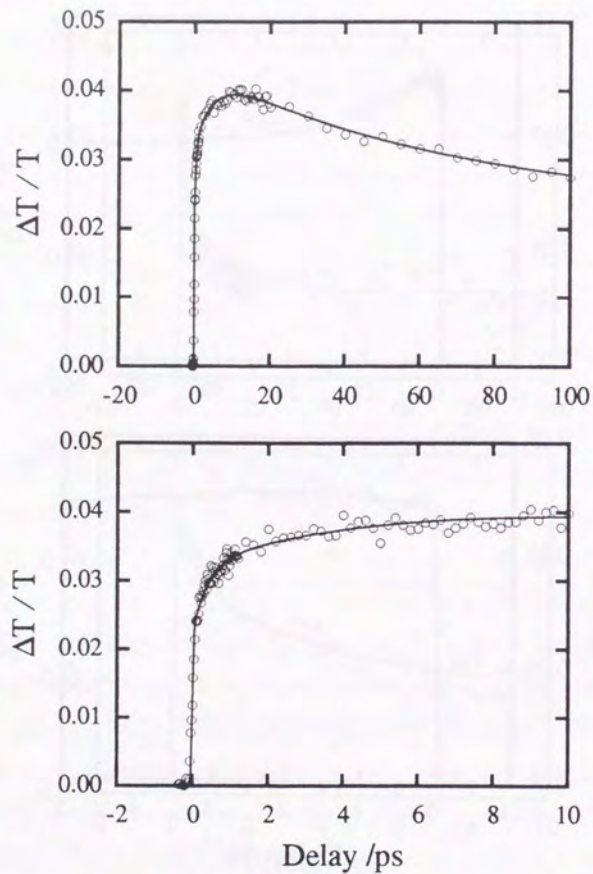


$\lambda_{exc.} = 620 \text{ nm} ; \lambda_{probe} = 650 \text{ nm}$

○ : Data

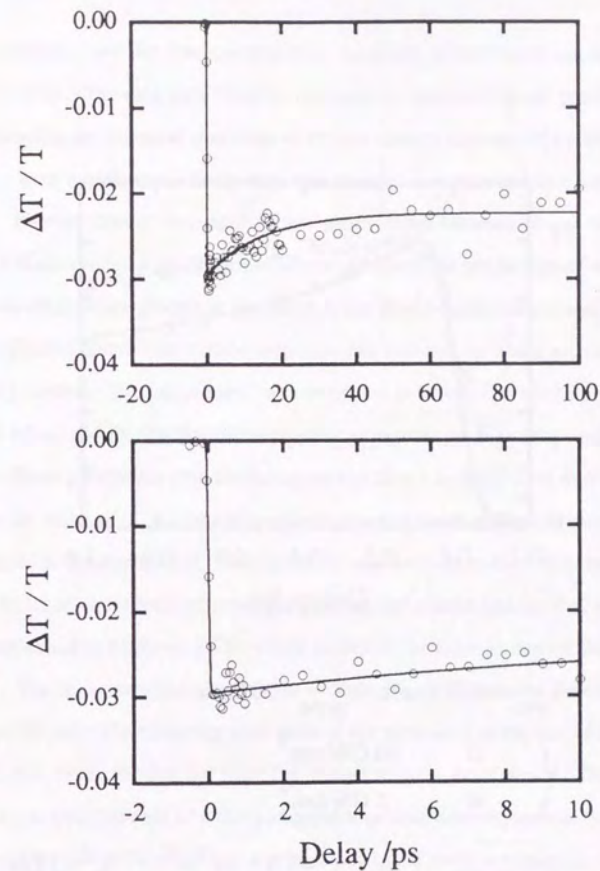
— : Fitting curves consisting of a constant term and two exponential terms with rise time constant of 1.5 ps and decay time constant of 10 ps

Figure 4-18 Transmittance change of phase I $(t\text{-Bu})_{1.1}$ VOPc / polystyrene as a function of time delay (2)



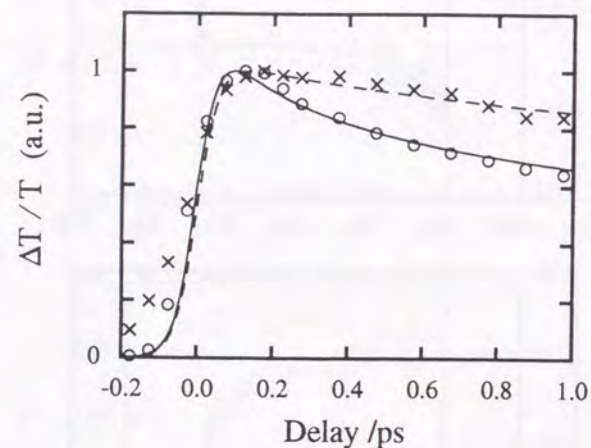
$\lambda_{exc.} = \lambda_{probe} = 620 \text{ nm}$; without spectral resolution
 ○ : Data
 — : Fitting curves consisting of a constant term and three exponential terms with rise time constants of 0.4 and 4.5 ps and decay time constant of 70 ps

Figure 4-19 Transmittance change of phase I $(t\text{-Bu})_{1.1}$ VOPc / polystyrene as a function of time delay (3)



$\lambda_{exc.} = 620 \text{ nm}$; $\lambda_{probe} = 550 \text{ nm}$
 ○ : Data
 — : Fitting curves consisting of a constant term and an exponential term with time constant of 15 ps

Figure 4-20 Transmittance change of phase I $(t\text{-Bu})_{1.1}$ VOPc / polystyrene as a function of time delay (4)



$$\lambda_{\text{exc.}} = 620 \text{ nm} ; \lambda_{\text{probe}} = 700 \text{ nm}$$

$$\text{Data} \quad \left\{ \begin{array}{l} \circ : 30 \text{ GW/cm}^2 \\ \times : 5 \text{ GW/cm}^2 \end{array} \right.$$

$$\text{Calculation} \quad \left\{ \begin{array}{l} \text{—} : (n_0 \gamma')^{-1} = 1.5 \times 10^{-6} \text{ s}^{1/2}, \quad k^{-1} = 10 \text{ ps} \\ \text{---} : (n_0 \gamma')^{-1} = 9.0 \times 10^{-6} \text{ s}^{1/2}, \quad k^{-1} = 10 \text{ ps} \end{array} \right.$$

Figure 4-21 Comparison of bleaching decay of phase I $(t\text{-Bu})_{1,1}\text{VOPc}$ / polystyrene excited at two different intensities

decay process, and the slow component to formation of bottleneck states such as triplet states. The data were fitted in two ways as described in the preceding section by assuming the temporal evolution of exciton density represented by Eq. (4-3) or (4-4). Both models could fit the data well over the full observed time range in this case. Because similar data taken at low temperatures between 10 and 50 K showed only a slight change from those at room temperature, the mechanism of exciton-exciton annihilation process is attributed to the dipole-dipole interaction, as in phase II films, rather than exciton migration and collision, in which activation energy is usually needed. The parameter γ' was estimated to be *ca.* $1.3 \times 10^{-15} \text{ cm}^3 \text{ s}^{-1/2}$, k^{-1} to be 10 ± 5 ps, and the fraction of the constant term to be *ca.* 0.3 of the peak value of the data. These parameters give the fitting curves shown by solid lines in Fig. 4-17. From the value of γ' , the transition-dipole moment between excited states was estimated to be about 0.8 D. This value, as well as γ' , is smaller than that of phase II by a factor of about four, whereas that between the ground and the first excited state was estimated to be about 3.5 D, which is almost the same as that of phase II.

The response of the bleaching at 650 nm, Fig. 4-18, behaved differently from that at 700 nm. The bleaching took place at the same time as the rise of the excitation pulse, and, even after this fast rise, it continued to grow more slowly. This component with a rise time constant of a few picoseconds probably corresponds to the creation of the excitons due to the annihilation of excitons in the lower energy state at 700 nm in the absorption spectrum. As illustrated in Fig. 4-22, it is considered that a part of the excitons in $S_1^{(1)}$ state annihilated via the bimolecular process was once excited into a higher singlet exciton state, S_n , and repopulated at this energy states after the successive rapid internal conversion from S_n to $S_1^{(2)}$. After this initial event, the bleaching signal decays with time constant of *ca.* 10 ps and about 0.7 of the peak signal remains for much longer than 100 ps. The signal fraction of the long-lived

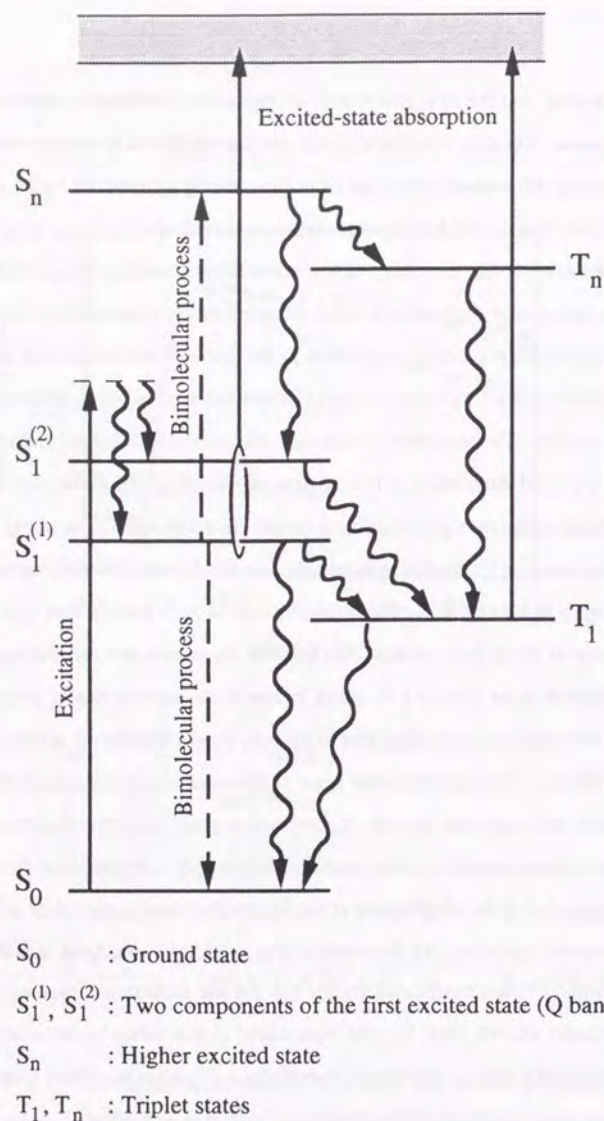


Figure 4-22 Energy level diagram of VOPc in phase I

component is much higher than that observed at 700 nm. This suggests that, although $S_1^{(2)}$ is a higher energy level than $S_1^{(1)}$, the decay from $S_1^{(2)}$ to $S_1^{(1)}$ is much slower than usual internal conversion processes. And also, excitons in this state do not appear to undergo exciton-exciton annihilation by interacting with each other.

Similar slow rise of bleaching following excitation was also observed in the data at 620 nm, Fig. 4-19. However, because this response did not show excitation-intensity dependence, it is attributed to the broadening of the burned spectral hole centered at 650 nm to the blue side of the absorption band. Fitting of the data was made to a triexponential function with a constant term, for instance. It yielded rise time constants of 0.4 ± 0.1 and 4.5 ± 1 ps, a decay time constant of 70 ± 20 ps, and a fraction of the constant term of *ca.* 0.5 of the peak value of the data.

The decay kinetics of the induced excited-state absorption at 550 nm, Fig. 4-20, had a decay rate of 15 ± 3 ps and a constant term of 0.7 of the peak value of the data. Thus the observed induced absorption at 550 nm must be taking place from $S_1^{(2)}$, whose lifetime is *ca.* 10 ps, and T_1 , whose lifetime is much longer than 100 ps.

The present observation found that two types of excitons created in the phase I form corresponding to the two absorption peaks in the Q band, *i.e.*, $S_1^{(1)}$ and $S_1^{(2)}$ in the schematics in Fig. 4-22, behave totally differently. Excitons in $S_1^{(1)}$ state relax rapidly, but more slowly than those in phase II, by exciton-exciton annihilation via the dipole-dipole interaction, and a part of them creates population in $S_1^{(2)}$ state after annihilation via higher excited states. On the other hand, excitons in $S_1^{(2)}$ state interact only weakly with each other and have a long lifetime *ca.* 10 ps.

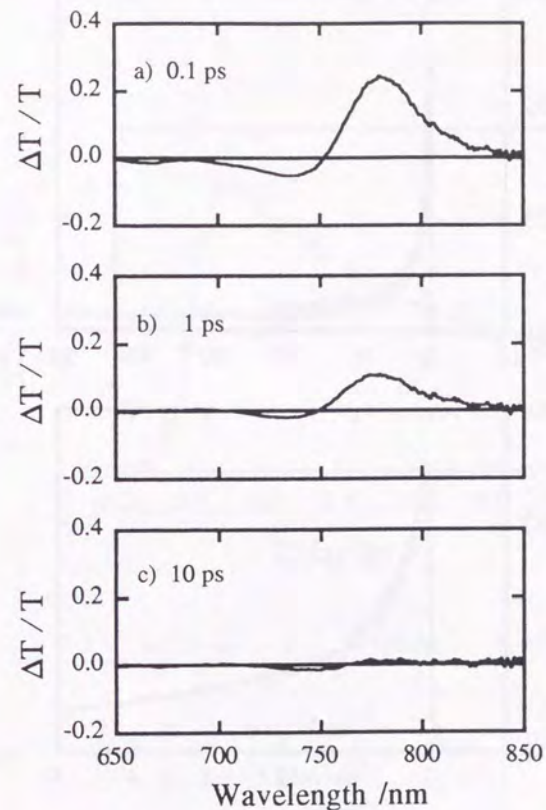
4.5.4. Films deposited on KBr

In this subsection discussion is given on a novel solid-state phase of VOPc grown on a potassium-bromide (KBr) substrate by the organic molecular-beam-

epitaxy technique, which has an electronic structure different from those in phases I and II described in the preceding subsections.

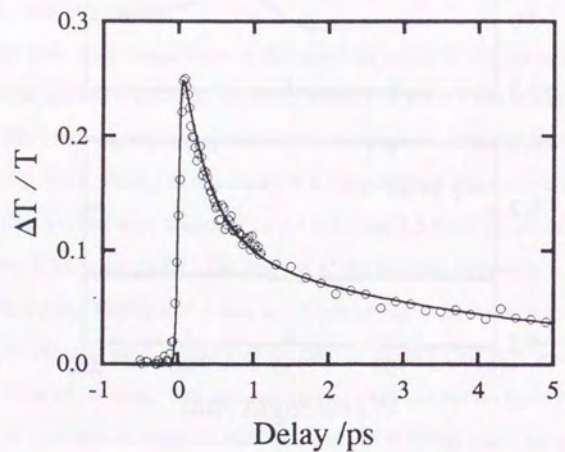
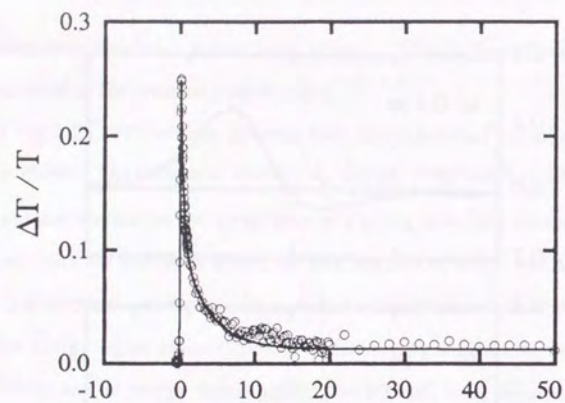
In Fig. 4-23, DTS at three different time delays between pump and probe pulses are shown. The excitation density, n_0 was *ca.* $2 \times 10^{20} \text{ cm}^{-3}$. The outstanding features of these spectra are the appearance of a strong bleaching around 780 nm immediately after the excitation within the time resolution, which corresponds to the peak of its absorption spectrum, and a signal of induced excited-state absorption at a little higher energy region around 730 nm. Relatively weak bleaching peak appeared around 690 nm and, at energy region higher than 660 nm, weak induced excited-state absorption was observed.

The time-delay dependence of the bleaching signal at 780 nm is shown in Fig. 4-24. In marked contrast to the decay kinetics of phase I and II films, the initial decay of this bleaching signal appeared to be independent of excitation intensity, as shown in Fig. 4-25. Fitting of this decay to a biexponential function including a constant term yielded time constants of 0.4 ± 0.1 and 3.5 ± 0.5 ps, whose fraction were *ca.* 0.62 and 0.32, respectively. The fraction of the constant term was *ca.* 0.06 of the peak of the signal. Fitting of the data at 730 nm in Fig. 4-26 resulted in almost the same values of parameters except that the ratio of the constant term was *ca.* 0.1 to the peak value of the data. The induced excited-state absorption lasting more than hundreds of picoseconds suggests that the transition is taking place not only from the first excited state but also from bottleneck states. The data taken by the pump-probe method with amplified pulses (620 nm) themselves for both excitation and probe are shown in Fig. 4-27. In this case, induced excited-state absorption appeared at early times and it turned to bleaching after 2 ps. The obtained decay time constants were the same as those of the above within experimental error. At this wavelength, the



$$\lambda_{\text{exc.}} = 620 \text{ nm}$$

Figure 4-23 Differential transmission spectra of VOPc deposited on KBr

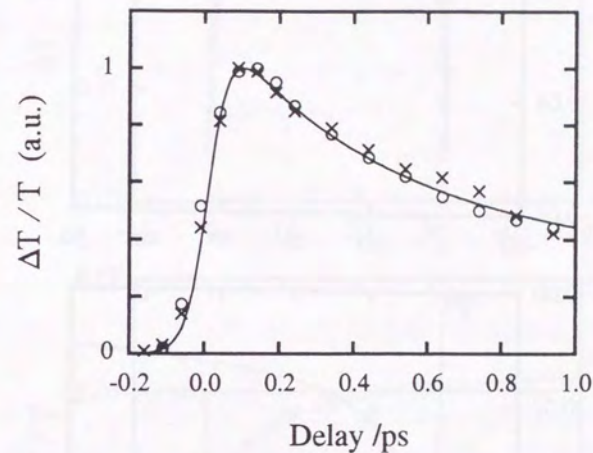


$\lambda_{exc.} = 620 \text{ nm}$; $\lambda_{probe} = 780 \text{ nm}$

○ : Data

— : Fitting curves consisting of a constant term and two exponential terms with time constants of 0.4 and 3.5 ps

Figure 4-24 Transmittance change of VOPc deposited on KBr as a function of time delay (1)

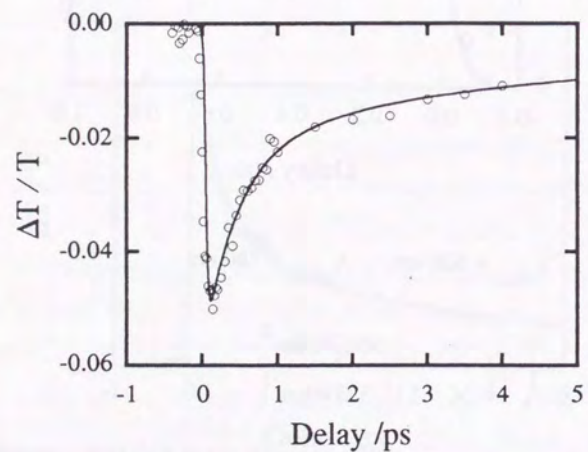
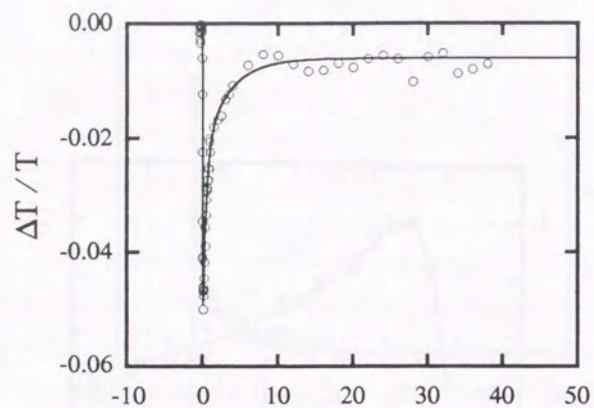


$\lambda_{exc.} = 620 \text{ nm}$; $\lambda_{probe} = 780 \text{ nm}$

Data { ○ : 30 GW/cm²
× : 5 GW/cm²

Calculation — : Biexponential decay with time constants of 0.4 and 3.5 ps

Figure 4-25 Comparison of bleaching decay of VOPc on KBr excited at two different intensities

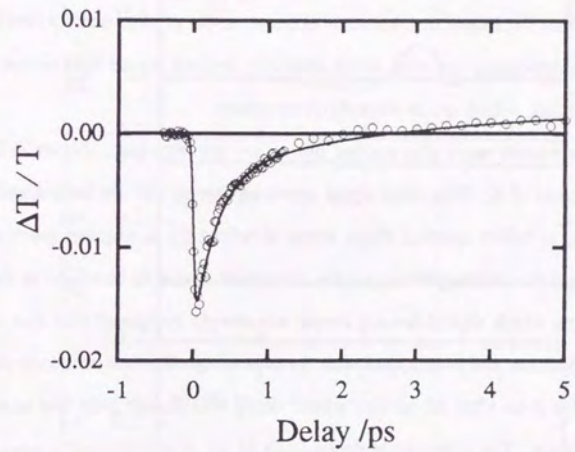
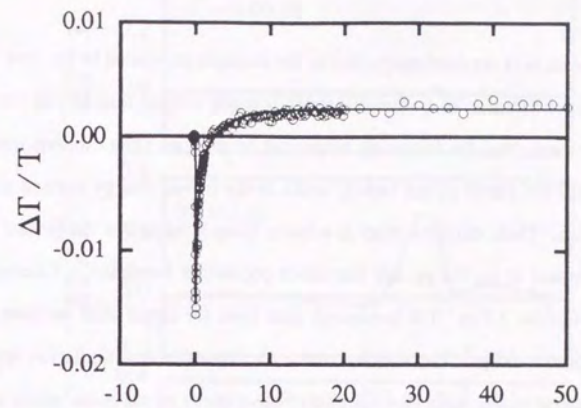


$\lambda_{\text{exc.}} = 620 \text{ nm}$; $\lambda_{\text{probe}} = 730 \text{ nm}$

○ : Data

— : Fitting curves consisting of a constant term and two exponential terms with time constants of 0.4 and 3.5 ps

Figure 4-26 Transmittance change of VOPc deposited on KBr as a function of time delay (2)



$\lambda_{\text{exc.}} = \lambda_{\text{probe}} = 620 \text{ nm}$; without spectral resolution

○ : Data

— : Fitting curves consisting of a constant term and two exponential terms with time constants of 0.3 and 3.0 ps

Figure 4-27 Transmittance change of VOPc deposited on KBr as a function of time delay (3)

induced absorption is predominantly due to the excitons populated in the first excited state and the contribution of bottleneck states is much weaker than at 730 nm.

From these data, the following model can be inferred. The excitons initially created by 620-nm pump pulses rapidly relax to the lowest-energy excited state around 780 nm. These excitons relax to a lower lying level and/or the ground state with time constant of *ca.* 0.4 ps, and bottleneck population formation is followed with time constant of *ca.* 3.5 ps. The bottleneck state lives for longer than the time range of our observation, ~ 100 ps. The absence of the exciton-exciton annihilation process is probably because of the rapid (0.4 ps) nonradiative decay of excitons, which takes place faster than the interaction between excitons at the present density level, due to the strong exciton-lattice coupling in the relatively ordered crystal film compared with phase I or II films, which are in amorphous structures.

Measurements were also carried out at low temperatures. Figure 4-28 shows DTS measured at 10 K. Bleaching signal appeared around 780 nm immediately after the excitation, of which spectral shape seems to reflect the absorption spectrum shown in Fig. 4-9. Induced excited-state absorption was also observed at the spectral region, which shifted toward longer wavelength compared with that observed at room temperature and overlapped with the bleaching. The transmittance change was observable even after 80 ps, *i.e.*, whose decay was slower than that observed at room temperature. The temperature dependence of the time evolution is much clear in Fig. 4-29, which shows the bleaching at 780 nm as a function of time delay for 10, 100, and 295 K. The initial relaxation time constants, 0.4 and 3.5 ps, remained almost unchanged even at 10 K. However, significant differences are seen after *ca.* 10 ps. At room temperature the bleaching recovered monotonically, whereas, at 10 K, it rather began to increase again at 10 ps, and the data at 100 K traced between the two. This observation, which was not the case in phases I and II, suggests the existence of a

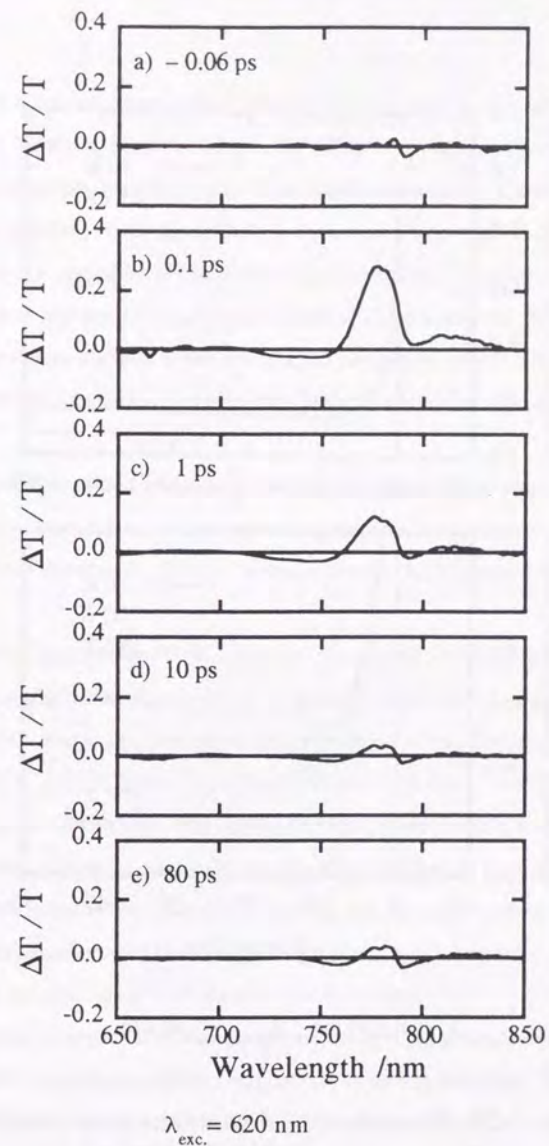


Figure 4-28 Differential transmission spectra of VOPc deposited on KBr at 10 K

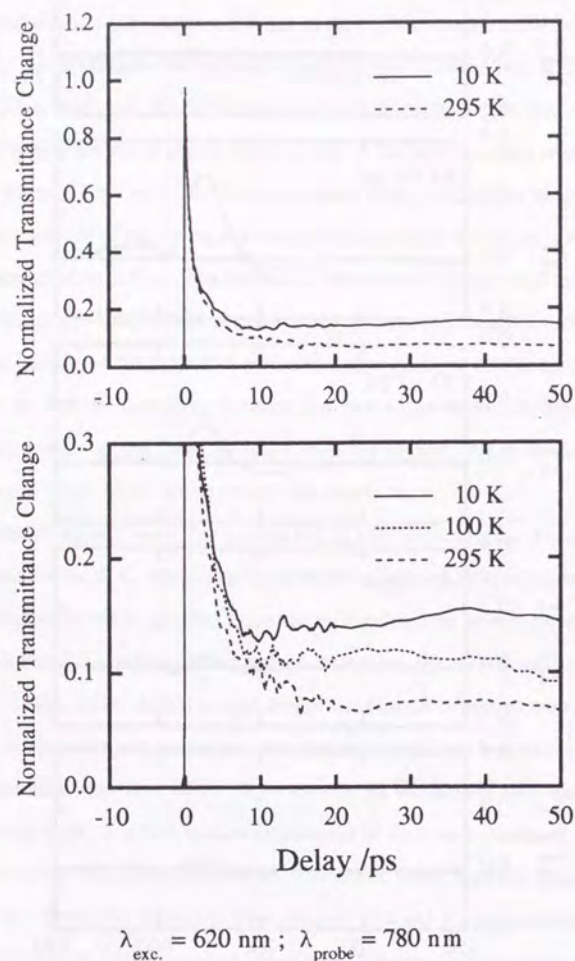


Figure 4-29 Temperature dependent time evolution of transmittance change of VOPc deposited on KBr

temperature dependent process of the formation of excitons at the lowest energy of the Q band. However, details of this kinetics still remain to be understood.

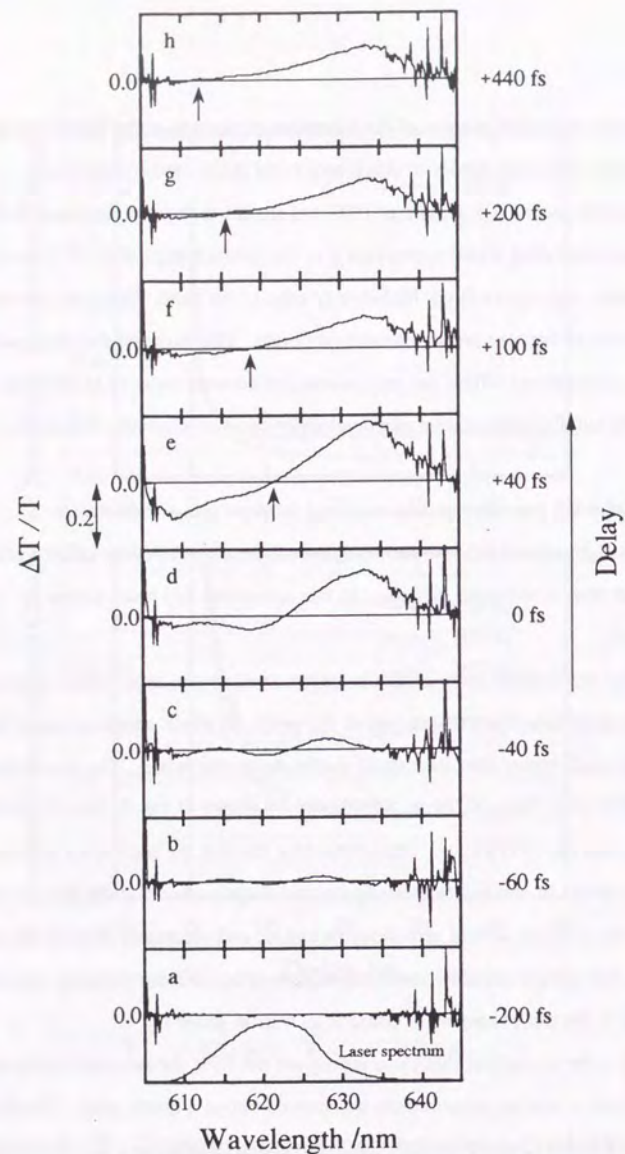
In this sample, the feature of DTS was similar to those of the phase II films in that strong bleaching signal appears only at the lowest-energy edge of Q band immediately after excitation at high-energy edge of the band. However, the relaxation mechanisms of excitons are significantly different. This suggests that molecular stacking arrangement affects not only interaction between excitons in different molecules but also nonradiative monomolecular decay mechanism of excitons.

4.5.5. Coherent transient phenomena and induced phase modulation

In Subsection 4.5.3., we have pointed out the novel behavior of DTS around the excitation laser wavelength, 620 nm. In this subsection this phenomenon is discussed.

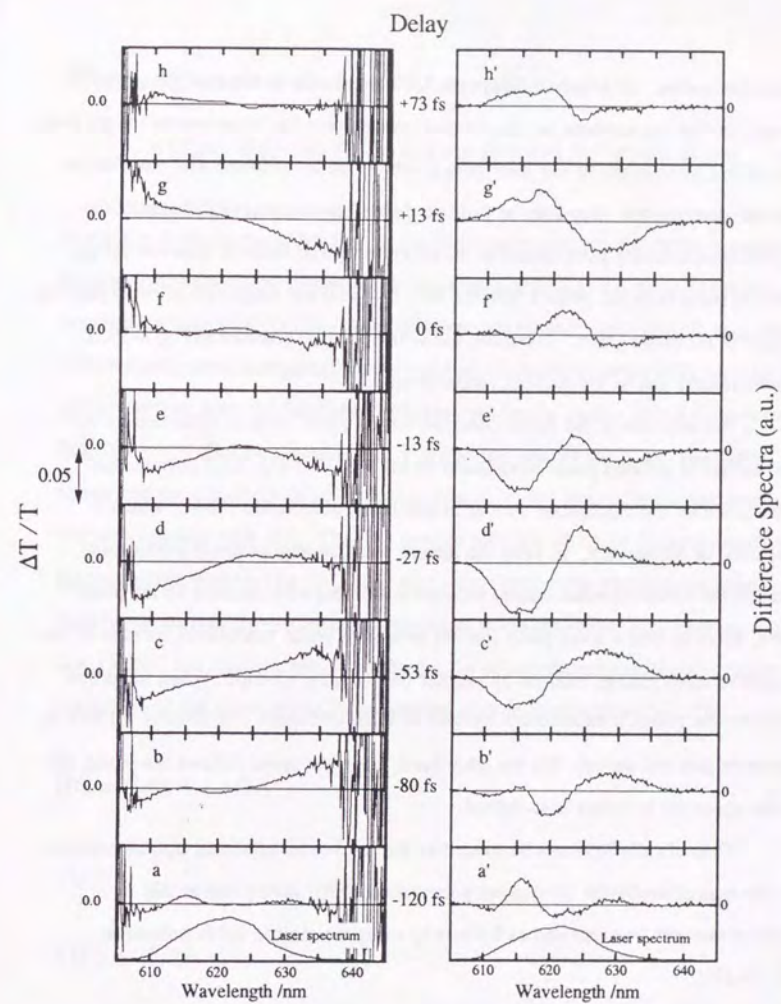
For the detailed study of this behavior, pump-probe experiments were carried out with amplified pulses themselves as the probe, in which condition signal-to-noise ratio was much higher than the case of continuum probe pulses. The results for a phase I film of (*t*-Bu)_{1,1}VOPc in polystyrene are shown in Fig. 4-30(a-h). Excitation intensity was *ca.* 20 GW/cm². The outstanding features are oscillatory structures at negative delays (b and c), steep antisymmetric shape centered at the spectral peak of the excitation pulses around zero delay (d and e), and successive shift of the zero-crossing wavelength toward shorter wavelength (e-h). Similar behavior was also observed in the other samples of phase II as well as phase I.

In order to confirm that these signals are not from the substrate but from the sample itself, a similar measurement was carried out on a quartz plate. The data are shown in Fig. 4-31, where the same data are plotted in two ways, *i.e.*, $\Delta I/I$ and ΔS ($= S' - S$), the difference between transmitted probe spectra with (S') and without (S)



The same pulses for both excitation and probe.
Arrows indicate "zero-crossing" points.

Figure 4-30 Differential transmission spectra of Phase I $(t\text{-Bu})_{1,1}$ VOPc/polystyrene around excitation wavelength



The same pulses for both excitation and probe.

Figure 4-31 Differential transmission spectra and difference spectra of a quartz plate; the same data are plotted in two ways.

excitation pulses. At negative delays the DTS are similar to those of the phase I sample in that the increase in transmission was observed at wavelengths longer than the central wavelength of the laser pulses, while that its decrease was observed at shorter wavelengths. However, at positive delays there appeared difference; the signals from a quartz plate turned to the opposite sign of those at negative delays, whereas those from the phase I film did not. And also the magnitude of the signal was greater in the phase I film. Therefore, the behavior of DTS shown in Fig. 4-30 is predominantly due to the phthalocyanine sample.

The behavior of the signal observed for the quartz plate is explained by the mechanism of induced phase modulation (IPM) [48,103-105]. This phenomenon takes place by the mechanism similar to self-phase modulation (SPM), which is discussed in Section 2.5. In SPM the intense pulse undergoes phase modulation through the refractive index change induced in a propagating medium by the pulse itself, while in IPM a weak pulse (probe) undergoes phase modulation because of the refractive index change induced by another intense pulse (pump). When the probe precedes the pump, it experiences increase in refractive index (for positive n_2) and its spectrum gets red-shifted. On the other hand, when the probe follows the pump, the probe spectrum becomes blue-shifted.

Theoretically IPM can be treated as the third-order nonlinear optical process. In transparent media the third-order polarization $\tilde{P}^{(3)}(t)$ giving rise to this phenomenon can be expressed as follows by using the electric fields defined in Eq. (3-23):

$$\tilde{P}^{(3)}(t) \propto \int_{-\infty}^{\infty} dt' R(t-t') \times [\tilde{E}_p(t) \tilde{E}_L(t'+\tau) \tilde{E}_L^*(t'+\tau) + g \tilde{E}_L(t+\tau) \tilde{E}_L^*(t'+\tau) \tilde{E}_p(t')] , \quad (4-6)$$

where $R(t)$ is the response function of the nonlinearity and g is the factor dependent on the origin of the nonlinearity and the polarization direction of the pump, the probe, and the detected beams [105,113]. When all these polarizations are parallel, as in the present experimental configuration, the value of g is equal to unity. This equation can also be derived from the third-order off-diagonal density matrix element expressed in Eqs. (3-25a)-(3-25c) by assuming the identical frequencies for pump and probe pulses and the extremely large dephasing rate ($\gamma \rightarrow +\infty$) and replacing the energy response function with $R(t)$. The first term in the r.h.s. of Eq. (4-6) corresponds to the incoherent process (Eq. (3-25a)), where the probe pulse experiences phase modulation induced by the intense pump pulse, while the second term corresponds to Eqs. (3-25b) and (3-25c), which represents the coherent coupling process between the pump and the probe pulses. The detected electric field is given by [105]

$$\tilde{E}(t) = \tilde{E}_p(t) + i \Delta\tilde{E}(t) , \quad (4-7)$$

where

$$\Delta\tilde{E}(t) \propto \tilde{P}^{(3)}(t) . \quad (4-8)$$

Then the power spectrum of the transmitted probe pulse is given by the Fourier transformation of the following field autocorrelation function:

$$G(t) \propto \int_{-\infty}^{\infty} dt' \bar{E}^*(t') \bar{E}(t' + t) . \quad (4-9)$$

The difference spectrum $\Delta S (= S' - S)$ between the transmitted probe spectrum with (S') and without (S) the pump pulse is expressed as follows:

$$\Delta S(\Delta\omega) \propto \int_{-\infty}^{\infty} dt \exp[i\Delta\omega t] \times [i \int_{-\infty}^{\infty} dt' \{ \bar{E}_p^*(t') \Delta \bar{E}(t' + t) - \bar{E}_p(t' + t) \Delta \bar{E}^*(t') \}] . \quad (4-10)$$

Here $\Delta\omega (= \omega - \omega_p)$ is the frequency measured from the central frequency of the incident laser pulse. Thus, it is expressed as the sum of the two contributions of the incoherent ($\Delta S_{[INC]}$) and the coherent coupling ($\Delta S_{[COH]}$) processes, *i.e.*,

$$\Delta S(\Delta\omega) = \Delta S(\Delta\omega)_{[INC]} + \Delta S(\Delta\omega)_{[COH]} , \quad (4-11)$$

where

$$\Delta S(\Delta\omega)_{[INC]} = - \text{Im} [\int_{-\infty}^{\infty} dt \exp[-i\Delta\omega t] \int_{-\infty}^{\infty} dy \int_{-\infty}^{\infty} dx \times R(y) \bar{E}_p^*(y + x + t) \bar{E}_p(y + x) |\bar{E}_L(x + \tau)|^2] \quad (4-12a)$$

and

$$\Delta S(\Delta\omega)_{[COH]} = - g \text{Im} [\int_{-\infty}^{\infty} dt \exp[-i\Delta\omega t] \int_{-\infty}^{\infty} dy \int_{-\infty}^{\infty} dx \times R(y) \bar{E}_p^*(y + x + t) \bar{E}_L(y + x + \tau) \bar{E}_L^*(x + \tau) \bar{E}_p(x)] . \quad (4-12b)$$

This is the general third-order expression of the spectral shift of the probe pulse due to IPM observable in the pump-probe type experiments.

When the response is instantaneous, *i.e.*, $R(t) = \delta(t)$, which is expected for the electronic nonlinearity, the above two terms give the same time-delay dependence of ΔS , *i.e.*,

$$\Delta S(\Delta\omega)_{[INC]} = \frac{1}{g} \Delta S(\Delta\omega)_{[COH]} = - \text{Im} [\int_{-\infty}^{\infty} dt \exp[-i\Delta\omega t] \int_{-\infty}^{\infty} dx \bar{E}_p^*(x + t) \bar{E}_p(x) |\bar{E}_L(x + \tau)|^2] . \quad (4-13)$$

By assuming the Gaussian profile for both the pump and the probe fields, *i.e.*,

$$\bar{E}_p(t) \propto \bar{E}_L(t) \propto \exp[-2(\frac{t}{\Delta t})^2] , \quad (4-14)$$

Eq. (4-13) is reduced to

$$\Delta S(\Delta\omega)_{[INC]} = \frac{1}{g} \Delta S(\Delta\omega)_{[COH]} = \exp[-\frac{1}{6} (\Delta\omega \Delta t)^2 - \frac{4}{3} (\frac{\tau}{\Delta t})^2] \cdot \sin(\frac{2}{3} \tau \cdot \Delta\omega) . \quad (4-15)$$

This explains the antisymmetric shape of the difference spectrum due to the spectral shift (*e.g.*, Fig. 4-31d' and g'), and also the oscillatory structure in the difference

spectra when the pump and the probe pulses are separated by more than pulse duration both in positive and in negative delays (e.g., Fig. 4-31a' and b'). At zero delay Eq. (4-15) predicts no change in the spectrum. This is because, although broadening of the spectrum is expected intuitively at zero delay, it is a higher-order phenomenon. In the limit of instantaneous response, such higher-order effect can be taken into account by considering the phase shift of the probe field following the pump intensity profile, as in the theoretical treatment of SPM described in Section 2.5. By including such a phase shift, the probe field is expressed as

$$E_p(t) = \tilde{E}_p(t) \exp [- i (\omega_p t - \varphi_2 \hat{I}(t + \tau))] , \quad (4-16)$$

where $\hat{I}(t)$ is the normalized pump intensity profile and φ_2 is the maximum phase shift. The probe spectrum $S'(\omega)$ can be calculated by Fourier-transforming the above equation:

$$S'(\omega) = | \mathcal{F} [E_p(t)] |^2 . \quad (4-17)$$

The result of the simulation of difference spectra is shown in Fig. 4-32a, in which the 60-fs (FWHM) Gaussian pulse at 620 nm was assumed for both pump and probe pulses and φ_2 was assumed to be 0.02. At zero delay there appears broadening of the probe spectrum but it is hardly seen in the figure because its magnitude is very weak. Moreover, since the experimental observation in Fig. 4-31f' shows narrowing of the spectrum rather than broadening around zero delay, it is necessary to take a chirp in the probe field into account for the better explanation of the observation. If the probe field is negatively chirped, *i.e.*, the blue component precedes the red component, the blue part undergoes, near zero delay, red shift at the leading edge of the pump pulse

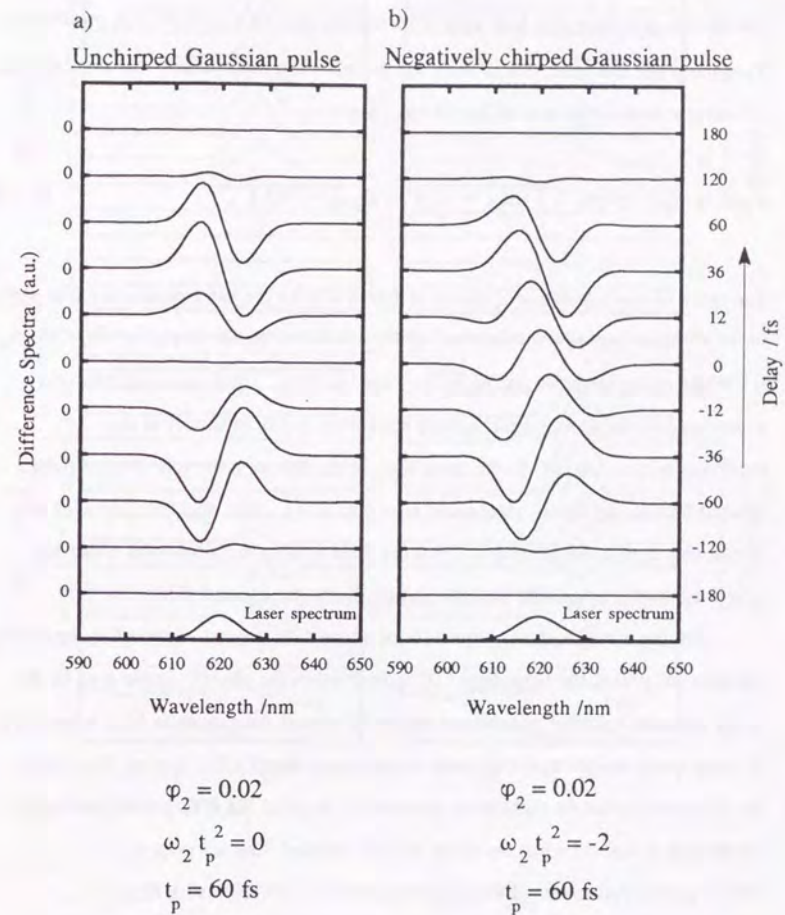


Figure 4-32 Calculation of difference spectra of chirped and unchirped pulses caused by induced phase modulation in a transparent medium

and the red part undergoes blue shift at the trailing edge in a medium with positive n_2 . Then the probe spectrum should show narrowing. This phenomenon was simulated by including a linear chirp term in Eq. (4-16), *i.e.*,

$$E_p(t) = \tilde{E}_p(t) \exp \left[-i \left(\omega_p t + \frac{\omega_2}{2} t^2 - \varphi_2 \hat{J}(t + \tau) \right) \right] . \quad (4-18)$$

The result of the calculation is shown in Fig. 4-32b for the same parameters that used in the above, except that the linear chirp term was assumed to be $\omega_2 t_p^2 = -2$, where t_p is FWHM of the temporal profile of the pulse intensity. There appeared relatively strong spectral narrowing signal around zero delay, which is similar to the experimental observation. In the same way, in the case of positively chirped pulses, spectral broadening signal is enhanced near zero delay. Such spectral narrowing or broadening signals due to chirp in the probe field arise as the third-order effect and have magnitude comparable with the signals due to the spectral shift.

On the other hand, in contrast to the above IPM process observed in the quartz and KBr substrates, the behavior of DTS observed in the phase I sample may be due to the coherent transient phenomena appearing around the excitation laser wavelength in pump-probe experiments explained by the theory described in Section 3.3. From the simulation based on this theory, asymmetric shape of the DTS around excitation wavelength is derived when the pump pulse is detuned from the peak of inhomogeneously broadened absorption spectrum [114]. By using Eqs. (3-7), (3-25a,b,c), (3-26), and (3-28), such a simulation was carried out as shown in Fig. 4-33, for the pump and probe pulses with the same Gaussian intensity profile (FWHM t_p). The energy (T_1) and phase (T_2) relaxation times were assumed to be $850 \cdot t_p$ and $0.85 \cdot t_p$, respectively. The laser frequency, ν_{Laser} , was assumed to be

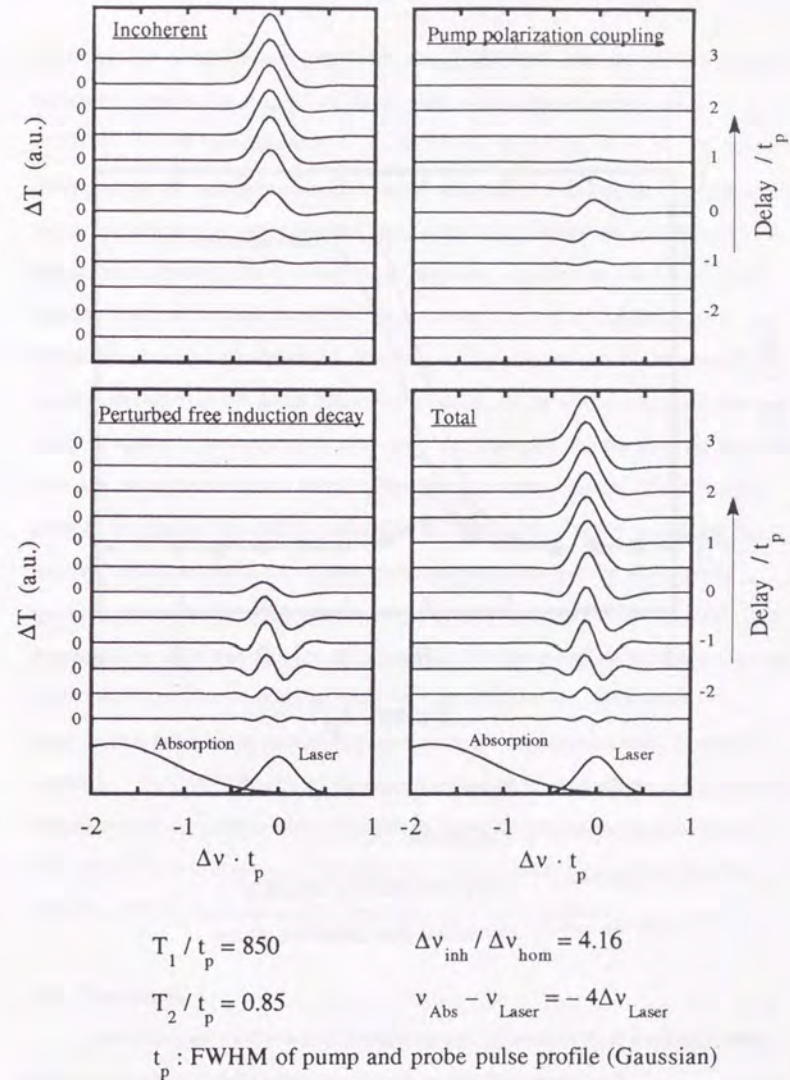


Figure 4-33 Calculation of spectra of transmittance change in an inhomogeneously broadened two-level system

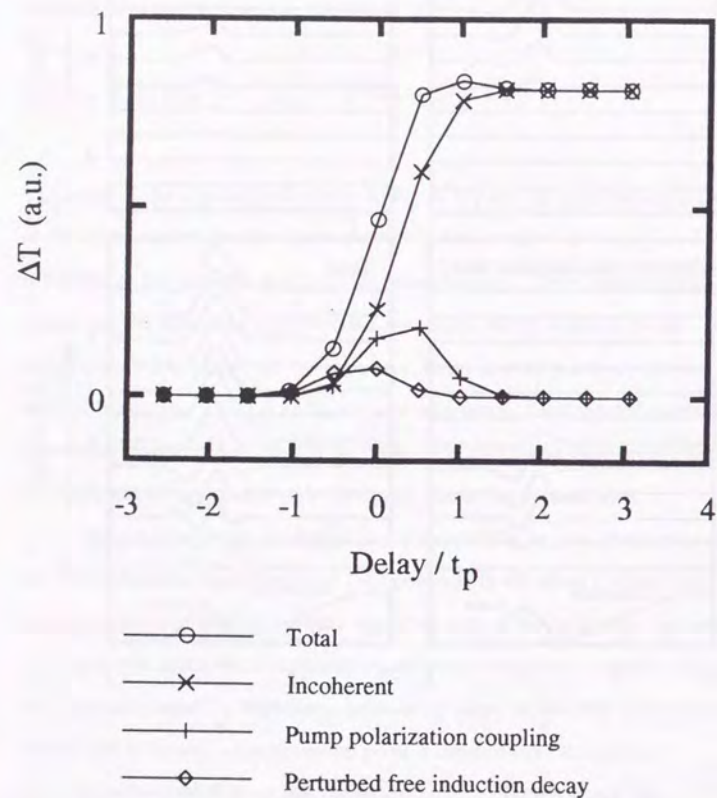


Figure 4-34 Calculation of transmittance change integrated over the whole probe-pulse spectrum as a function of time delay

higher by four times the laser bandwidth, $\Delta\nu_{\text{Laser}}$ (FWHM), than the inhomogeneously broadened transition at ν_{Abs} , in which the ratio of the inhomogeneous, $\Delta\nu_{\text{inh}}$ (FWHM), and the homogeneous, $\Delta\nu_{\text{hom}}$ (FWHM), linewidths was 4.16. At negative delays, where the oscillatory structure in the transmittance change spectrum is seen, the signal from the perturbed free induction decay term is dominant and the spectrum crosses zero near the central frequency of the laser. As the delay increases, zero-crossing frequency moves toward higher frequency and, at positive delays, the incoherent term becomes dominant. The frequency giving the maximum spectral hole signal is shifted from the pump frequency toward the center of the absorption line, which is similar to the experimental observation. However, the shape of the spectral hole does not change much at delays longer than the pulse duration. The difference between the observation and the simulation becomes much clear by comparing the temporal evolution of the transmittance change integrated over the whole probe spectrum, shown in Fig. 4-34, with the experimental result shown in Fig. 4-19. In the simulation the total transmission stays constant after the pump pulse duration, except for the slight peak at the delay t_p due to the coherent coupling terms, while the experiment resulted in the continuous increase in the transmission until 10 ps after excitation. Thus, the behavior of the DTS observed at negative delays is qualitatively consistent with the present model, but that at longer delays could not be explained well. Probably it is necessary to include the effect of the spectral cross-relaxation [108,171,172] for the more precise simulation of this observation.

4.6. Conclusions

Femtosecond time-resolved measurements of excited-state dynamics were reported for vanadyl phthalocyanines in various morphological forms.

In isolated molecules in solution and in a host polymer, 0.7-ps decay due to the thermalization process between tripdoublet (2T_1) and tripquartet (4T_1) states in monomers was observed. The process was preceded by extremely rapid relaxation from the first excited singdoublet (2Q) to tripdoublet (2T_1) taking place within the time resolution, *ca.* 60 fs, which is consistent with their low quantum yield of fluorescence reported previously [136]. The recovery of the ground-state population was very slow ($\gg 100$ ps) because of the high yield of the population of tripdoublet and tripquartet states.

In phase II films, a rapid intraband decay of excitons created at the high energy side of the Q band was observed, which took place within the time resolution. The excitons at the lowest-energy Q-band absorption peak relaxed via an exciton-exciton annihilation process due to the long-range dipole-dipole interaction. The rate of this bimolecular decay had time dependence, $t^{-1/2}$, and its coefficient γ' was estimated to be $4\text{--}6 \times 10^{-15} \text{ cm}^3 \text{ s}^{-1/2}$. From the value of γ' , the transition-dipole moment between excited states was estimated to be about 3 D, while that between the ground and the excited state is about 3.2 D. This value of γ' is more than one order of magnitude greater than that reported for $\beta\text{-H}_2\text{Pc}$ [141] probably because of the larger transition-dipole moment of excitons in phase II vanadyl phthalocyanines. In this molecular aggregate, the recovery time of the ground state is much faster than that in the isolated systems mainly because of the interaction between excitons. The decay kinetics was almost independent of temperature. It was also insensitive to the existence of the host polymer. This is consistent with that the molecules form aggregates in the host polymer with a local structure similar to that in bulk materials and the exciton decay is dominated by such a local environment. And also a *t*-butyl peripheral substituent did not affect the exciton decay kinetics.

In phase I films, two types of excitons, corresponding to the two peaks in the absorption spectrum, were created after excitation. The lower energy excitons relaxed faster than the higher energy ones. The initial picosecond relaxation of the lower energy excitons was interpreted as an exciton-exciton annihilation process via the long-range dipole-dipole interaction, which is the same mechanism as in phase II. The coefficient γ' of the time-dependent bimolecular decay rate was estimated to be $1.3 \times 10^{-15} \text{ cm}^3 \text{ s}^{-1/2}$. This leads the transition-dipole moment between excited states to about 0.8 D, which is smaller than that of phase II by a factor of about four, while that between the ground and the excited state is about 3.5 D. This difference is due to the different nature of the excitons in phases I and II, which is possibly related to their properties of photoconductivity and electroabsorption. On the other hand, the higher energy excitons created at 650 nm did not show bimolecular annihilation and relaxed more slowly with time constant of *ca.* 10 ps. Moreover, at early times within a few picoseconds, its population increased as a result of the annihilation of the lower energy excitons. The relaxation from the higher to the lower exciton level was found to be much slower than usual internal conversion processes.

In VOPc deposited on KBr, excitons created in the high energy region of Q band relaxed rapidly, within the time resolution, to the bottom of the band, as observed in phase II. However, in marked contrast to the above cases of phases I and II, it showed rapid monomolecular decay with time constant of 0.4 ps, which is probably due to the stronger exciton-lattice coupling in the more ordered crystal phase. The temperature dependence of the evolution of DTS, especially at times longer than 10 ps, still remains to be understood.

Finally, signals of DTS due to coherent interaction between pump and probe pulses were observed around the pump wavelength 620 nm, the magnitude of which was dependent on the samples. This behavior was followed by the broadening of the

spectral hole at the higher energy side of the Q band transition probably due to the spectral cross-relaxation, which took place with characteristic time constant of a few picoseconds. And also, in the quartz and alkali halide substrates, the spectral shift of the probe due to induced phase modulation was observed, which should be always, more or less, contained in DTS signal.

CHAPTER 5

CONCLUDING REMARKS

In this dissertation I have described construction and characterization of a femtosecond laser system, the experimental techniques and the theory of typical time-resolved measurements, *i.e.*, degenerate four-wave mixing and pump-probe measurements, and studies of excited-state dynamics in vanadyl phthalocyanines in several morphological forms by applying the above laser system and measurement techniques.

In the characterization of the laser system, it turned out that the combination of the dye laser and the amplifier is an important factor for the optimal pulse generation. An appropriate operation condition of the system was found by examining the dependence of the spectrum and the pulse duration on the intracavity dispersion of the dye laser. Femtosecond continuum was also characterized and found to have a frequency dependent temporal distribution caused not only by dispersion in optical elements but also by the generation process itself, which was explained by a simple model of self-phase modulation. Although extensive efforts were made to construct a laser system with better performance, there are several possible further improvements as described in Section 2.7., *i.e.*, achievement of higher gain of the amplifier, stabilization of the amplified pulses, achievement of more accurate data discrimination for the better signal to noise ratio, pulse compression, and wavelength tuning. After these improvements the present femtosecond laser system is expected to become much more reliable and flexible.

In the description of techniques of measurements, a simple but essential theory was described in terms of the third-order nonlinear polarization to figure out what is observed in these measurements. The importance of coherent processes at delays

less than pulse duration was pointed out and such phenomena were observed in pump-probe measurements in phthalocyanines, which was described in Subsection 4.5.5.

In the studies of excited-state dynamics in vanadyl phthalocyanines, relaxation mechanisms were revealed to be strongly dependent on the molecular environments. Four types of systems were investigated, *i.e.*, isolated molecules, phase I films, phase II films, and a thin film grown on a KBr substrate with a novel structure. Marked differences in the decay kinetics were observed among these systems. The dominant relaxation processes were the formation of tripdoublet and tripquartet states possessing lifetimes much longer than hundreds of picoseconds in the isolated molecules, the exciton-exciton annihilation taking place in the picosecond regime in phases I and II with different rate constants, and the subpicosecond monomolecular decay in VOPc on KBr. These behaviors are clearly due to the differences in interactions between these molecules. Because, unfortunately, the crystal structures and the origins of electronic transitions of these materials have not been fully understood yet, the relationship between arrangements of molecules and the dynamics of excitons created in the system remains to be clarified. However, it is important to notice that the same molecules can show markedly different behavior of the dynamics of the excited electronic states because of the differences in the intermolecular interactions. Although only one compound, vanadyl phthalocyanines, was investigated in the present study, such phenomena must be observed not only in other phthalocyanines but also in many other molecular compounds. The interpretation of the relaxation mechanism still contains several ambiguities. For the advanced step of the present study, selective excitation of excitons by utilizing a tunable laser source would help the better understanding.

The motivation of the present study was to know how different the dynamics of excited states of molecular systems with different molecular environments is. It was clarified that the relaxation mechanisms are strongly affected by the arrangement of molecules. This suggests the importance of the design of the molecular arrangement as well as the design of molecules for the extraction of proper functions from various compounds. Investigations of the relationship between various properties dependent on the molecular arrangement are expected to be significantly valuable for the design of functional molecular devices.

REFERENCES

1. R.L. Fork, C.H. Brito Cruz, P.C. Becker, and C.V. Shank, "Compression of optical pulses to six femtoseconds by using cubic phase compensation," *Opt. Lett.* **12**, 483-485 (1987).
2. For example, *Picosecond Phenomena* Vols. I-III (Springer-Verlag, Berlin, 1978, 1980, 1982); *Ultrafast Phenomena* Vols. IV-VII (Springer-Verlag, Berlin, 1984, 1986, 1988, 1990).
3. For example, *Nonlinear Optical Properties of Organic and Polymeric Materials*, ed. by D.J. Williams, ACS Symp. Series 233 (American Chemical Society, Washington, D.C., 1983); *Nonlinear Optics of Organics and Semiconductors*, ed. by T. Kobayashi, Springer Proc. in Physics **36** (Springer-Verlag, Berlin, 1989); *Advanced Organic Solid State Materials*, ed. by L.Y. Chiang, P.M. Chaikin, and D.D. Cowan, Mater. Res. Soc. Proc. **173** (Pittsburgh, PA, 1990); *Nonlinear Optical Properties of Organic Materials III*, ed. by G. Khanarian, Proc. SPIE **1337** (1990); *Organic Materials for Nonlinear Optics*, ed. by R.A. Hann and D. Bloor (Royal Soc. of Chem., London, 1989); *Organic Molecules for Nonlinear Optics and Photonics*, ed. by J. Messier *et al.*, NATO ASI Ser. E **194** (Kluwer Academic, Boston, 1991).
4. J.D. Simon, "Ultrashort light pulses," *Rev. Sci. Instrum.* **60**, 3597-3624 (1989), and references therein.
5. H.W. Mocker and R.J. Collins, "Mode competition and self-locking effects in a Q-switched ruby laser," *Appl. Phys. Lett.* **7**, 270-273 (1965).
6. E.B. Treacy, "Compression of picosecond light pulses," *Phys. Lett.* **28A**, 34-35 (1968).
7. M.J. Colles, "Ultrashort pulse formation in a short-pulse-stimulated Raman oscillator," *Appl. Phys. Lett.* **19**, 23-25 (1971).
8. A. Penzkofer, D. von der Linde, A. Laubereau, and W. Kaiser, "Generation of single picosecond and subpicosecond light pulses," *Appl. Phys. Lett.* **20**, 351-354 (1972).
9. C.V. Shank and E.P. Ippen, "Subpicosecond kilowatt pulses from a mode-locked cw dye laser," *Appl. Phys. Lett.* **24**, 373-375 (1974).
10. R.L. Fork, B.I. Greene, and C.V. Shank, "Generation of optical pulses shorter than 0.1 psec by colliding pulse mode locking," *Appl. Phys. Lett.* **38**, 671-672 (1981).
11. W. Dietel, J.J. Fontaine, and J.-C. Diels, "Intracavity pulse compression with glass: a new method of generating pulses shorter than 60 fsec," *Opt. Lett.* **8**, 4-6 (1983).
12. O.E. Martinez, R.L. Fork, and J.P. Gordon, "Theory of passively mode-locked lasers including self-phase modulation and group-velocity dispersion," *Opt. Lett.* **9**, 156-158 (1984).
13. S. De Silvestri, P. Laporta, and O. Svelto, "The role of cavity dispersion in cw mode-locked lasers," *IEEE J. Quantum Electron.* **QE-20**, 533-539 (1984).
14. E.B. Treacy, "Optical pulse compression with diffraction gratings," *IEEE J. Quantum Electron.* **QE-5**, 454-458 (1969).
15. R.L. Fork, O.E. Martinez, and J.P. Gordon, "Negative dispersion using pairs of prisms," *Opt. Lett.* **9**, 150-152 (1984).
16. J.P. Gordon and R.L. Fork, "Optical resonator with negative dispersion," *Opt. Lett.* **9**, 153-155 (1984).
17. F. Gires and P. Tournois, "Interféromètre utilisable pour la compression d'impulsions lumineuses modulées en fréquence," *C. R. Acad. Sc. Paris* **258**, 6112-6115 (1964).
18. J. Heppner and J. Kuhl, "Intracavity chirp compensation in a colliding pulse mode-locked laser using thin-film interferometers," *Appl. Phys. Lett.* **47**, 453-455 (1985).
19. J.A. Valdmanis, R.L. Fork, and J.P. Gordon, "Generation of optical pulses as short as 27 femtoseconds directly from a laser balancing self-phase modulation, group-velocity dispersion, saturable absorption, and saturable gain," *Opt. Lett.* **10**, 131-133 (1985).
20. J.A. Valdmanis and R.L. Fork, "Design considerations for a femtosecond pulse laser balancing self phase modulation, group velocity dispersion, saturable absorption, and saturable gain," *IEEE J. Quantum Electron.* **QE-22**, 112-118 (1986).
21. M.R.X. de Barros, R.S. Miranda, and C.H. Brito Cruz, "Third-order group-velocity dispersion in a colliding-pulse mode-locked dye laser," *Opt. Lett.* **15**, 127-129 (1990).
22. M. Yamashita, M. Ishikawa, K. Torizuka, and T. Sato, "Femtosecond-pulse laser chirp compensated by cavity-mirror dispersion," *Opt. Lett.* **11**, 504-506 (1986).
23. M. Yamashita, K. Torizuka, and T. Sato, "A chirp-compensation technique using incident-angle changes of cavity mirrors in a femtosecond pulse laser," *IEEE J. Quantum Electron.* **QE-23**, 2005-2007 (1987).

24. M. Yamashita, S. Kaga, and K. Torizuka, "Chirp-compensation cavity-mirrors with minimal third-order dispersion for use in a femtosecond pulse laser," *Opt. Commun.* **76**, 363-368 (1990).
25. H. Goto, K. Ueda, S. Hashiguchi, and Y. Kawano, "Generation of the range of 20 to 30 fs light pulses by third-order phase dispersion compensation," presented in the spring meeting of the Japan Society of Applied Physics (Saitama, 1990), paper 30p-G-10.
26. H. Kubota, K. Kurokawa, and M. Nakazawa, "29-fsec pulse generation from a linear-cavity synchronously pumped dye laser," *Opt. Lett.* **13**, 749-751 (1988).
27. A.E. Siegman, "An antiresonant ring interferometer for coupled laser cavities, laser output coupling, mode locking, and cavity dumping," *IEEE J. Quantum Electron.* **QE-9**, 247-250 (1973).
28. H. Vanherzeele, R. Torti, and J.-C. Diels, "Synchronously pumped dye laser passively mode-locked with an antiresonant ring," *Appl. Opt.* **23**, 4182-4184 (1984).
29. T. Norris, T. Sizer II, and G. Mourou, "Generation of 85-fsec pulses by synchronous pumping of a colliding-pulse mode-locked dye laser," *J. Opt. Soc. Am. B* **2**, 613-615 (1985).
30. J. Chesnoy and L. Fini, "Stabilization of a femtosecond dye laser synchronously pumped by a frequency-doubled mode-locked YAG laser," *Opt. Lett.* **11**, 635-637 (1986).
31. S. Ruhman, A.G. Joly, B. Kohler, L.R. Williams, and K.A. Nelson, "Intramolecular and intermolecular dynamics in molecular liquids through femtosecond time-resolved impulsive stimulated scattering," *Rev. Phys. Appl.* **22**, 1717-1734 (1987).
32. W.T. Lotshaw, D. McMorrow, T. Dickson, and G.A. Kenney-Wallace, "Synchronously pumped, femtosecond dye laser insensitive to cavity-length variation of up to 15 μm ," *Opt. Lett.* **14**, 1195-1197 (1989).
33. N. Jamasbi, J.-C. Diels, and L. Sarger, "Study of a linear femtosecond laser in passive and hybrid operation," *J. Mod. Opt.* **35**, 1891-1906 (1988).
34. M.D. Dawson, D. Maxson, T.F. Boggess, and A.L. Smirl, "Cavity-length detuning effects and stabilization of a synchronously pumped femtosecond linear dye laser," *Opt. Lett.* **13**, 126-128 (1988).
35. W.H. Knox, "Femtosecond optical pulse amplification," *IEEE J. Quantum Electron.* **QE-24**, 388-397 (1988).

36. R.L. Fork, C.V. Shank, and R.T. Yen, "Amplification of 70-fs optical pulses to gigawatt powers," *Appl. Phys. Lett.* **41**, 223-225 (1982).
37. W.M. Wood, G. Focht, and M.C. Downer, "Tight focusing and blue shifting of millijoule femtosecond pulses from a conical axicon amplifier," *Opt. Lett.* **13**, 984-986 (1988).
38. W.H. Knox, M.C. Downer, R.L. Fork, and C.V. Shank, "Amplified femtosecond optical pulses and continuum generation at 5-kHz repetition rate," *Opt. Lett.* **9**, 552-554 (1984).
39. E.V. Khoroshilov, I.V. Kryukov, P.G. Kryukov, and A.V. Sharkov, "10 kHz-rate amplification of 40-fs optical pulses at low pumping energy," in *Ultrafast Phenomena VI*, ed. by T. Yajima, K. Yoshihara, C.B. Harris, and S. Shionoya, Springer Series in Chemical Physics **48** (Springer-Verlag, Berlin, 1988), pp. 22-23.
40. D. Nickel, D. Kühlke, and D. von der Linde, "Multipass dye-cell amplifier for high-repetition-rate femtosecond optical pulses," *Opt. Lett.* **14**, 36-38 (1989).
41. D.C. Rodenberger, C.H. Grossman, and A.F. Garito, "Low-dispersion, high-gain femtosecond optical pulse amplifier," *Opt. Lett.* **15**, 498-500 (1990).
42. C. Rolland and P.B. Corkum, "Amplification of 70 fs pulses in a high repetition rate XeCl pumped dye laser amplifier," *Opt. Commun.* **59**, 64-68 (1986).
43. T. Turner, M. Chatelet, D.S. Moore, and S.C. Schmidt, "Large-gain amplifier for subpicosecond optical pulses," *Opt. Lett.* **11**, 357-359 (1986).
44. P.C. Becker, H.L. Fragnito, R.L. Fork, F.A. Beisser, and C.V. Shank, "Generation of tunable 9 femtosecond optical pulses in the near infrared," *Appl. Phys. Lett.* **54**, 411-412 (1989).
45. I.N. Duling III, T. Norris, T. Sizer II, P. Bado, and G.A. Mourou, "Kilohertz synchronous amplification of 85-femtosecond optical pulses," *J. Opt. Soc. Am. B* **2**, 616-618 (1985).
46. V.J. Newell, F.W. Deeg, S.R. Greenfield, and M.D. Fayer, "Tunable subpicosecond dye laser amplified at 1 kHz by a cavity-dumped, Q-switched, and mode-locked Nd:YAG laser," *J. Opt. Soc. Am. B* **6**, 257-263 (1989).
47. A. Chébir and J. Chesnoy, "Amplification of a femtosecond laser at eight kilohertz with a continuously pumped YAG laser," *Opt. Commun.* **76**, 235-238 (1990).
48. R.L. Fork, C.V. Shank, C. Hirlimann, R. Yen, and W.J. Tomlinson, "Femtosecond white-light continuum pulses," *Opt. Lett.* **8**, 1-3 (1983).

49. C.V. Shank, R.L. Fork, R. Yen, R.H. Stolen, and W.J. Tomlinson, "Compression of femtosecond optical pulses," *Appl. Phys. Lett.* **40**, 761-763 (1982).
50. W.J. Tomlinson, R.H. Stolen, and C.V. Shank, "Compression of optical pulses chirped by self-phase modulation," *J. Opt. Soc. Am. B* **1**, 139-149 (1984).
51. J.G. Fujimoto, A.M. Weiner, and E.P. Ippen, "Generation and measurement of optical pulses as short as 16 fs," *Appl. Phys. Lett.* **44**, 832-834 (1984).
52. J.-M. Halbout and D. Grischkowsky, "12-fs ultrashort optical pulse compression at high repetition rate," *Appl. Phys. Lett.* **45**, 1281-1283 (1984).
53. W.H. Knox, R.L. Fork, M.C. Downer, R.H. Stolen, C.V. Shank, and J.A. Valdmanis, "Optical pulse compression to 8 fs at a 5-kHz repetition rate," *Appl. Phys. Lett.* **46**, 1120-1121 (1985).
54. W.H. Knox, "Generation and kilohertz-rate amplification of femtosecond optical pulses around 800 nm," *J. Opt. Soc. Am. B* **4**, 1771-1776 (1987).
55. P.M.W. French and J.R. Taylor, "Generation of sub-100-fsec pulses tunable near 497 nm from a colliding-pulse mode-locked ring dye laser," *Opt. Lett.* **13**, 470-472 (1988).
56. P.M.W. French, M.M. Opalinska, and J.R. Taylor, "Passively mode-locked cw Coumarin 6 ring dye laser," *Opt. Lett.* **14**, 217-218 (1989).
57. P. Georges, F. Salin, and A. Brun, "Generation of 36-fsec pulses near 775 nm from a colliding-pulse passively mode-locked dye laser," *Opt. Lett.* **14**, 940-942 (1989).
58. P. Georges, F. Salin, G. Le Saux, G. Roger, and A. Brun, "58 fs pulse generation near 685 nm from a passively mode locked dye laser," *Opt. Commun.* **69**, 281-284 (1989).
59. J. Comly and E. Garmire, "Second harmonic generation from short pulses," *Appl. Phys. Lett.* **12**, 7-9 (1968).
60. D.C. Edelstein, E.S. Wachman, L.K. Cheng, W.R. Bosenberg, and C.L. Tang, "Femtosecond ultraviolet pulse generation in β -BaB₂O₄," *Appl. Phys. Lett.* **52**, 2211-2213 (1988).
61. G. Szabó and Z. Bor, "Broadband frequency doubler for femtosecond pulses," *Appl. Phys. B* **50**, 51-54 (1990).
62. O.E. Martínez, "Achromatic phase matching for second harmonic generation of femtosecond pulses," *IEEE J. Quantum Electron.* **QE-25**, 2464-2468 (1989).
63. J.H. Glowina, J. Misewich, and P.P. Sorokin, "160-fs XeCl excimer amplifier system," *J. Opt. Soc. Am. B* **4**, 1061-1065 (1987).

64. S. Szatmári and F.P. Schäfer, "Simplified laser system for the generation of 60 fs pulses at 248 nm," *Opt. Commun.* **68**, 196-202 (1988).
65. M. Watanabe, A. Endoh, N. Sarukura, and S. Watanabe, "Subpicosecond UV pulse generation for a multiterawatt KrF laser," *Appl. Phys. B* **48**, 417-420 (1989).
66. A.J. Taylor, C.R. Tallman, J.P. Roberts, C.S. Lester, T.R. Gosnell, P.H.Y. Lee, and G.A. Kyrala, "High-intensity subpicosecond XeCl laser system," *Opt. Lett.* **15**, 39-41 (1990).
67. D.S. Moore and S.C. Schmidt, "Tunable subpicosecond infrared pulse generation to 4 μ m," *Opt. Lett.* **12**, 480-482 (1987).
68. K. Kurokawa and M. Nakazawa, "Femtosecond 1.4-1.6 μ m infrared pulse generation at a high repetition rate by difference frequency generation," *Appl. Phys. Lett.* **55**, 7-9 (1989).
69. T.M. Jedju and L. Rothberg, "Tunable femtosecond radiation in the mid-infrared for time-resolved absorption in semiconductors," *Appl. Opt.* **27**, 615-618 (1988).
70. D.C. Edelstein, E.S. Wachman, and C.L. Tang, "Broadly tunable high repetition rate femtosecond optical parametric oscillator," *Appl. Phys. Lett.* **54**, 1728-1730 (1989).
71. E.S. Wachman, D.C. Edelstein, and C.L. Tang, "Continuous-wave mode-locked and dispersion-compensated femtosecond optical parametric oscillator," *Opt. Lett.* **15**, 136-138 (1990).
72. J.H. Glowina, J. Misewich, and P.P. Sorokin, "Subpicosecond time-resolved infrared spectral photography," *Opt. Lett.* **12**, 19-21 (1987).
73. A. Migus, A. Antonetti, J. Etchepare, D. Hulin, and A. Orszag, "Femtosecond spectroscopy with high-power tunable optical pulses," *J. Opt. Soc. Am. B* **2**, 584-594 (1985).
74. J.P. Chambaret, A. Dos Santos, G. Hamoniaux, A. Migus, and A. Antonetti, "Generation of megawatt tunable pulses of duration 90 fs at 11 kHz repetition rate: first experiments in the range 800-850 nm," *Opt. Commun.* **69**, 401-404 (1989).
75. I. Ledoux, J. Badan, J. Zyss, A. Migus, D. Hulin, J. Etchepare, G. Grillon, and A. Antonetti, "Generation of high-peak-power tunable infrared femtosecond pulses in an organic crystal: application to time resolution of weak infrared signals," *J. Opt. Soc. Am. B* **4**, 987-997 (1987).
76. J. Hebling and J. Kuhl, "Generation of femtosecond pulses by traveling-wave amplified spontaneous emission," *Opt. Lett.* **14**, 278-280 (1989).

77. J. Hebling and J. Kuhl, "Generation of tunable femtosecond pulses by traveling wave amplification," *Opt. Commun.* **73**, 375-379 (1989).
78. J. Klebniczki, J. Hebling, and J. Kuhl, "Generation of tunable femtosecond pulses in a traveling-wave amplifier," *Opt. Lett.* **15**, 1368-1370 (1990).
79. P. Moulton, "Ti-doped sapphire: a tunable solid-state laser," *Opt. News* **8**, 9 (1982).
80. D.E. Spence, P.N. Kean, and W. Sibbett, "60-fsec pulse generation from a self-mode-locked Ti:sapphire laser," *Opt. Lett.* **16**, 42-44 (1991).
81. Recent progress is presented by several groups in *Quantum Electronics Laser Science*, (Baltimore, 1991).
82. For example, C.V. Shank, "Generation of ultrashort optical pulses," in *Ultrashort Laser Pulses and Applications*, ed. by W. Kaiser, Topics in Applied Physics **60** (Springer-Verlag, Berlin, 1988), pp. 5-34.
83. E.M. Garmire and A. Yariv, "Laser mode-locking with saturable absorbers," *IEEE J. Quantum Electron.* **QE-3**, 222-226 (1967); *ibid.* **QE-3**, 377 (1967).
84. H.A. Haus, "Theory of mode locking with a slow saturable absorber," *IEEE J. Quantum Electron.* **QE-11**, 736-746 (1975).
85. H.A. Haus, "Theory of mode locking with a fast saturable absorber," *J. Appl. Phys.* **46**, 3049-3058 (1975).
86. A. Penzkofer, "Passive Q-switching and mode-locking for the generation of nanosecond to femtosecond pulses," *Appl. Phys. B* **46**, 43-60 (1988).
87. J. Mark, L.Y. Liu, K.L. Hall, H.A. Haus, and E.P. Ippen, "Femtosecond pulse generation in a laser with a nonlinear external resonator," *Opt. Lett.* **14**, 48-50 (1989).
88. E.P. Ippen, H.A. Haus, and L.Y. Liu, "Additive pulse mode locking," *J. Opt. Soc. Am. B* **6**, 1736-1745 (1989).
89. M.S. Stix and E.P. Ippen, "Pulse shaping in passively mode-locked ring dye lasers," *IEEE J. Quantum Electron.* **QE-19**, 520-525 (1983).
90. M. Yoshizawa and T. Kobayashi, "Experimental and theoretical studies on colliding pulse mode locking," *IEEE J. Quantum Electron.* **QE-20**, 797-803 (1984).
91. K. Naganuma, K. Mogi, and H. Yamada, "General method for ultrashort light pulse chirp measurement," *IEEE J. Quantum Electron.* **QE-25**, 1225-1233 (1989).
92. R.E. Grove, "Copper vapor lasers come of age," *Laser Focus*, 45-50 (1982).
93. D.B. McDonald and C.D. Jonah, "Amplification of picosecond pulses using a copper vapor laser," *Rev. Sci. Instrum.* **55**, 1166-1168 (1984).

94. J.B. Hopkins and P.M. Rentzepis, "Picosecond pulse amplification using a copper vapor laser," *Appl. Phys. Lett.* **47**, 776-778 (1985).
95. K.H. Drexhage, "Structure and properties of laser dyes," in *Dye Lasers*, ed. by F.P. Schäfer, Topics in Applied Physics **1** (Springer-Verlag, Berlin, 1973), pp. 144-193.
96. Recently the gain dye concentration twice as high as before, *i.e.*, ca. 6×10^{-4} mol/l in 20-vol% aqueous solution of Ammonyx LO, could amplify the dye laser pulse to more than 3 μ J with 0.5-mJ CVL pump. ASE was suppressed to less than 1% in energy by inserting another aperture between the fourth pass and the saturable absorber.
97. R.L. Fork, F.A. Beisser, and D.K. Fork, "Multipass optical amplifier using a double confocal resonator geometry," *Rev. Phys. Appl.* **22**, 1665-1671 (1987).
98. R.L. Fork, H. Avramopoulos, H.L. Fragnito, P.C. Becker, K.L. Scheerer, and C. Hirlimann, "Amplification of femtosecond optical pulses using a double confocal resonator," *Opt. Lett.* **14**, 1068-1070 (1989).
99. D.C. Rodenberger, private communication.
100. R.R. Alfano and S.L. Shapiro, "Emission in the region 4000 to 7000 Å via four-photon coupling in glass," *Phys. Rev. Lett.* **24**, 584-587 (1970).
101. R.R. Alfano, L.L. Hope, and S.L. Shapiro, "Electronic mechanism for production of self-phase modulation," *Phys. Rev. A* **6**, 433-438 (1972).
102. Q.X. Li, T. Jimbo, P.P. Ho, and R.R. Alfano, "Temporal distribution of picosecond super-continuum generated in a liquid measured by a streak camera," *Appl. Opt.* **25**, 1869-1871 (1986).
103. P.L. Baldeck, P.P. Ho, and R.R. Alfano, "Effects of self, induced and cross phase modulations on the generation of picosecond and femtosecond white light supercontinua," *Rev. Phys. Appl.* **22**, 1677-1694 (1987).
104. R.R. Alfano and P.P. Ho, "Self-, cross-, and induced-phase modulations of ultrashort laser pulse propagation," *IEEE J. Quantum Electron.* **QE-24**, 351-364 (1988).
105. T. Hattori, A. Terasaki, T. Kobayashi, T. Wada, A. Yamada, and H. Sasabe, "Optical-heterodyne-detected induced phase modulation for the study of femtosecond molecular dynamics," *J. Chem. Phys.* **95**, 937-945 (1991).
106. C.H. Brito Cruz, R.L. Fork, W.H. Knox, and C.V. Shank, "Spectral hole burning in large molecules probed with 10 fs optical pulses," *Chem. Phys. Lett.* **132**, 341-344 (1986).

107. A.M. Weiner and E.P. Ippen, "Novel transient scattering technique for femtosecond dephasing measurements," *Opt. Lett.* **9**, 53-55 (1984).
108. A.M. Weiner, S. De Silvestri, and E.P. Ippen, "Three-pulse scattering for femtosecond dephasing studies: theory and experiment," *J. Opt. Soc. Am. B* **2**, 654-661 (1985).
109. N. Morita and T. Yajima, "Ultra-high-time-resolution coherent transient spectroscopy with incoherent light," *Phys. Rev. A* **30**, 2525-2536 (1984).
110. S. Asaka, H. Nakatsuka, M. Fujiwara, and M. Matsuoka, "Accumulated photon echoes with incoherent light in Nd³⁺-doped silicate glass," *Phys. Rev. A* **29**, 2286-2289 (1984).
111. R. Beach and S.R. Hartmann, "Incoherent photon echoes," *Phys. Rev. Lett.* **53**, 663-666 (1984).
112. N. Morita, T. Tokizaki, and T. Yajima, "Time-delayed four-wave mixing using incoherent light for observation of ultrafast population relaxation," *J. Opt. Soc. Am. B* **4**, 1269-1275 (1987).
113. T. Kobayashi, A. Terasaki, T. Hattori, and K. Kurokawa, "The application of incoherent light for the study of femtosecond-picosecond relaxation in condensed phase," *Appl. Phys. B* **47**, 107-125 (1988).
114. C.H. Brito Cruz, J.P. Gordon, P.C. Becker, R.L. Fork, and C.V. Shank, "Dynamics of spectral hole burning," *IEEE J. Quantum Electron.* **QE-24**, 261-266 (1988).
115. B. Fluegel, N. Peyghambarian, G. Olbright, M. Lindberg, S.W. Koch, M. Joffre, D. Hulin, A. Migus, and A. Antonetti, "Femtosecond studies of coherent transients in semiconductors," *Phys. Rev. Lett.* **59**, 2588-2591 (1987).
116. M. Lindberg and S.W. Koch, "Theory of coherent transients in semiconductor pump-probe spectroscopy," *J. Opt. Soc. Am. B* **5**, 139-146 (1988).
117. M. Joffre, D. Hulin, A. Migus, A. Antonetti, C. Benoit à la Guillaume, N. Peyghambarian, M. Lindberg, and S.W. Koch, "Coherent effects in pump-probe spectroscopy of excitons," *Opt. Lett.* **4**, 276-278 (1988).
118. J.P. Sokoloff, M. Joffre, B. Fluegel, D. Hulin, M. Lindberg, S.W. Koch, A. Migus, A. Antonetti, and N. Peyghambarian, "Transient oscillations in the vicinity of excitons and in the band of semiconductors," *Phys. Rev. B* **38**, 7615-7621 (1988).
119. S.W. Koch, N. Peyghambarian, and M. Lindberg, "Transient and steady-state optical non-linearities in semiconductors," *J. Phys. C* **21**, 5229-5249 (1988).
120. M. Joffre, D. Hulin, A. Migus, and A. Antonetti, "Dynamics of the optical Stark effect in semiconductors," *J. Mod. Opt.* **35**, 1951-1964 (1988).

121. M. Joffre, D. Hulin, J.-P. Foing, J.-P. Chambaret, A. Migus, and A. Antonetti, "Dynamics and Fourier transform studies of the excitonic optical Stark effect," *IEEE J. Quantum Electron.* **QE-25**, 2505-2515 (1989).
122. Z.Z. Ho, C.Y. Ju, and W.M. Hetherington III, "Third harmonic generation in phthalocyanines," *J. Appl. Phys.* **62**, 716-718 (1987).
123. T. Wada, Y. Matsuoka, K. Shigehara, A. Yamada, A.F. Garito, and H. Sasabe, "Organic nonlinear thin film: phthalocyanine derivatives," in *Photoresponsive Materials* (Materials Research Society, Pittsburgh, 1989) Proc. MRS Int. Meeting on Advd. Mat. **12**, pp. 75-80.
124. T. Wada, S. Yamada, Y. Matsuoka, C.H. Grossman, K. Shigehara, H. Sasabe, A. Yamada, and A.F. Garito, "Frontier materials for organic nonlinear optics," in *Nonlinear Optics of Organics and Semiconductors*, ed. by T. Kobayashi, Springer Proc. in Physics **36** (Springer-Verlag, Berlin, 1989) pp. 292-300.
125. T. Wada, J. Ojima, A. Yamada, A.F. Garito, and H. Sasabe, "Optical third harmonic measurements of macrocyclic conjugated chains," *Proc. SPIE* **1147**, 286-291 (1989).
126. J.W. Wu, J.R. Heflin, R.A. Norwood, K.Y. Wong, O. Zamani-Khamiri, A.F. Garito, P. Kalyanaraman, and J. Sounik, "Nonlinear-optical processes in lower-dimensional conjugated structures," *J. Opt. Soc. Am. B* **6**, 707-720 (1989).
127. J.S. Shirk, J.R. Lindle, F.J. Bartoli, C.A. Hoffman, Z.H. Kafafi, and A.W. Snow, "Off-resonant third-order optical nonlinearities of metal-substituted phthalocyanines," *Appl. Phys. Lett.* **55**, 1287-1288 (1989).
128. H. Sasabe, T. Wada, M. Hosoda, H. Ohkawa, A. Yamada, and A.F. Garito, "Molecular design of conjugated systems for nonlinear optics," *Mol. Cryst. Liq. Cryst.* **189**, 155-168 (1990).
129. M. Hosoda, T. Wada, A. Yamada, A.F. Garito, and H. Sasabe, "Enhancements in third-order optical properties of phthalocyanine thin films," *Proc. SPIE* **1337**, 99-104 (1990).
130. M. Hosoda, T. Wada, A. Yamada, A.F. Garito, and H. Sasabe, "Phases and third-order optical nonlinearities in tetravalent metallophthalocyanine thin films," *Jpn. J. Appl. Phys.* **30**, L1486-L1488 (1991).
131. M. Hosoda, T. Wada, A. Yamada, A.F. Garito, and H. Sasabe, "Third-order nonlinear optical properties in soluble phthalocyanines with *tert*-butyl substituents," *Jpn. J. Appl. Phys.* **30**, 1715-1719 (1991).

132. For example, M.J. Stillman and T. Nyokong, "Absorption and magnetic circular dichroism spectral properties of phthalocyanines Part I: Complexes of the dianion Pc(-2)," in *Phthalocyanines: Properties and Applications*, ed. by C.C. Leznoff and A.B.P. Lever (VCH Publishers, New York, 1989) pp. 133-290; M. Gouterman, "Optical spectra and electronic structure of porphyrins and related rings," in *The Porphyrins*. Vol. III, Part A. *Physical Chemistry*, ed. by D. Dolphin (Academic Press, New York, 1978) pp. 1-165.
133. L.K. Lee, N.H. Sabelli, and P.R. LeBreton, "Theoretical characterization of phthalocyanine, tetraazaporphyrin, tetrabenzoporphyrin, and porphyrin electronic spectra," *J. Phys. Chem.* **86**, 3926-3931 (1982).
134. C.H. Griffiths, M.S. Walker, and P. Goldstein, "Polymorphism in vanadyl phthalocyanine," *Mol. Cryst. Liq. Cryst.* **33**, 149-170 (1976).
135. R.F. Ziolo, C.H. Griffiths, and J.M. Troup, "Crystal structure of vanadyl phthalocyanine, phase II," *J. Chem. Soc., Dalton Trans.*, 2300-2302 (1980).
136. T.-H. Huang and J.H. Sharp, "Electronic transitions of vanadyl phthalocyanine in solution and in the solid state," *Chem. Phys.* **65**, 205-216 (1982).
137. Sh.Sh. Bashkurov, L.S. Volkova, and V.V. Parfenov, "Feature of exciton electroabsorption in vanadyl and hydroxygallium phthalocyanines," *Opt. Spectrosc.* **42**, 326-327 (1977).
138. T.-H. Huang, "Electroabsorption spectra of the vanadyl phthalocyanine films," *J. Phys. Soc. Jpn.* **56**, 1213-1222 (1987).
139. K.-Y. Law, "Effect of dye aggregation on the photogeneration efficiency of organic photoconductors," *J. Phys. Chem.* **92**, 4226-4231 (1988).
140. T.D. Sims, J.E. Pemberton, P. Lee, and N.R. Armstrong, "Comparison of supramolecular aggregate structure and spectroscopic and photoelectrochemical properties of tetravalent and trivalent metal phthalocyanine thin films," *Chem. Mater.* **1**, 26-34 (1989).
141. B.I. Greene and R.R. Millard, "Subpicosecond spectroscopic studies of singlet exciton fusion in molecular solids," *J. Phys., Colloq.* **46**, C7-371-376 (1985); "Singlet-exciton fusion in molecular solids: A direct subpicosecond determination of time-dependent annihilation rates," *Phys. Rev. Lett.* **55**, 1331-1334 (1985).
142. Z.Z. Ho and N. Peyghambarian, "Femtosecond dynamics in organic thin films of fluoro-aluminium phthalocyanine," *Chem. Phys. Lett.* **148**, 107-111 (1988).

143. M.K. Casstevens, M. Samoc, J. Pflieger, and P.N. Prasad, "Dynamics of third-order nonlinear optical processes in Langmuir-Blodgett and evaporated films of phthalocyanine," *J. Chem. Phys.* **92**, 2019-2024 (1990).
144. D. Neher, A. Kaltbeitzel, A. Wolf, C. Bubeck, and G. Wegner, "Nonlinear optical properties of ultrathin polymer films," in *Conjugated Polymeric Materials: Opportunities in Electronics, Optoelectronics, and Molecular Electronics*, ed. by J.L. Brédas and R.R. Chance (Kluwer Academic, Dordrecht, 1990) pp. 387-398.
145. V.S. Williams, J.P. Sokoloff, Z.Z. Ho, C. Arbour, N.R. Armstrong, and N. Peyghambarian, "Observation of polarization-dependent spectral holes in an organic thin film," in *Technical Digest Series Vol. 11, Quantum Electronics Laser Science*, (Baltimore, 1991), paper QThA7.
146. K.-Y. Law, "An investigation of solvent-vapor-induced crystallization of soluble vanadyl phthalocyanine dyes in a polymer matrix," *J. Phys. Chem.* **89**, 2652-2657 (1985).
147. H. Tada, K. Saiki, and A. Koma, "Preparation and characterization of vanadyl-phthalocyanine ultrathin films grown on KBr and KCl by molecular beam epitaxy," *Jpn. J. Appl. Phys.* **30**, L306-L308 (1991).
148. M. Hara, H. Sasabe, A. Yamada, and A.F. Garito, "Epitaxial growth of organic thin films by organic molecular beam epitaxy," *Jpn. J. Appl. Phys.* **28**, L306-L308 (1989).
149. A.J. Dann, H. Hoshi, and Y. Maruyama, "The structure and properties of phthalocyanine films grown by the molecular beam epitaxy technique. I. Preparation and characterization," *J. Appl. Phys.* **67**, 1371-1379 (1990).
150. H. Hoshi, A.J. Dann, and Y. Maruyama, "The structure and properties of phthalocyanine films grown by the molecular beam epitaxy technique. II. Ultraviolet/visible spectroscopic study," *J. Appl. Phys.* **67**, 1845-1849 (1990).
151. H. Hoshi, A.J. Dann, and Y. Maruyama, "The structure and properties of phthalocyanine films grown by the molecular beam epitaxy technique. III. Preparation and characterization of lutetium diphthalocyanine films," *J. Appl. Phys.* **67**, 6871-6875 (1990).
152. H. Hoshi, Y. Maruyama, H. Masuda, and T. Inabe, "A new type of epitaxial growth in lithium phthalocyanine film on KBr (100) prepared by the molecular-beam epitaxy," *J. Appl. Phys.* **68**, 1396-1398 (1990).
153. R.L. Ake and M. Gouterman, "Porphyrins XIV. Theory for the luminescent state in VO, Co, Cu complexes," *Theoret. Chim. Acta* **15**, 20-42 (1969).

154. M. Kasha, H.R. Rawls, and M.A. El-Bayoumi, "The exciton model in molecular spectroscopy," *Pure and Appl. Chem.* **11**, 371-392 (1965).
155. N.S. Hush and I.S. Woolsey, "The electronic absorption spectra of phthalocyanine monomers and dimers," *Mol. Phys.* **21**, 465-474 (1971).
156. M. Morita, "Charge-transfer like structures of stannic-phthalocyanine," *J. Phys. Soc. Jpn.* **33**, 863 (1972).
157. A.T. Vartanyan and A.N. Sidorov, "Spectral properties of Pb phthalocyanine layers," *Russ. J. Phys. Chem.* **59**, 1319-1321 (1985).
158. Y. Tokura, T. Koda, Y. Iyechika, and H. Kuroda, "Electro-reflectance spectra of charge-transfer excitations in copper phthalocyanine single crystals," *Chem. Phys. Lett.* **102**, 174-178 (1983).
159. H. Yoshida, Y. Tokura, and T. Koda, "Charge-transfer excitation bands in electro-absorption spectra of metal (Co, Ni, Cu, Zn)-phthalocyanine films," *Chem. Phys.* **109**, 375-382 (1986).
160. S.J. Strickler and R.A. Berg, "Relationship between absorption intensity and fluorescence lifetime of molecules," *J. Chem. Phys.* **37**, 814-822 (1962).
161. P.S. Vincett, E.M. Voigt, and K.E. Rieckhoff, "Phosphorescence and fluorescence of phthalocyanines," *J. Chem. Phys.* **55**, 4131-4140 (1971).
162. M. Gouterman, R.A. Mathies, and B.E. Smith, "Porphyrins XIX. Triplet and quartet luminescence in Cu and VO complexes," *J. Chem. Phys.* **52**, 3795-3802 (1970).
163. M. Asano, Y. Kaizu, and H. Kobayashi, "The lowest excited states of copper porphyrins," *J. Chem. Phys.* **89**, 6567-6576 (1988).
164. T. Kobayashi, D. Huppert, K.D. Straub, and P.M. Rentzepis, "Picosecond kinetics of copper and silver protoporphyrins," *J. Chem. Phys.* **70**, 1720-1726 (1979).
165. Th. Förster, "Zwischenmolekulare Energiewanderung und Fluoreszenz," *Ann. Physik* **2**, 55-75 (1948); "Experimentelle und theoretische Untersuchung des zwischenmolekularen Übergangs von Elektronenanregungsenergie," *Z. Naturforsch.* **4a**, 321-327 (1949).
166. D.L. Dexter, "A theory of sensitized luminescence in solids," *J. Chem. Phys.* **21**, 836-850 (1953).
167. R.C. Powell and R.G. Kepler, "Evidence for long-range exciton-impurity interaction in tetracene-doped anthracene crystals," *Phys. Rev. Lett.* **22**, 636-639 (1969); *ibid.* **22**, 1232 (1969).

168. R.C. Powell and Z.G. Soos, "Singlet exciton energy transfer in organic solids," *J. Lumin.* **11**, 1-45 (1975).
169. A. Bergman, M. Levine, and J. Jortner, "Collision ionization of singlet excitons in molecular crystals," *Phys. Rev. Lett.* **18**, 593-596 (1967).
170. T. Kobayashi and S. Nagakura, "The biexcitonic quenching and exciton migration rate in aromatic crystals," *Mol. Phys.* **24**, 695-704 (1972).
171. G. Mourou, "Spectral hole burning in dye solutions," *IEEE J. Quantum Electron.* **QE-11**, 1-8 (1975).
172. T. Yajima and H. Souma, "Study of ultra-fast relaxation processes by resonant Rayleigh-type optical mixing. I. Theory," *Phys. Rev. A* **17**, 309-323 (1978); T. Yajima, H. Souma, and Y. Ishida, "Study of ultra-fast relaxation processes by resonant Rayleigh-type optical mixing. II. Experiment on dye solutions," *ibid.* **17**, 324-334 (1978).

